12-11-2009

Laser Induced Incandescence and Laser Induced Breakdown Spectroscopy based Sensor Development

Kemal Efe Eseller

LASER INDUCED INCANDESCENCE AND LASER INDUCED BREAKDOWN SPECTROSCOPY BASED SENSOR DEVELOPMENT

By

Kemal Efe Eseller

A Dissertation
Submitted to the Faculty of
Mississippi State University
in Partial Fulfillment of the Requirements
for the Degree of Doctor of Philosophy
in Engineering with an Emphasis in Applied Physics
in the Department of Physics and Astronomy

Mississippi State, Mississippi

December 2009

LASER INDUCED INCANDESCENCE AND LASER INDUCED BREAKDOWN

SPECTROSCOPY BASED SENSOR DEVELOPMENT

By

Kemal Efe Eseller

Approved:

Jagdish P. Singh Adjunct Professor of Physics and Research Professor of Institute for Clean Energy Technology (Director of Dissertation and Major Professor)	David L. Monts Professor and Graduate Coordinator of Physics (Co-Major Professor)
Fang Yu Yueh Research Scientist II of Institute for Clean Energy Technology (Committee Member)	Chun Fu Su Professor of Physics (Committee Member)
Thomas Philip Professor of Computer Science and Engineering (Committee Member)	Olin Perry Norton Research Professor of Institute for Clean Energy Technology (Committee Member)
Sarah A. Rajala Dean of College of Engineering Earnest W. and Mary Ann Deavenport, Jr. Chair	

Name: Kemal Efe Eseller

Date of Degree: December 10, 2009

Institution: Mississippi State University

Major Field: Engineering with emphasis in Applied Physics

Major Professor: Dr. Jagdish P. Singh

Title of Study: LASER INDUCED INCANDESCENCE AND LASER INDUCED BREAKDOWN SPECTROSCOPY BASED SENSOR DEVELOPMENT.

Pages in Study: 117

Candidate for Degree of Doctor of Philosophy

In this doctoral dissertation, two laser-based sensors were evaluated for different applications. Laser Induced Incandescence (LII) is a technique which can provide non-intrusive quantitative measurement of soot and it provides a unique diagnostic tool to characterize engine performance. Since LII is linearly proportional to the soot volume fraction, it can provide *in situ*, real time measurement of soot volume fraction with high temporal and spatial resolution. LII has the capability to characterize soot formation during combustion. The soot volume fraction from both flames and a soot generator was investigated with LII. The effects of experimental parameters, such as laser fluence, gate delay, gate width and various laser beam focusing, on LII signal was studied.

Laser Induced Breakdown Spectroscopy (LIBS), a diagnostic tool for *in situ* elemental analysis, has been evaluated for on-line, simultaneous, multi-species impurity monitoring in hydrogen. LIBS spectra with different impurity levels of nitrogen, argon, and oxygen were recorded and the intensity of the spectral lines of Ar, O, N, and H observed were used to form calibration plots for impurities in hydrogen measurements.

An ungated detection method for LIBS has been developed and applied to equivalence ratio measurements of CH_4/air and biofuel/air. LIBS has also been used to quantitatively analyze the composition of a slurry sample. The quenching effect of water in slurry samples causes low LIBS signal quality with poor sensitivity. Univariate and multivariate calibration was performed on LIBS spectra of dried slurry samples for elemental analysis of Mg, Si and Fe. Calibration results show that the dried slurry samples give good correlation between spectral intensity and elemental concentration.

DEDICATION

I would like to dedicate this dissertation to my mother; Nevhiz Eseller, my father; Göksenin Eseller, my sister; Esra Ece (Eseller) Bayat.

ACKNOWLEDGEMENTS

I would like to thank my advisor Dr. Jagdish P. Singh for his endless support during my graduate studies at Mississippi State University. I am very pleased to thank Dr. David L. Monts for guidance in this dissertation. I would also like to thank my committee members, Mrs. Fang-Yu Yueh, Dr. Chun Fu Su, Dr. Olin Perry Norton, and Dr. Thomas Philip. Finally I would like to thank ICET, Physics Department, NASA STTR (NNX08CD53P, 05-I T9.01), and U.S. Department of Energy (Cooperative Agreement no DE-FC26-98FT 40395) for providing financial support.

TABLE OF CONTENTS

Page

CHAPTER Page

CHAPTER Page

LIST OF TABLES

LIST OF FIGURES

FIGURE Page

FIGURE Page

CHAPTER I

INTRODUCTION

Laser spectroscopy is an essential tool for understanding and analyzing molecular and atomic compositions and energies. Technological developments in lasers, spectrometers and detectors have made incredible positive impacts on spectroscopy. Laser sources, such as pulsed lasers, dye lasers, and tunable lasers, have increased spectral resolution. A semi-classical approach to emission and absorption phenomena provides a way to understand laser spectroscopic techniques. Time-resolved, *in situ* laser spectroscopic techniques help to improve the detection sensitivity.

Objective of this dissertation is to develop laser-based sensors by using optical diagnostic techniques. My first goal was to develop a Laser Induced Breakdown Spectroscopy (LIBS) sensor to determine the concentration of impurities in hydrogen gas. The LIBS technique has several notable advantages over other analytical techniques, such as it prepares and excites the sample in single step and is applicable to samples in difficult environments. My second goal was to develop a LIBS sensor for the slurry measurements. Since a focused laser beam creates waves that disrupt the signal in liquid specimens, dried slurry samples were created for the first time and analyzed to overcome this limitation on LIBS.

Combustion diagnostics require techniques to investigate the efficiency and the structure of fuels and flames. My third goal was to apply LIBS to the diagnosis of biodiesel flames. The first LIBS measurements of the stochiometry of a flame and of the diagnosis of a biodiesel flame were achieved. Finally my last goal was to measure the soot volume fraction and to analyze the structure of soot particles using Laser Induced Incandescence (LII). LII is a technique that can provide measurements of the soot volume fraction produced by the vaporization process by applying a pulsed laser and recording the resulting incandescence emission. A compact, rugged LII system based on an Ocean Optics Inc. (OOI) spectrometer was developed for soot diagnostics.

1.1 Laser Spectroscopy

After the discovery of lasers, a remarkable improvement has occurred in spectroscopic techniques. Improvements in instrumentation aid analysis and have improved the spectroscopic techniques. Pulsed lasers have been used as new spectroscopic radiation sources. Measurement timing problems, environmental difficulties and spatial fluctuations in determining compositions have forced researchers to find more sensitive detection means. Enhanced detectors and spectroscopic techniques facilitate analysis even of weak signals. Laboratory conditions and techniques can generate new fields of applications for laser spectroscopy. There are several laser-based techniques for analysis of atomic and molecular species, such as Raman, Rayleigh scattering, laser-induced florescence (LIF), laser-induced incandescence (LII), cavity ringdown spectroscopy (CRDS), and coherent anti-Stokes Raman spectroscopy (CARS).

Atoms and molecules in high excited states can be generated by high intensity lasers. Absorption and emission of electromagnetic waves is a basic phenomenon in laser spectroscopy. A classical electromagnetic description of optics and spectroscopy helps to understand absorption and emission.

1.1.1 Emission and Absorption of Light

The absorption process in atoms and molecules is mainly dependent on the photons' energy. The probability of absorption is described by the Einstein absorption coefficient (A_{12}) and by the spectral energy density (ρ_v). Both induced absorption and emission processes can be explained as a transition from one energy state to another state. The excitation energy is released by a transition of photon energy $h\nu$ as induced and spontaneous emission. The induced emission process probability is equal to the induced absorption probability. Spontaneous emission can be emitted in any direction and it is related to the structure of the molecule. The number of photons emitted in spontaneous photon emission can be far more than from thermal radiation.

Discrete emission spectroscopy is an emission of a photon between two bound energy states. If the photon energy is equal to or greater than the ionization energy, continuous emission can result (Fig 1.1). Emitted photons can be in discrete or in continuum emission. Fluorescence emission is released only from a discrete upper level to the initial state which is bound. If the initial state is a repulsive state which can be separated, emission is discrete. When an atom reaches a higher energy level, fluorescence emission is released as the atom returns to a lower energy state. Energy transfer between two atoms can result in fluorescence emission.

Atoms absorb or emit energy in discrete amounts; however, molecules have three different processes. Those are electronic, vibrational and rotational transitions. Electronic transitions are typically in the visible or ultraviolet regions and vibrational and rotational transitions are in the infrared and microwave regions, respectively.

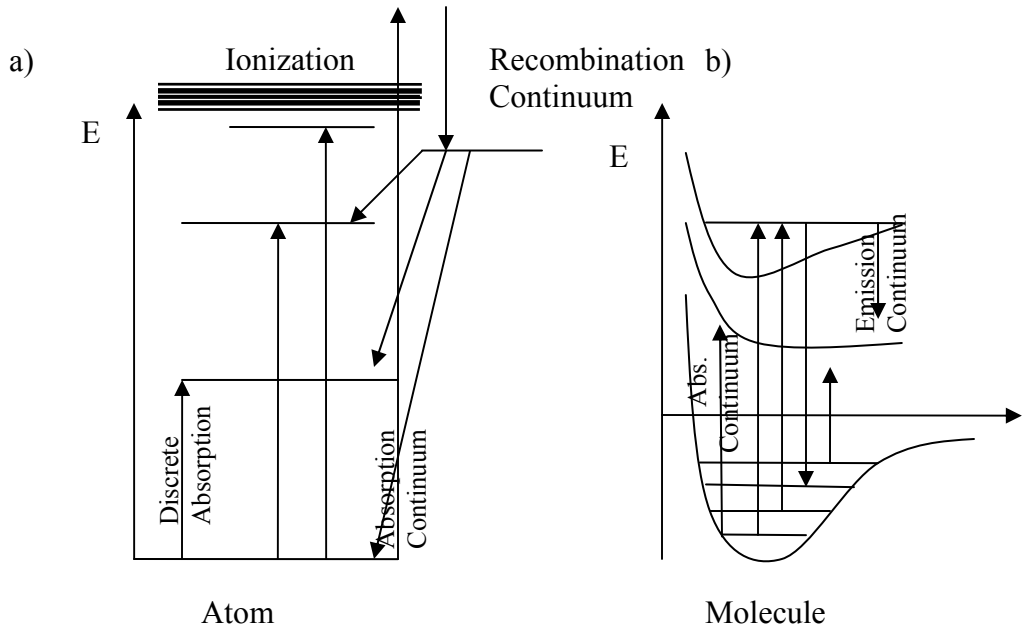

Figure 1.1

Discrete and continuous spectra distribution for a) atoms and b) molecules

Laser Induced Florescence (LIF) is an influential method for detecting molecules and atoms. Excited electronic ground levels of molecules (atoms) can be measured by absorption of laser radiation. Fluorescence or spontaneous emission is released after the absorption process. Collisions with species are also effective in transferring energy after the excitation of molecules by laser radiation. Background illumination and scattered laser radiation can be eliminated by use of a monochromator or a filter. Photomultiplier

tubes or other light sensitive detectors can be used to detect the fluorescence signal. Concentration or temperature measurements are the most common parameters investigated by LIF. Excited level transfers can occur as rotational or vibrational energies. Spontaneous emission occurs while excited molecules decay into their ground states. LIF is a sensitive measurement of absorption of laser illumination which helps to monitor molecular states. Detection systems with monochromators help to disperse and analyze the selected absorption transitions. Inelastic collision processes can give quantitative information and are collisionally occupied. [1]

The Raman effect is an inelastic light scattering where a photon is emitted at the same time when a photon is absorbed. Stokes Raman scattering is a photon emission process where the emitted photon energy is lower than the absorbed energy. The emitted photon energy is higher than the absorbed energy in anti-Stokes Raman scattering (Fig 1.2a). Two-photon absorption can be detected by Raman scattering, following absorption at visible or UV frequencies. Inelastically scattered photons which have Stokes (ω_s) and anti-Stokes (ω_{as}) frequencies are emitted from a virtual (v) eigenstate. Scattering from one photon-allowed transition can enhance the scattering. These transitions are called resonance scattering and are emitted from real state (Fig 1.2b).

Inelastic scattering has incoherent emission and is generated spontaneously. Coherent anti-Stokes Raman scattering is emission of a coherent signal beam which provides higher intensity signals. The Raman absorption process can involve the absorption of photon and emission of photons with frequencies ω_s and ω_{as} (Fig 1.2c). Coherent Raman scattering is stimulated light scattering. Signal intensities of coherent Raman scattering are greater than those of incoherent and spontaneous Raman scattering.

Coherent Raman scattering is more useful and can increase the spectral resolution. Raman spectroscopy helps to analyze molecules since they have Raman active vibrational mode(s). Both homonuclear and heteronuclear diatomic molecules are Raman active. Many vibrational transitions in polyatomic molecules are Raman active, even if they are not infrared active so this makes Raman more popular in molecular spectroscopy.

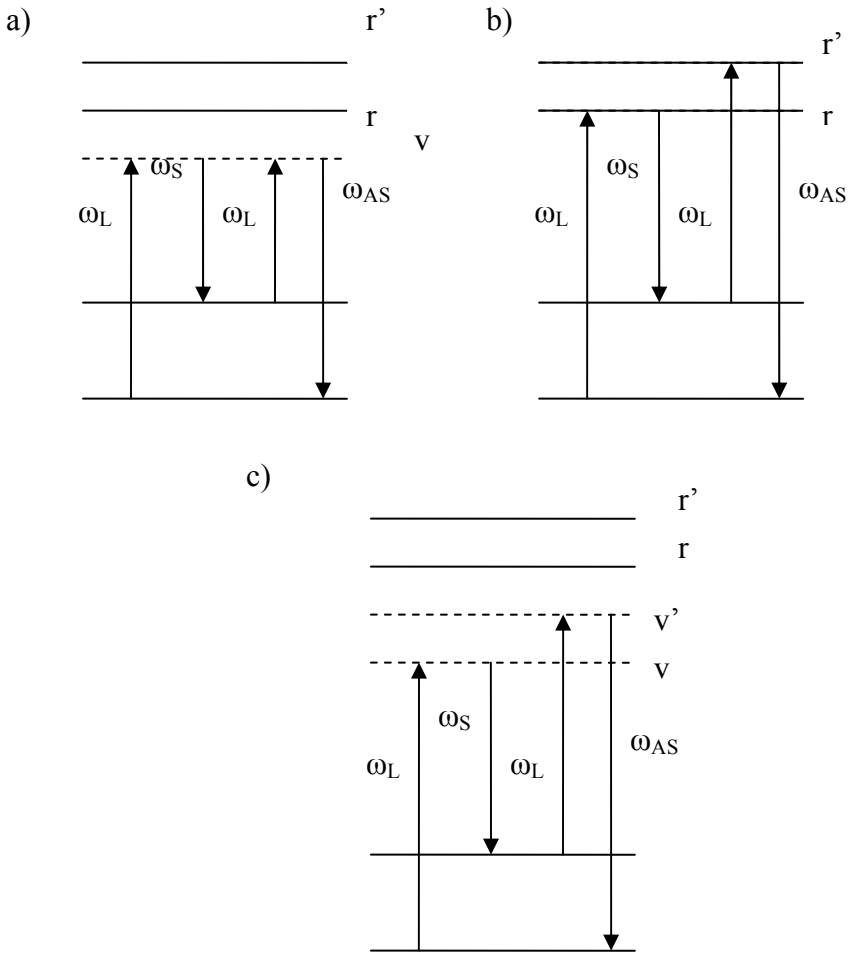

Figure 1.2

a) Spontaneous Stokes and anti-Stokes scattering b) Resonance Raman scattering
c) Coherent anti- Stokes scattering

Molecular rotational, vibrational, and electronic transitions can be identified in the visible and ultraviolet spectral regions. Raman scattering achieved revolutionary enhancement after discovery of lasers and became an important spectroscopic method. Adjustable laser frequencies made a big impact by avoiding inelastic scattering. Resonance Raman spectroscopy and coherent Raman spectroscopy are among the main developments from establishment of tunable laser sources. Electronic resonance helps to analyze reaction products and forensic samples, to characterize catalysts and chemical vapor depositions, to enable kinetic studies of proteins, and to facilitate concentration measurements in flames and in internal combustion and jet engines. [2]

Laser Induced Breakdown Spectroscopy (LIBS) is an atomic emission spectroscopic technique that was discovered after the development of laser technology in 1963. A laser plasma is generated and the emission line intensities are analyzed. *In situ* and remote detection capability makes LIBS an preferable technique. LIBS plasma formation has been investigated since the 1980's. Since that time, LIBS has become common for several analytical applications. In recent times, new technological developments of detectors, spectrographs and lasers have been used. Q-switched laser technology has the ability to focus high power energy to create a plasma. Analyzing new materials with this new analytical tool makes LIBS a useful method. Atomization of the sample, excitations of the atoms, detection of emission, and calibration of intensity as a function of concentration are the main objectives in atomic emission spectroscopy. A plasma from a high-power pulsed laser is focused and the resulting emission is sent to the detection system with a proper fiber optic cable. Signal precision and accuracy can be obtained by averaging or preprocessing the data. The signal can be enhanced by

increasing the signal-to-noise ratio (SNR) and eliminating interferences from continuum radiation.

LIBS was used initially for concentration measurements of solids, but nowadays it can be applied also to both gasses and liquids. Less energy is used to create atomization and the breakdown threshold is higher for gaseous samples. The LIBS signal can be detected under the surface of a liquid where the liquid is transparent at the laser wavelength. [3] Double-pulse lasers can create significantly enhanced signals in liquids due to creating a vapor hollow space during the first pulse. Breakdown creates multiphoton ionization at low pressure, and inverse Bremsstrahlung at high pressures from solids. The LIBS signal is produced by avalanche ionization. Recently LIBS was used to find the thickness of the coatings by applying several shots onto the surface of the coatings. [4]

Laser Induced Incandescence (LII) is a technique that detects enhanced thermal radiation from heated particles. LII has been applied mostly to soot particles. Lasers have been applied to extinction of the laser beam by soot particles. Where the LII signal starts to decay gives information about the size of the primary particles. The soot volume fraction (SVF) is related to the maximum of the signal where particles start to absorb laser energy. LII is widely used to investigate the processes in combustion engines, especially diesel engines. Quantitative spatially time-resolved measurements can be obtained with the LII technique. Since soot particles aggregate, measurements are mostly focused on the structure and formation of the primary particles. Laser heating of soot particles is followed by photodetection of the incandescence signal coming from the particles. Soot concentration, particle size and number concentration are the main parameters of interest in soot diagnosis by LII. One of the most important facts about LII

is that selection of the incident wavelength depends on the particle's absorption probability which is in the ultraviolet to the infrared regions. The experimental procedure depends on the laser excitation energy and wavelength, spectral detection region, and gate width and gate delay. The LII signal increases up to a laser fluence (J/cm^2) plateau region, which is typically from $0.2J/cm^2$ to $2.48J/cm^2$. [5] Beyond the laser fluence threshold, particles start to vaporize and the LII signal becomes approximately constant. The plateau region is identified by the vaporization threshold value. As the particles start cooling, the LII signal decays. High particle heating rates may affect the physical and optical properties of the particles. LII excitation also depends on the morphology of the soot structure(s). [6] Soot volume fraction (SVF) measurements aid in solving for the total volume of emitting particles in the field of view of the LII detection system. The SVF is related to the cross-sectional area of the imaged laser beam multiplied by beam thickness and divided by volume of emitting signal. [7]

1.2 Laser Spectroscopy Applications

Laser spectroscopy has become a very useful tool for chemical, physical, and biological applications. Concentration measurements, such as trace elements in chemical samples, are widely investigated. Concentrations of chemical reactants or products and collision-induced energy transfer processes can be determined by laser spectroscopy. The detection sensitivity is the main concern in analytical chemistry, especially for concentration measurements of impurity atoms and molecules. Femtosecond lasers can be applied to understand processes involving breaking or formation of chemical bonds. LIF can be used in chemical and biochemical research fields. Determination of molecular

structure and of reaction products, such as ground water contaminants, can generally be carried out by LIF. Hence LIF is often used to study the composition of molecules and the kinetics of chemical mechanisms.[2] DNA molecules bonding with dye molecules emit fluorescence radiation which gives information about the structure and rotational and vibrational motion of the molecules. Energy transfer between molecules facilitates analysis of structure with picosecond Nd:YAG lasers. [8] Moreover, structure and reaction mechanisms of membranes have been investigated with LIF. Hence LIF is an *in situ*, real-time monitoring technique which helps to analyze the molecular structure of specimens. Quantum state distributions of molecules formed by laser-excited collisional transfer can be monitored by florescence radiation. LIF helps to analyze combustion processes in flames, especially OH radicals, temperature, and radical and pollutant concentrations. In fusion applications, LIF has provided a considerable understanding of the impurities, like iron atoms. Optical access problems for imaging of the impurity measurements of plasmas are the main concern. However, hydrogen atom concentrations and velocity measurements in fusion devices and electron density measurements of plasma have been reported.

Raman spectroscopy is extensively used in combustion applications and it is well suited for specimen measurements. The spontaneous Raman technique with temperature determination is imperfect in some combustion applications, such as in flames. However coherent anti-Stokes Raman Spectroscopy (CARS) allows measurement of temperatures, even in sooty flames. Polymer films and fibers' structure, orientation, and bonding can be analyzed with Raman spectroscopy. Raman scattering has been used to detect molecular species on surfaces. Providing highly spatially resolved analysis, Raman microprobe

applications help to detect chemical species in or on the surface of samples. Forensic samples, pathological tissues, and characterization of catalysts are the main applications for the Raman microprobe method. [9-10] Adsorbed species in opaque pellets and powders can be analyzed *in situ* with Raman spectroscopy. Special configurations of optics can be used for detecting species for remote sensing applications.

Laser Induced Breakdown Spectroscopy (LIBS) is used in gas analysis with highly focused laser beams to create plasmas. Gaseous applications of LIBS are based on focusing a laser beam through a window and collecting the signal through an optical fiber. Low limits of detection (LODs) of toxic metals in gaseous environments can be obtained. However, application is not easy as the breakdown occurs at different locations along the laser beam axis. CN emission is the main concern that interferes with LIBS signal and is formed where breakdown occurs in air. LIBS can be used as an *in situ* and real-time continuous emission monitoring system for toxic metal measurements in air. However, high LOD values show that the development of new techniques is needed to decrease the detection limits.[11] LIBS has been applied to liquids and samples sunken or suspended in liquids. In this case, shock waves are the main concern that changes the LIBS signal shot-to-shot. Bubbles created inside the liquid also have a negative effect, which changes the reproducibility of the measurements. Experimental techniques have been applied to prevail over those problems. There are systems that work with bulk liquids and liquid jet samples. Remote online analysis is very useful with LIBS whereas other methods, such as inductively coupled plasma-atomic emission spectroscopy (ICP-AES) are not useful. Remote LIBS consists of a fiber optic probe that focuses the laser beam onto the fiber. The fiber output is focused onto the sample. Sending the laser beam

into the desired location is needed to analyze samples more precisely. Fiber optic LIBS (FO LIBS) can provide a high energy laser beam focused onto the desired sample without damaging the fiber. [12]Fiber Optic LIBS (FO LIBS) consists of two fibers; one delivers the laser pulse at the same time that the other collects emission from the plasma that is created. Atomic composition of powder materials, which are commonly used in pharmaceutical, ceramic, glass industries, can be identified by LIBS. Minimum sample preparation, quick analysis, and reproducibility are the main advantages of LIBS in powder specimen analysis. Microplasma formation on the sample creates shock waves that decreases the enhancement of the signal is the main disadvantage of LIBS. However, pellets which are prepared in a high-pressure hydraulic press with a binder give accurate and reproducible data. The focal spot on the pellet, delay time, and sample rotation speed have to be adjusted to improve of the LIBS signal. LIBS has been applied to environmental and hazardous samples. The elemental ratios in a gas flow or particles suspended in gaseous environment are among the main chemical/biological hazardous applications by LIBS. Bacterial samples, prepared as pellet substrates, can be analyzed, abolishing the matrix effects of LIBS. Elemental analysis in forensic science, such as biomaterials bone, hair, and nails, have been investigated by LIBS. Inhomogeneous structure and variation in the surface hardness of biological samples decreases the reproducibility. Hence focusing the plasma onto sample requires several adjustments to overcome discrepancies. However, high integration times and data acquisition techniques make available enhanced signal for analysis. *In situ* and *in vivo* sample analysis with LIBS is straightforward and easy. LIBS is one of the best techniques for analysis of particle composition and for determining the number density of the primary particles. [13]

Laser Induced Incandescence (LII), a newly established technique, is mostly applied to combustion studies. Soot particle measurements involve soot volume fraction, soot aggregate, and soot primary particle sizes. Polycyclic aromatic hydrocarbons (PAHs) are the main precursor in soot formation. *In situ* measurements of soot mass concentration in diesel engines can be analyzed by LII. Diesel engine exhaust measurements with LII have an important impact for determining the soot concentration with high temporal resolution. [14] Since there is no need for a specific laser line width and since LII can detect low polycyclic aromatic hydrocarbons (PAH) ppm concentrations, LII has the most significant capabilities for analysis of soot formation.

1.3 Dissertation Overview

My doctoral research is based on the fundamentals of laser diagnostics and sensor development. It will be presented in five chapters. Atomic structure and atomic emission spectroscopy is described in the second chapter. The third chapter focuses on the instrumentation for laser spectroscopic applications. Lasers and spectroscopic instruments are explained. The fourth and fifth chapters present the research that has been done to solve selected scientific problems. Chapter four is about sensor development for concentration measurements by Laser Induced Breakdown Spectroscopy (LIBS). In section 4.2, impurity measurements in hydrogen gas are explained. The LIBS sensor development was carried out for a specific need at the U.S. National Aeronautics and Space Administration's Stennis Space Center (NASA/SSC) test site. Section 4.3 is an application of LIBS to dried slurry measurements. The effect of water content in slurry specimens from the U.S. Department of Energy's Savannah River Site's Defense Waste

Processing Facility (DWPF) was investigated. Univariate and multivariate data analysis were applied to identify the calibration curves of the data. Chapter five is about the development of sensor technology for combustion diagnostics. Section 5.2 is about diagnosis of a biodiesel flame using LIBS. LIBS data of biodiesel and methane/air flames were obtained with an un-gated, miniature detector. In section 5.3, soot volume fraction measurements using Laser Induced Incandescence (LII) were performed. The soot structure and the performance of hydrocarbon rocket engines were studied and effects on the environment were evaluated. Finally, conclusions of each chapters are summarized in Chapter 6.

CHAPTER II

ATOMIC EMISSION SPECTROSCOPY

2.1 Introduction

In addition to translational and electronic states, atoms have spin, and nuclear spin rather than vibrational and rotational structure which only molecules have. Atoms have negatively charged electrons and a corresponding positively charge nucleus which are bounded each other in electrostatic forces. Atomic spectra are categorized by, wavelength, line intensities, and line series, depending on the line characteristics. For bound-bound transitions the electromagnetic radiation, that is emitted by the particles, is discontinuous, that is only isolated wavelengths are emitted. Atomic structure can be identified by the energy level. Balmer developed a relation which represents the wavelengths of hydrogen atomic spectral lines in the visible region. The quantum concept of atoms, which is based on the Bohr postulates, has proven the quantum mechanical behavior of atoms that terms have discrete energy levels. Emission and absorption occur when a electron moves from one energy state to an other. Spectral lines with fine and hyperfine structure demonstrated the theoretical structure of atomic spectroscopy. Line broadening results from translational broadening (Doppler broadening), from collisions (pressure broadening) and from the presence of electric (Stark broadening) and magnetic fields (Zeeman effect).

2.1.1 Atomic Structure

The structure of the atoms was first explained by electrostatic approach. According to that hypothesis, the attractions and repulsions between the nucleus and electrons form atoms due to electrostatic forces. However this description was incomplete for understanding of the phenomenon of the structure itself. The quantum mechanical approach gave rise to in understanding of the electron orbitals in more details. The Schrödinger equation provides atoms with a wavefunction Ψ which has n, ℓ and m quantum numbers. The principal quantum number "n" corresponds 1, 2, 3... with the electron orbital quantum number ℓ=0, 1, 2, 3, 4… corresponding to s, p, d, f, g, h... The Pauli exclusion principle states that electrons (and other forms) cannot be located in energy levels with the same set of quantum numbers n, ℓ, m_ℓ, m_s. "m_ℓ" and "m_s" where the last two are magnetic angular and magnetic spin quantum numbers. Each orbital can take an $2(2\ell+1)m_\ell$ quantum numbers. A minimum of two electrons can occupy ns orbitals and maximum of six electrons can occupy np orbitals. Electron spin angular quantum number "s" is related to the electron spin quantum number m_s that can be $\pm 1/2$. Total angular momentum J is the summation of orbital angular momentum "ℓ" and spin angular momentum "s", giving j = ℓ+s, ℓ+s-1,.., |ℓ-s|. The magnetic moment "μ_ℓ" is formed since electron flows in an "orbit" and it is in the opposite direction to the angular momentum "ℓ". The electron spin moment μ_s, due to spin of electron, is in the opposite direction of the spin angular momentum "s" (Figure 2.1).

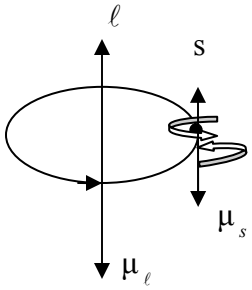

Figure 2.1

Vectoral representation of magnetic moments and angular quantum numbers

The coupling of two orbital angular momenta can be described in terms of ℓ - ℓ coupling. If valence electrons are located in different n and/or ℓ energy levels, they are said to be non-equivalent. The total angular momentum is given by "L" and further coupling of two orbital angular moments L= $\ell_1 + \ell_2$, $\ell_1 + \ell_2 - 1, \ldots |\ell_1 - \ell_2|$, where L = 0,1,2,3,.... Total orbital angular momentum quantization requires (2L +1) total magnetic quantum numbers M_L, where M_L =L, L -1,…, -L. Similarly spin spin "s-s" coupling between non equivalent electrons are given as S = $s_1 + s_2$, $s_1 + s_2 - 1, \ldots |s_1 - s_2|$. Also total orbital spin angular momentum s quantization has 2S +1 total magnetic quantum numbers M_S. Where M_S =S, S-1,…, -S. Russell Saunders (LS) coupling due to spin-orbit interaction gives the total angular momentum J. The resulting total angular momentum J = L + S, L+ S-1, …., |L – S|. As an example, consider two valence electrons in the s^1p^1 configuration where S = 1, L = 1 so it has ^1P and ^3P terms and "1" and "3" represent the (2s+1) electron spin multiplicity. Since J = 1 and 2 , there are two terms $^3P_1$, and $^3P_2$. Equivalent electrons, which are located in the same energy levels, cannot have same spin quantum numbers (m_s) and the same spin magnetic quantum numbers (m_ℓ). For

example when $(m_\ell)_1 = -1$, and $(m_\ell)_2 = -1$, spin quantum numbers are $(m_s)_1 = ½$, and $(m_s)_2 = - ½$ or $(m_s)_1 = - ½$ and $(m_s)_2 = - ½$

2.1.2 Spectral Line Transition

Transition probability and atomic population determine the intensity of a spectral line. The Einstein coefficients, degeneracy, and the number of particles occupied the energy states identify the characteristics of the transition process. The complexity of atomic forces leads to use approximations to decide which selection rules should be considered. Russell-Saunders coupling helps in this situation. The selection rules can be defined interms of their parities, and the quantum numbers L, J, and S.

Laporte rule, provides information of the parity of corresponding energy of that state. Changes of parity are in electric dipole transitions and opposite in electric quadruple transitions. Hence, parity selection rules are defined with electric dipole and quadruple transitions. When difference between total angular moments (ΔL) and (ΔJ) are "0", or ± 1, the transition is allowed, apart from both state gets difference of "0" value in electric dipole transitions. $\Delta J = 0, \pm 1$ except $J = 0$ and $J' = 0$, $\Delta L = \pm 1$.

2.1.3 Spectral Line Broadening

Degeneracy of electronic states, transition oscillator strength, and excitation conditions determines the spectral line intensities. The media, in which atom exist has an impact on the emission of radiation. Optically thin media prevent reabsorption of radiation in spontaneous emission. Electrons are distributed according to Maxwell's law. Emission from the excited state to the ground state which are called resonance lines can

be affected by self absorption process at high concentrations. Line peaks are broadened and amplitude is decreased.

2.1.3.1 Natural Line Broadening

Electrons in excited state decays until the equilibrium condition is obtained. The rate change is shown in the below equation:

$$\frac{dN_n}{dt} = A_{nm} N_n \tag{2.1}$$

N_n is the population in excited state n, an A_{nm} is the Einstein emission coefficient. . Lifetime "τ" of the state n can be defined by the time of number of electrons dropping to 1/e of its initial value. Heisenberg uncertainty relation concludes released energy and time τ can be measured at the same time and product of those relations must be bigger and equal to the Planck constant. Electric dipole moment μ has x,y, and z components and is represented as:

$$\mu_{x,y,z} = \sum_i q_i (x_i)_{x,y,z} \tag{2.2}$$

Selection rules determine transition probability $|R^{nm}|^2$:

$$R^{n,m}_{x,y,z} = \int \varphi^*_n \mu_{x,y,z} \varphi_m dx, dy, dz \tag{2.3}$$

$$| R^{n,m} |^2 = (R^{n,m}_x)^2 + (R^{n,m}_y)^2 + (R^{n,m}_z)^2 \tag{2.4}$$

Where n is excited, and m is the ground state, φ_n and φ_m are the excited and ground state wave functions. Einstein emission coefficient can be defined as:

$$A_{n,m} = \frac{64\pi^4 \nu^3}{(4\pi\varepsilon_0)3hc^3} | R^{n,m} |^2 \tag{2.5}$$

Natural line broadening can be determined by placing Heisenberg uncertainty relation in to equation 2.5

$$\Delta\nu \geq \frac{32\pi^3\nu^3}{(4\pi\varepsilon_0)3hc^3} \mid R^{n,m} \mid^2 \tag{2.6}$$

This type of broadening is in Lorentzian shape.[15]

2.1.3.2 Doppler Broadening

When radiation emitted from moving atoms in media is detected relative to the detector, broadening occurs. Characteristic broadening is defined as:

$$\Delta\nu = \frac{\nu}{c}\left(\frac{2kT\ln 2}{m}\right)^{1/2} \tag{2.7}$$

Where m is the mass of atom and "c" is the speed of light. Broadening ($\Delta\nu$) is much greater than natural line width and line is in Gaussian shape. It helps to identify the electron temperature of the atoms and ions by measuring width of the lines.

2.1.3.3 Pressure Broadening

Pressure broadening appears mostly in gaseous phase and there is direct collision process which results energy of atoms to be broadened. Broadening relation shows the dependency with mean collision time "τ"(Equation 2.8). It can be shown by Heisenberg uncertainty principle where energy and time can not be identified at the same time.

$$\Delta\nu = (2\pi\tau)^{-1} \tag{2.8}$$

Pressure broadening is in Lorentzian shape like natural line width.

2.1.4.4 Stark Broadening

Stark broadening especially happens in plasma conditions. Movement of electrons and ions create electric field in plasma condition. Electric field attraction between species is called Stark effect. Electric field acting on an atom creates Coulomb force (F). There is spectral line shift as a result which splits the energy levels. It can be defined as effect of energy levels with cause of force results in shifting and splitting. $\Delta\nu$ shifting is proportional with F^2 in most of the atoms. However it is proportional with F in Hydrogen which means there is indirect proportion with r^2. Higher shift is in quadratic Stark effects that make broadening asymmetric. Experiments identifying spectral line broadening can be seen on several sources [16-17]

2.2 Laser Induced Breakdown Spectroscopy

2.2.1 Introduction

When a high power laser is focused on to a target material, a plasma can be achieved due to several processes. Emission of radiation from the plasma, is the main parameter depending on the target conditions and the intensity of the laser. Liquid, gas and solid materials have different radiation emission characteristics. The structure of the plasma is highly complex to analyze. Several studies have been done on this issue. [18-19] We have focused mostly on the emission from plasmas which gives information of the species that are involved.

Intensity of the emission can be analyzed to understand the characteristics of the individual elements that are present. Spectra recorded for different samples show the

proportions to their elemental concentrations. Calibration curves drawn for known samples help to analyze unknown concentrations under similar laboratory conditions. Fluctuations in emission are the basic discrepancies while taking data. It can be avoided by choosing a standard line which is common in both unknown and known samples. Hence fluctuations do not affect the relative intensities.

The plasma depends on the size of the focal spot, the media pressure and composition, the wavelength and intensity of the laser and, the target vapor compostion. When a plasma condition is achieved, a hot plasma on the edge of the target is created due to the expansion waves in what is called the absorption zone. Plasma plume reduces through several modes from hot high density to cold low density (Figure 2.2). The plasma pushes the surrounding media and forms a shock wave. Laser absorption results in bremsstrahlung which is continuum radiation from free-free electron transitions. Due to the interaction between positive charge ions and electrons plasma is closest to the sample.

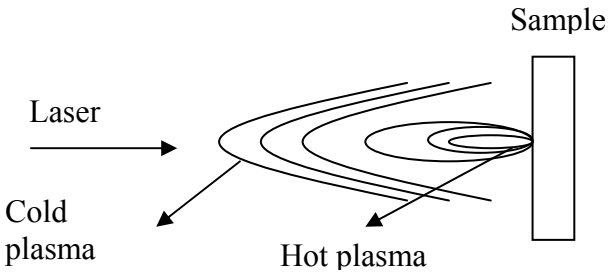

Figure 2.2

Schematic of plasma formation by laser beam

The first emission from the plasma is blackbody continuum radiation. It decays faster than the line emission. When it starts to cool down, the characteristic emission of

spectral lines can be detected. The ionized atoms are mostly located near the surface, while the neutral atoms are mostly a way from the plasma. Singly ionized and neutral atoms are observed near 500ns after plasma initiation.

2.2.2 Electron Density

Natural line broadening, Doppler, pressure and Stark broadenings are observed in plasmas. Natural line broadening which has Lorentzian shape is observed in the excitation of atoms. Doppler broadening has a Gaussian line shape and mostly occurs under low density plasma conditions. However in the early stages of plasma formation Stark broadening is the leading condition due to high electron density. When the plasma cools down, Doppler broadening can be seen in spectrometer's specifications, such as slit width, can be a good approximation to determine the observed line widths. Since the instrument's line shape is Lorentzian, spectral line width with Stark broadening effect can be determined.

$$\Delta\lambda_{total} = \Delta\lambda_{line} + \Delta\lambda_{spectrometer} \tag{2.9}$$

Plasma temperatures can be determined from the ratios of neutral atomic spectral lines which are combined using the Boltzmann equation.[20]

$$\frac{I_1}{I_2} = \frac{g_1 A_1}{g_2 A_2}\frac{\lambda_2}{\lambda_1}\exp(-\frac{|E_1 - E_2|}{kT_e}) \tag{2.10}$$

where g is the statistical weight, A is the Einstein coefficient, "T_e" is the plasma temperature, λ is the emission wavelength, k is the Boltzmann constant, $|E_1\text{-}E_2|$ is the energy difference between upper level of the transition 1 and upper level of the transition

2. As the difference between the two line intensities increases, the plasma temperature becomes more accurate.

There is a direct relationship between the electron density and the broadening effect. Hydrogen-like atoms show mostly Stark broadening. That is why hydrogen-like atoms give better results in electron density calculations. The relation between electron density and the full-width at half-maximum (FWHM) of hydrogen line is given:

$$N_e = C(N_e, T_e)\Delta\lambda_{FWHM}^{3/2} \tag{2.11}$$

Where the "C" coefficient for the hydrogen Balmer series can be found from the literature. [21]

2.2.3 Detection Limit

Limit of detection (LOD) can be determined by calibration curve in LIBS. It is defined as:

$$LOD = 3\frac{S_B}{S} \tag{2.12}$$

where S_B is the standard deviation of background, and S is the slope of calibration. LOD values of most of the elements were calculated in different matrixes.

2.3 Laser Induced Incandescence

2.3.1 Introduction

Laser-Induced Incandescence (LII) is an analytical tool, and is mainly used to analyze the particle structure and volume fraction. Heating of the particles with a high-energy laser light results in incandescence. The soot volume fraction (SVF) prediction with LII presents an analytical approach for temporally and spatially resolved measurements. Soot aggregates which are primary soot particles stick together and absorb the laser light in the Rayleigh scattering regime due to their particle sizes and diameters. The Rayleigh scattering regime is defined by relationship between the circumferences of the particles and the laser wavelength is in the range of 0.3 nm. [22]

LII mostly has been applied to soot particles, but we focus on the experimental approach to LII rather than the theoretical one.

2.3.2 Experimental Basis

The laser fluence heats the particles causing them to begin to vaporize. When they vaporize, the soot temperature becomes several thousand K. After that point, the particles' absorbance stays constant and that region refered to the plateau region. Radiation from the particles decreases as they start to cool down due to the laser pulse duration. The spectral region for collecting data can be a very wide range which is blackbody in origin. However selecting the region needs to take into factors such as background, laser induced inferences, and C_2 emission interferences.

The detection gate width and delay are the main parameters that should be determined in order to avoid interferences from fluorescence coming from the soot particles.[23] Short wavelength gas filters and proper gate delay and gate width help analysis the LII signal by avoiding interferences from laser induced fluorescence.

2.3.2.1 Soot Volume Fraction Measurements

Since LII emission from soot particles is in the same size, the Rayleigh limit of soot emission is used to measure the total volume of emitting particles within the field-of-view of the LII detection. The particle surface temperature should be measured prior to SVF calculation for the Rayleigh limit condition. The index of refraction is the one of the parameters that can be calculated from two-wavelength pyrometry. The emitting volume (V) of the cross-sectional area of the imaged laser beam (or sheet thickness) gives information about the soot volume fraction. The soot emissivity is dependent on the laser excitation that determines the volume fraction. Spectral variations in soot emissivity have an influence on the soot particle temperatures that effects the volume fraction measurements.

CHAPTER III

EXPERIMENTAL

3.1 Introduction

Laser spectroscopy enables the study of the interaction laser radiation and matter (i.e., atoms, molecules, atomic or molecular ions, or solids) as a function of wavelength. The major instruments needed to perform a spectroscopic study are an excitation source, a spectrometer, and a detector. The most common excitation sources for emission spectroscopy are lasers, sparks, arcs or flames. In laser spectroscopy, laser light is used as the excitation source. Spectral signals can be detected and analyzed with a spectrometer equipped with a proper detector. A variety of spectrometers, such as Czerny - Turner, Paschen - Runge, or Echelle, can be used for spectroscopic measurement. To obtain a good signal – to - noise ratio (S/N), detectors attached to spectrometers should have high quantum efficiency and with dynamic range. The selection of instruments for spectroscopic measurement depends on the required wavelength coverage, spectral resolution, and detection limit. In this chapter, the major instruments that are used in laser spectroscopic study are reviewed.

3.2 Lasers

Laser is an abbreviation of “light amplification by the stimulated emission of radiation.” They can be operated in the microwave, infrared, visible and ultraviolet

regions. Directionality, monochromaticity, brightness, and coherence are properties of laser light that makes it preferable in spectroscopic applications. The beam divergence of laser light is typically a few miliradians. The laser cavity limits wavelengths within the medium where it is resonant. Brightness can be defined as the emitted power per unit area. Coherency is a temporal and spatial property related to how well the monochromatic laser behaviors are preserved at very long times and distances that can sustain. Laser light is emitted by stimulated emission. In the spontaneous process, atoms or molecules emit unprompted radiation from upper energy level "m" to lower energy level "n":

$$M_m \rightarrow M_n + h\nu \tag{3.1}$$

The induced emission process requires photon emission due to a change of population N_n due to absorption from lower energy state. Two photons are creating process after one photon enters a medium can be described in special case as:

$$M_n + h\nu \rightarrow M_m + 2h\nu \tag{3.2}$$

$$\frac{dN_n}{dt} = N_m B_{mn} \rho \tag{3.3}$$

Where B_{mn} is Einstein coefficient and ρ is spectral radiation energy. At equilibrium where degrees of degeneracies of the two different energy states are equal, spontaneous emission is dominant with respect to induced emission.

$$\frac{N_n}{N_m} = \frac{g_n}{g_m} \exp\left(-\frac{\Delta E}{kT}\right) = \exp\left(-\frac{\Delta E}{kT}\right) \tag{3.4}$$

the stimulated emission process requires population inversion which changes the normal Boltzmann distribution. Normal Boltzmann distribution where population $N_n > N_m$ has to

be changed to $N_n<N_m$ with an energy input. This process is called pumping. The active medium that helps the inversion process and amplification of the absorbed radiation can be in gaseous, solid or liquid media. The lightening the laser cavity is confined between highly reflecting two mirrors. Those mirrors separation corresponds to an odd integer multiple of half wavelength' of laser light. Photons generated between those mirrors by spontaneous induced emission produce standing waves at certain resonance frequencies. A population inversion can be obtained by using three - or - four level system. This can provide stimulated emission in high accuracy. Inversion is provided by different pumping methods which create continuous wave or pulsed lasing. There are two pumping methods: optical and electrical. An energy supply with high intensity light source is used for optical pumping. Most of the pulsed lasers and some CW lasers use optical pumping. Gas and semiconductor lasers use electrical pumping.

The resonant frequency in the cavity depends on the linewidth of the transition between energy levels. It can be defined as

$$\nu = \frac{nc}{2d} \tag{3.5}$$

Where "d" is the distance between the two mirrors, and "c" is speed of light. Cavity nodes are transverse and longitudinal oscillations. The numbers of nodes depends on the amount of the radiation leakage from the cavity. Transverse cavity modes which are normal to the direction of propagation have a Gaussian intensity distribution. Longitudinal mode line widths are less than the Doppler line widths (Figure 3.1). Doppler line width can be explained by Doppler broadening effect which depends on the molecule's or atom's velocity.

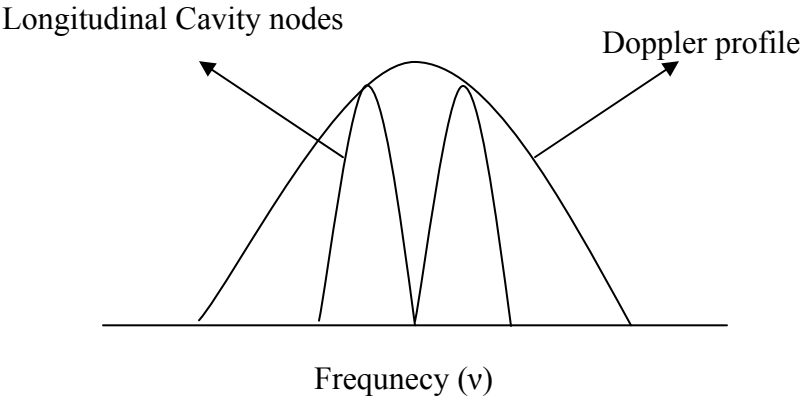

Figure 3.1

Two longitudinal modes within a Doppler limited laser line

Multimode lasers are generally used in spectroscopic applications, but single mode lasers give better results especially for high resolution purposes. Infrared lasers which are mostly used for high resolution purposes have a single cavity mode.

Q-switching is a very important phenomenon in laser technology because it helps to adjust the laser pulse power. It temporally controls the is the quality factor of the laser cavity by keeping the radiation between the cavity mirrors until the energy is built up and then energy in the laser cavity is quickly pumped. The quality factor (Q) of a laser cavity depends on the frequency divided by the laser line width. Single mode lasers have smaller line width which results in higher Q. It can be defined as:

$$Q = \frac{2\pi \nu E_c t}{E_t} \tag{3.6}$$

where E_c is the cavity-stored energy and E_t is the leak energy. Q-switching creates a high-power pulses due to short pulse duration. Moreover it creates pulse duration in the

nanoseconds range. Pulses can be obtained in picosecond, femtosecond range with the mode-locking technique. It can be applied to the multimode longitudinal cavity modes. The cavity mode-locking process requires modulation of the radiation in the cavity. After that the amplitude and phase of the modes of cavity are locked.

Frequency change or harmonic generation requires an electric field in which induced electric dipole and polarizability is

$$\mu = \alpha E + \frac{1}{2}\beta E^2 + \frac{1}{6}\gamma E^3 + ... \tag{3.7}$$

Where, in the power series, any terms higher than third order are non linear, Radiation is frequency doubled by the second term and frequency tripled by the third term.

There are several lasers that have been used widely. Those include ruby, alexandrite, titanium-sapphire, Nd:YAG, diode (or semiconductor), helium-neon, argon-ion krypton, nitrogen, excimer, and dye lasers. The details of these lasers can be found in many review articles. [24-26].

The neodyium (Nd) Yttrium aluminum garnet (YAG) Laser was used in my study. Nd:YAG lasers have been significantly important since they have first demonstrated. They are good pump sources. There are two kinds of Nd YAG lasers; one is continuous wave (CW) and the other is pulsed. Pulsed Nd:YAG lasers can be frequency doubled, tripled, and quadrupled, giving 532, 355, and 266nm. Actually they have pulse durations of about 10 to 20 ns with an average high power of several watts. [2]

Yttrium aluminum garnet ($Y_3Al_5O_{12}$) can be formed with neodymium ions (Nd^3) implanted into this special matrice which is referred to as YAG. Ground state of Nd^{+3}

with valence electron configuration $4d^{10}4f^3$ $5s^2 5p^6$ has ^4I and ^4F electronic states. Transitions occur from those states. Since orbital angular momentum L=6 and electron spin angular momentum S=3/2, the total angular momentum becomes J= 15/2, 13/2, 11/2, 9/2 with Russel-Saunders coupling. The laser transition is from $^4F_{3/2}$ to $^4I_{11/2}$. According to the selection rules $\Delta J = 0,\pm 1$ and $\Delta L = 0,\pm 1$ transitions are forbidden. However for YAG crystal field splits the $^4I_{11/2}$ energy state in to six energy state and the $^4F_{3/2}$ into two states. Two transitions are shown in Figure 3.2. These are the 1.0612 and 1.0648 in terms.

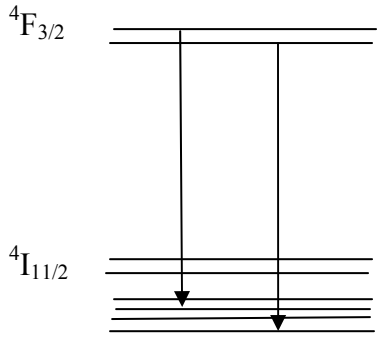

Figure 3.2

Transitions in Nd ^{3}energy levels with crystal field interaction.

3.3 Spectrometers

A spectrometer is an instrument that spatially separates the colors of light into a frequency (wavelength) spectrum. The spectrometers consist of a diffraction grating (or prism), an entrance slit, and collimating mirrors or lenses. Diffraction gratings in spectrometers separate incoming light by wavelength. Diffraction grating consists of many grooves typically (10^5) that reflect collimated parallel light. The angles and widths of grooves on glass plates depends upon the designed spectral resolution and wavelength

region of interest (Figure 3.3).. Light that is reflected from the grooves generates destructive or constructive interference. Grooves can be defined as light sources since they reflect incoming light with a width of d which is approximately equal to the average wavelength λ of the spectra. Difference between the paths of light reflected from two adjacent grooves produce constructive interference. The grating equation is as follows:

$$d \sin \alpha \pm d \sin \beta = m\lambda \tag{3.8}$$

Where α is the angle between normal and incident light, β is the angle between normal and reflected light.

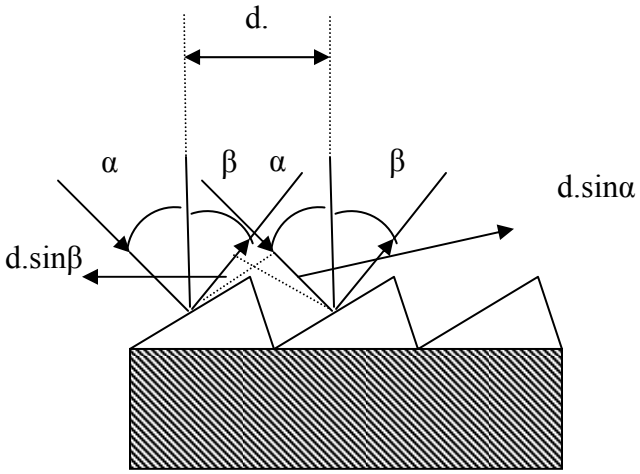

Figure 3.3

Reflection of incident light from a groove

Reflection from grooves needs to be adjusted depending on the type of spectrometer. The blaze angle between the groove normal and the incident light is determined according to the desired spectral range and spectrometer type. The angular dispersion can be defined as $(d\theta/d\lambda) = n/d\cos\theta$. The resolving power of grating is given

by R = nN, where N is the number of grooves. [15] Depending on the design, there are some different spectrometers,

Czerny-Turner spectrometers are widely used in spectrometric applications. The grating, entrance and exit optics are inside the spectrometer (Figure 3.4). Gratings typically have 100 to 4800 grooves. The spectral resolving power is the wavelength divided by the difference between two consecutive wavelengths. Diffraction limit line profiles are achieved if the central maximum coincides with the adjacent wave minimum. Although spectrometers have the same structure as monochromators, they can detect different spectral ranges and large region simultaneously and successively. The signal which is received by the detector depends on the area of the exit slit and the spectral intensity. Charge coupled device (CCD) arrays with Czerny-Turner spectrometers can detect with low integration times where as although photoelectric recording is more sensitive it requires longer detection times.

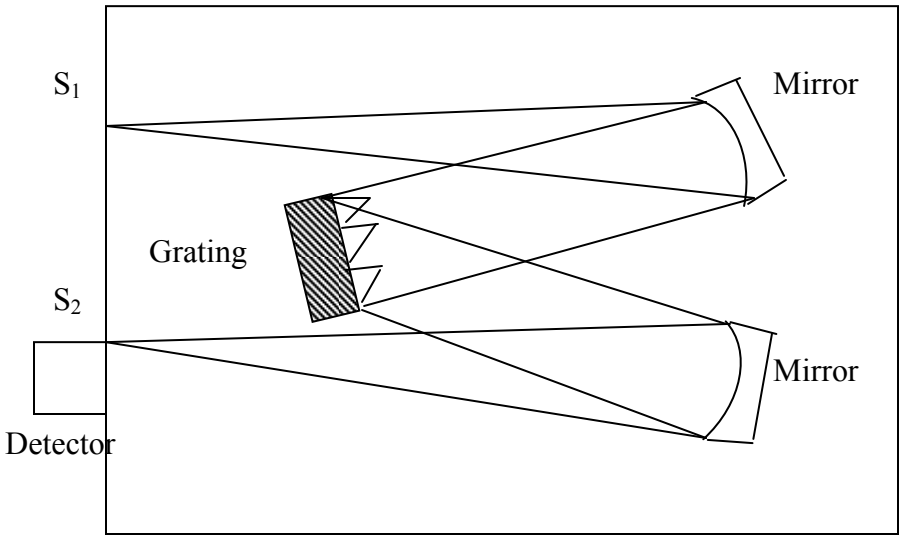

Figure 3.4

Schematic of a Czerny-Turner spectrometer

A Paschen-Runge spectrometer consists of several monochromators. A Rowland circle with grating and several slits attached is the main structure of this spectrometer. The grating is fixed and does not move (Figure 3.5). Spectral wavelength coverage (UV to NIR) needs too many photomultipliers to detect the signal. In the original Pashen-Runge spectrometers, photographic plates were used for detection, enabling recording the entire spectrum..

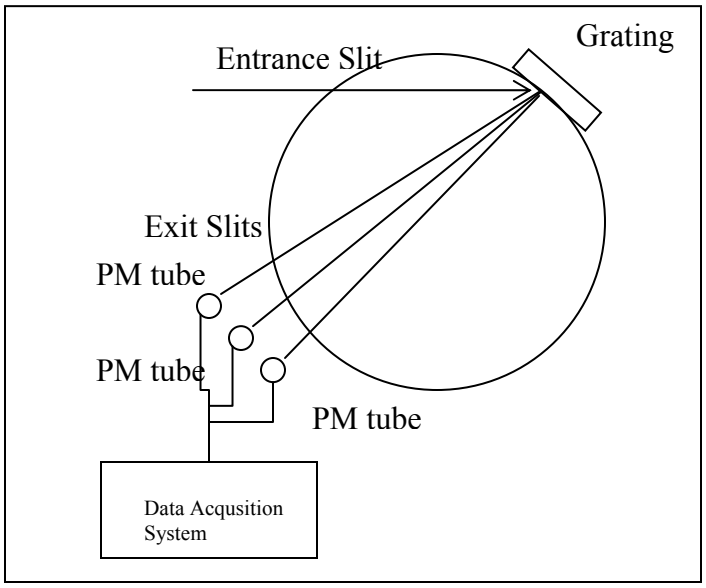

Figure 3.5

Schematic of a Paschen-Runge spectrometer

An echelle spectrometer consists of high dispersion echelle grating, mirror and lenses. For a echelle spectrometer, the grooves are very widely located to each other. As we have mentioned, the resolving power depends on the number of grooves and the spectral order. Although resolution is improved by increasing the blaze angle and the spectral order, the overlapping problem is unavoidable in a echelle spectrometer. The prism can be used as a second "grating unit" which is perpendicular to the other grating element. The prism determines the wavelength coverage before light is dispersed by the echelle grating. ICCD or CCD detectors can be attached to echelle spectrometer to analyze the intense and well resolved spectra. An ordinary echelle grating has 0.12 nm/mm average reciprocal linear dispersion and 0.003 nm resolution. One of the biggest differences between echelle and ordinary spectrometers is the grating density, which is

1200 for conventional grating whereas it is 79 for a echelle grating. Although an echelle grating covers a broader spectra and region, high limits-of-detection can be measured in some applications relative to Czerny-Turner spectrometers. However it doesn't mean that it has less detectability. There have been several applications with echelle spectrometers with ICCDs that give reasonable results that are comparable to the other detector systems. [27-28]

3.4 Detectors

The photo detector is a light sensor which is usually mounted on the spectrometer exit slit for recording spectra. Solid-state detectors, and photomultiplier tubes (PMT) are widely used detectors in spectroscopy. Time-resolved detection requires use of detection systems correlated with selectable time delays and signal integration times. Detectors with high quantum efficiency and fast temporal response are desirable combined with a spectrometer system.

Photomultiplier tubes (PMT) are sensitive light detectors, that create current relative to the intensity of the light that it absorbs. They consist of a photocathode and dynodes with a gain of 10^6-10^7 for incident photon. It has spectral bandwidth of 6 to 100 pm with a single channel (Figure 3.6). Noisy signal from PMTs is caused by dark current, fluctuating in the incoming signal, and fluctuations in the amplification process. The current that is created is relative to the voltage that has been applied to the detector and it is converted to the signal with an analog-to-digital converter. Noise coming from the detector's dark current is the main problem for gated detection purposes. It can be avoided by cooling the detector and a using boxcar averager-gated detection.

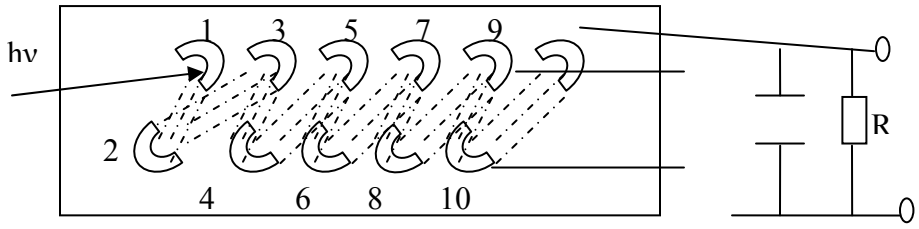

Figure 3.6

Photomultiplier tube with time-dependent output voltage.

Photodiode array (PDA), charge coupled device (CCD), charge transfer device (CTD), and coupled injection device (CID) devices are also solid-state detectors. These devices transfer photons to charge by pixels or semiconductor elements.[2] PDAs consist of several diodes integrated within a chip, forming a photodiode array. They have up to 2048 diodes in one dimension. Applying potential difference V to the p-n diodes and illuminated with light, the photocurrent generated discharges the diode capacitance (Figure 3.7.a). Metal oxide semiconductors (MOS) switch that is connected to the photodiodes recharges the photodiodes. High temperature has a major effect on the integration time, increasing the dark current and reducing the signal-to-noise ratio. For most of spectroscopic applications such as plasma diagnostics and induced incandescence, gated detection is essential to analyze very weak signals, especially in high background. CCD and PDA detectors coupled with Echelle spectrometers provide signal integration times in the nanosecond to microsecond range.

Quantum efficiency is the ratio of rate of photoelectrons divided by rate of incident photons. CCDs which have replaced PDAs have the ability to change charge

capacitance of MOS capacitors, providing 90% high quantum efficiency (Figure 3.7b). CCDs are mostly preferred because they have low dark current with respect to other detectors (PMTs, PDAs).[29] They can be used for in 350-900 nm spectral range. Being two dimensional and easily coupled with spectrometers intensified coupled device (ICCD) and CCDs are the most preferable detectors in spectroscopy.

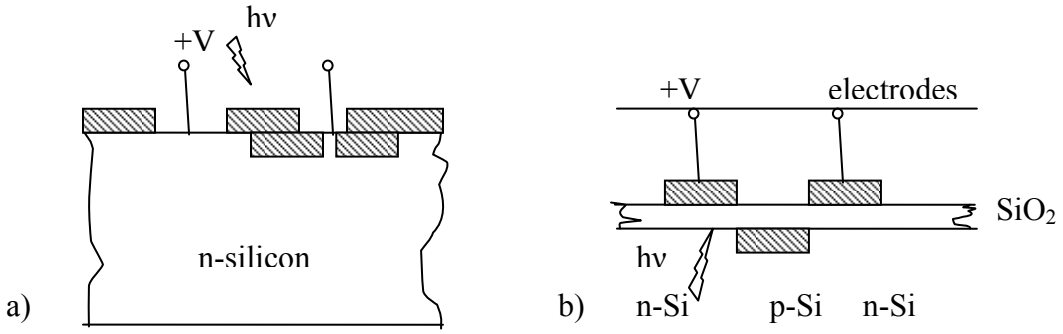

Figure 3.7

a) Schematic of single diode array and b) CCD array

CCDs catch electrons that are generated from electrons and holes by detecting incoming light. Analog-to-digital converters in CCDs help to transform the signal from where it is created by the electrons in to the final form. ICCDs have image intensifier that work as shutters opening and closing in nanosecond time scale. As has been mentioned for PMTs, the photocathode in ICCD changes photons that the absorbed into images by producing electrons by the photoelectric effect.[24] The photocathodes' quantum efficiency depends on the cathode material, thickness of the photo emissive material and the incident radiation wavelength. A microchannel plate (MCP) consists of a glass with a microchannel structure system (Figure 3.8). Electrons are transformed to photons and

amplified, and focused on the phosphor screen of the microchannel plate (MCP). The MCP gate voltage is generally in 200V which is sufficient to accelerate electrons up to high voltages. The photocathode has the most important role for detection because it creates electrons independent of the incident photons, and determines the quality of the ICCD. Gating capability depends on the voltage that is applied to the photocathode which determines the shutter switching for the shortest gate delay times. Gate delay times can be changed mostly from 1 to 3ns with using conductive nickel.[30, 24] For time resolved measurement such as LIBS and LII, the detector should have gating capability.

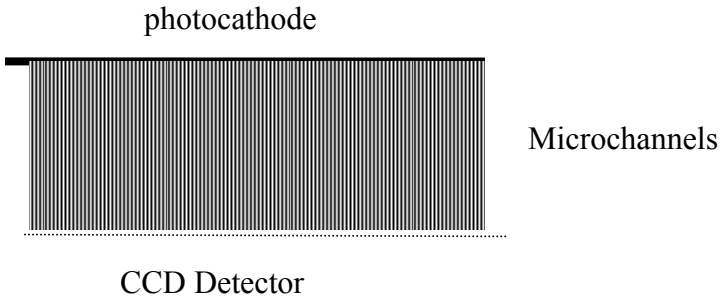

Figure 3.8

Schematic of the MCP detector

CHAPTER IV

LIBS SENSOR FOR CONCENTRATION MEASUREMENTS

4.1 Introduction

Laser-induced breakdown spectroscopy (LIBS) is a versatile elemental analysis technique for any form of material—solid, liquid, gas, or aerosol specimens. [31-33] Optical techniques based on either absorption or scattering have been used for sample composition measurements.[34-35] Molecular energy levels and transition probabilities can be determined with Raman Spectroscopy.[1] Laser Raman Spectroscopy (LRS) has been used to investigate the dynamics of vibrational relaxation in gases, liquids, and solids. It can detect homonuclear diatomic molecules, but has poor detection sensitivity due to weak Raman cross sections.[36] Also it has extremely low efficiency of inelastic light scattering which has cross sections of 10^{-12} of those of infrared absorption.[37] Coherent anti-Stokes Raman Spectroscopy (CARS) measurements provide more information on molecular structures which is useful and involve a higher intensity of scattered light from the molecules.[2] CARS spectra of O_2 in visible and UV photolysis of the ozone layer have been recorded. Since it needs monochromators (and photomultiplier tubes for detection optics), minor species detection is difficult to achieve.[38] Infrared (IR) spectroscopy can identify compounds or investigate sample composition. The disadvantages of IR spectroscopy are poor detection limits, non-IR active components, and the possibility of different species possessing similar IR spectra. Concentration measurements of free

radical species (e.g., OH, O, H), pollutant species (e.g., NO, CO, NO_2, SO_2), and metallic species (e.g., Na, K, NaS) have been performed with LIF in several applications.[2] Plasma experiments using Balmer-α and Lyman-α excitations in neutral hydrogen density and velocity measurements have been reported. Burakov *et al*. have performed the first hydrogen Balmer-α atom measurements in a tokamak plasma discharge.[39] Since metallic impurities effect plasma formation and radiation, LIF measurements of impurity concentrations have been made.[40] Laser excitation Balmer- α measurements for hydrogen have been made to analyze electron temperatures and densities.[41] Absorption and laser-induced fluorescence (LIF) methods need a tunable laser in the ultraviolet (UV) and vacuum ultraviolet (VUV) spectral regions. [42-43] Collisional quenching effects are the main concern in LIF measurements. [44] These techniques can generally require bulky and sophisticated lasers. Cavity Ringdown Spectroscopy (CRDS) is an optical technique that detects atomic and molecular species even at small concentrations. It has excellent sensitivity, but again needs tunable UV and VUV lasers.[45] Also, CRDS can't detect atomic species, such as argon, because the resonance transition is not accessible with commercial lasers. Infrared (IR) spectroscopy is not suitable for homonuclear diatomic molecules, such as N_2, O_2, or H_2, which are the main species of interest for combustion.[46] Laser Raman Scattering (LRS) is relatively simple and can detect several species simultaneously and so provides an alternative to the IR technique. In contrast to IR, visible or near-IR light is efficiently transported by fiber optics; in addition, Raman transitions are allowed for homonuclear diatomic molecules, such as N_2, O_2, or H_2, which are not observed by electric dipole-allowed IR vibrational transitions. LRS has also been successfully used to measure gas concentrations and gas temperatures in combustion

environments. However, the main disadvantage of LRS is the intrinsically low Raman cross section. Therefore, it usually requires a long integration time for accurate measurement, particularly for species present in low concentrations. None of these techniques are ideal for NASA/SSC rocket engine testing applications.

Laser Induced Breakdown Spectroscopy (LIBS), a laser-based diagnostic technique, has proven to be effective for measuring the concentrations of elements in various types of test media including gases, liquids, and solids. [4,13, 47-56] A laser-induced breakdown plasma consists of electrons and ions as well as neutral particles and it exhibits rich emission spectra. The optical emission from neutral and ionized atoms is collected to obtain the emission spectrum. Analysis of a LIBS spectrum identifies the elements present and provides information about elemental concentrations in the test medium. The LIBS technique has several notable advantages over other analytical techniques, such as it prepares and excites the sample in single step. It can be operated in harsh and difficult environmental conditions. LIBS can simultaneously detect all the elements of interest using a broadband spectrometer. LIBS applications cover from analysis of aerosol samples and toxic metals in a gas stream[57,49] detection of metals inside solids, concrete, and paint, quantitative analysis in various matrix, [58-60] and qualitative analysis of U and Pu particles. [61]

Feasibility of using LIBS has been studied for concentration measurements in two sample forms. First, LIBS was used to detect impurities in hydrogen gas. Details of this work are in Section 4.2. Second, LIBS was used to detect the elemental composition of slurry.

4.2 LIBS for Hydrogen Impurity Detection

The real-time continuous emission monitoring capability of LIBS in the off gas from combustion facilities has been demonstrated previously. [4, 49, 62-63] LIBS has also been evaluated for rocket engine health monitoring, [64] and combustion diagnostics. [65-67] It has the capability to provide good sensitivity, to accurately measure low levels of impurities in H_2 tanks and feed lines, and to provide non-intrusive, on-line, simultaneous multi-species impurity detection capability. This type of diagnostic technique is very valuable for verifying hydrogen quality for engine testing. In this work, LIBS has been evaluated to measure the trace level impurities of N_2, Ar, and O_2 in H_2 using an ungated detector. The effect of pressure on the measurement was examined and the detection limits for N_2, Ar, and O_2 impurities in H_2 are reported.

4.2.1 Experimental Details

The conceptual design of the LIBS system for hydrogen purity measurement is shown in Figure 4.1. A frequency-doubled, pulsed Nd:YAG laser (Big Sky, Model CFR 400) (532 nm, 200 mJ, 9-mm diameter) was used as the excitation source and can deliver laser energies up to 189 mJ per pulse. The laser beam was focused inside the sample cell by a 10-cm focal length fused silica convex lens to produce laser-induced sparks. The focusing lens was attached to the LIBS system to avoid alignment problems, and it was adjusted to optimize the signal-to-background ratio. The LIBS signal from the sample cell is collimated using the same laser focusing lens and focused into an ultraviolet (UV) transmission, bifurcated optical fiber. The collection optics collects light emitted by the laser discharge plasma and directs it into a fiber optic cable. The output end of the fiber

was connected to an ungated LIBS spectrometer (Ocean Optics Inc. (OOI), model HR 2000) that covers the spectral range from 620 to 820 nm. This detection system allows simultaneous detection of all species of interest. Simultaneous LIBS spectra of multiple species were recorded and analyzed using a personal computer.

4.2.1.1 Sample Cell:

A high-pressure sample cell was designed which can easily be filled with different gas mixtures. Since the presence of O_2 in H_2 in a LIBS spark could initiate combustion and become explosive, special precaution was taken in designing the cell and gas lines to avoid any air leaks in the sample cell and gas lines. Figure 4.2 shows the design of a stainless steel (SS) sample cell for hydrogen gas mixtures. A SS four-arm cross (Pressure Products Company) was used to fabricate the sample cell. Two quartz windows were mounted in two opposing arms of the cross.

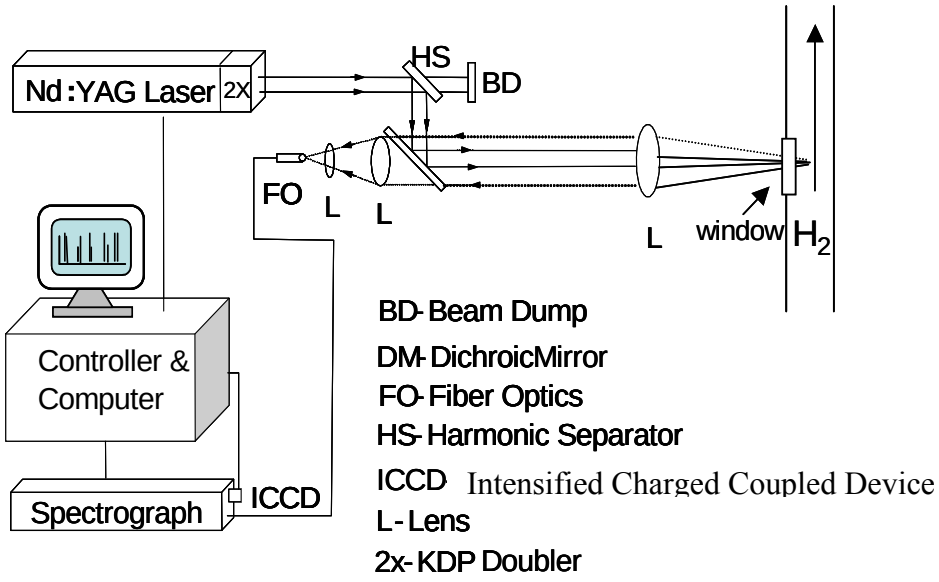

Figure 4.1.

Schematic of the LIBS system for a hydrogen impurity monitor.

Two SS plates with threaded holes were attached to the other two arms. A vacuum pump was connected to one threaded hole and the other threaded hole was connected to a gas manifold system, using compressed gas cylinders to introduce gas mixtures into the cell. One high-range (700 psi) and one low-range (10 psi) pressure gauge were attached to the sample cell. A quartz window provided optical access for laser light. A laser beam dump was attached to the other quartz window. A lecture bottle of a mixture of 97% hydrogen, 1.9% nitrogen, 0.1% oxygen and 1% argon and another bottle of pure hydrogen gas were used to prepare the sample with different levels of impurities.

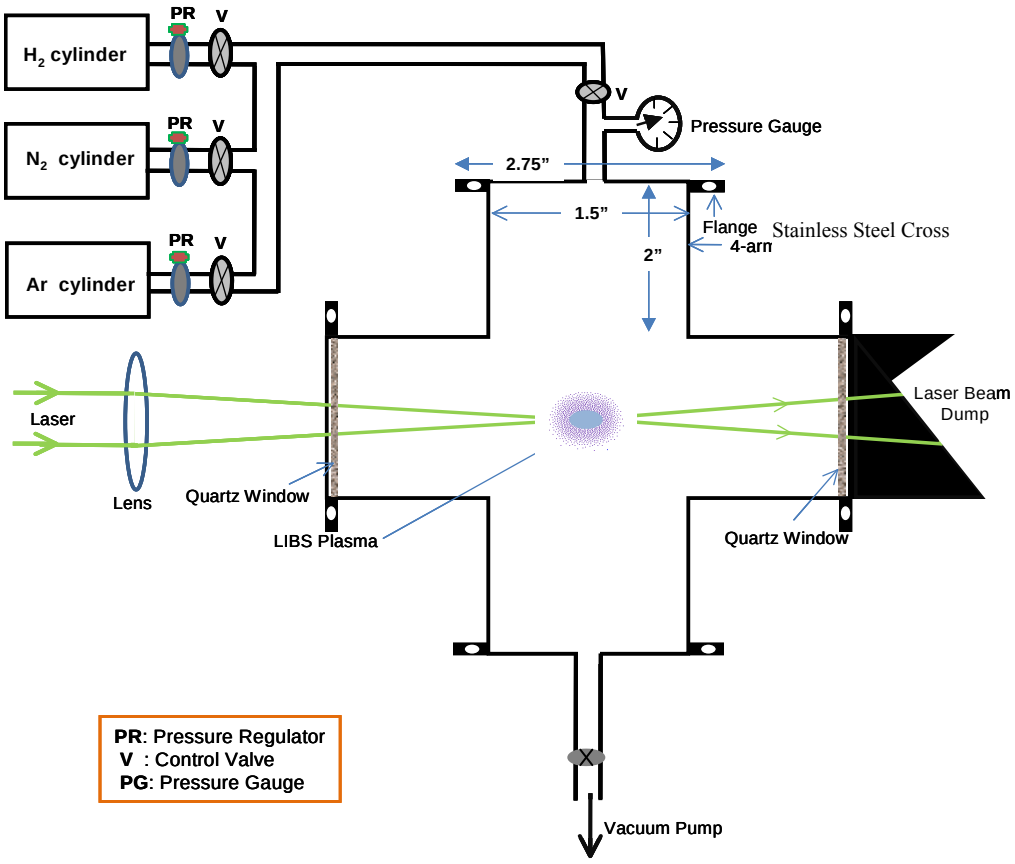

Figure 4.2.

Schematic of the stainless steel (SS) sample cell for hydrogen gas mixture.

LIBS spectra from mixtures of H_2 with low concentrations of N_2, O_2 and Ar were recorded using the miniature spectrometer. These spectra were used to find the most sensitive spectral lines for N_2, O_2 and Ar measurements in H_2. Since the LIBS signals from the impurities are much lower than from high-concentration H_2 (>96%), special efforts were made to enhance trace species signals with a proper detection system and optics. Also to simultaneously detect both high concentration H_2 and trace impurities, the dynamic range of the detection system was considered in preparing the various gas mixtures. The concentration range studied in this work is that typically expected in a

hydrogen tank or delivery line due to contamination. A 700-nm long pass filter (Thorlabs) was used in all the measurements to avoid detector saturation due to the strong hydrogen signal at 656 nm. Figure 4.3.a shows a typical LIBS spectrum of a H_2 mixture (O_2: 0.08 %, Ar: 1.00 %, N_2: 2.00 %) at 850 Torr. In LIBS, strong continuum background radiation dominates in the first 100 ns, and the continuum background radiation and atomic emission decay with time. But the continuum background radiation decays faster than the atomic emission. Therefore with a gated detection system, one can obtain a good signal-to-noise ratio data by selecting a proper detection window (i.e., gate delay and gate width). The miniature spectrometer used in this work can provide some gating capability (20-ms fixed gate width) if a laser system that allows external Q-switch triggering is used with this spectrometer. Our laser system cannot be operated with an external Q-switch. Therefore the current system is considered to be an ungated system. It is clear from Figure 4.3.a that the high continuum background is dominant in the collected spectra. For data processing, the continuum background was fitted with a polynomial function and was subtracted from the raw spectra. Figure 4.3.b. shows the background-subtracted LIBS spectrum of this hydrogen mixture. The atomic lines identified from the spectrum are marked in the figure and the spectroscopic constant of these lines are given in Table 4.1.[68]

4.2.1.2 Effect of Pressure

For practical applications, measurements might be conducted at various pressures. The effect of pressure on the detection of the impurities in hydrogen was studied. LIBS spectra of H_2 mixtures were recorded at different pressures and the results are shown in

Figure 4.4. It is clear from the figure that the background increases with gas pressure until 24.7 psi. When gas pressure is higher than 34 psi, the continuum radiation maintains the same level. The signals of N, O, and Ar lines at different pressures follow a similar trend as the background. To understand the characteristics of laser-produced plasmas at different pressures, two important parameters, plasma temperature and electronic density, need to be evaluated. Plasma temperature is generally obtained using a Boltzmann plot. However, the spectral lines obtained in the observed spectral region have very similar upper energy (see Table 4.1). Therefore, they are not suitable for temperature calculation. Plasma temperature can also be obtained by comparing the continuum radiation with calculated Planck radiation. Due to the ungated detection used in this work, the temperature obtained from LIBS spectra will be a time-averaged temperature. The fact that the shape of continuum background between 680 and 740 nm did not change with different pressures indicates that the averaged plasma temperature did not change significantly with gas pressure. By taking into account the spectral response of the 700-nm band pass filter, the continuum background peak near 700 nm was found which corresponds to a temperature around 4140 K, using Wien's displacement law ($\lambda_{max} = b /T$) (peak at 730 nm was found in all spectra of H_2 mixtures).

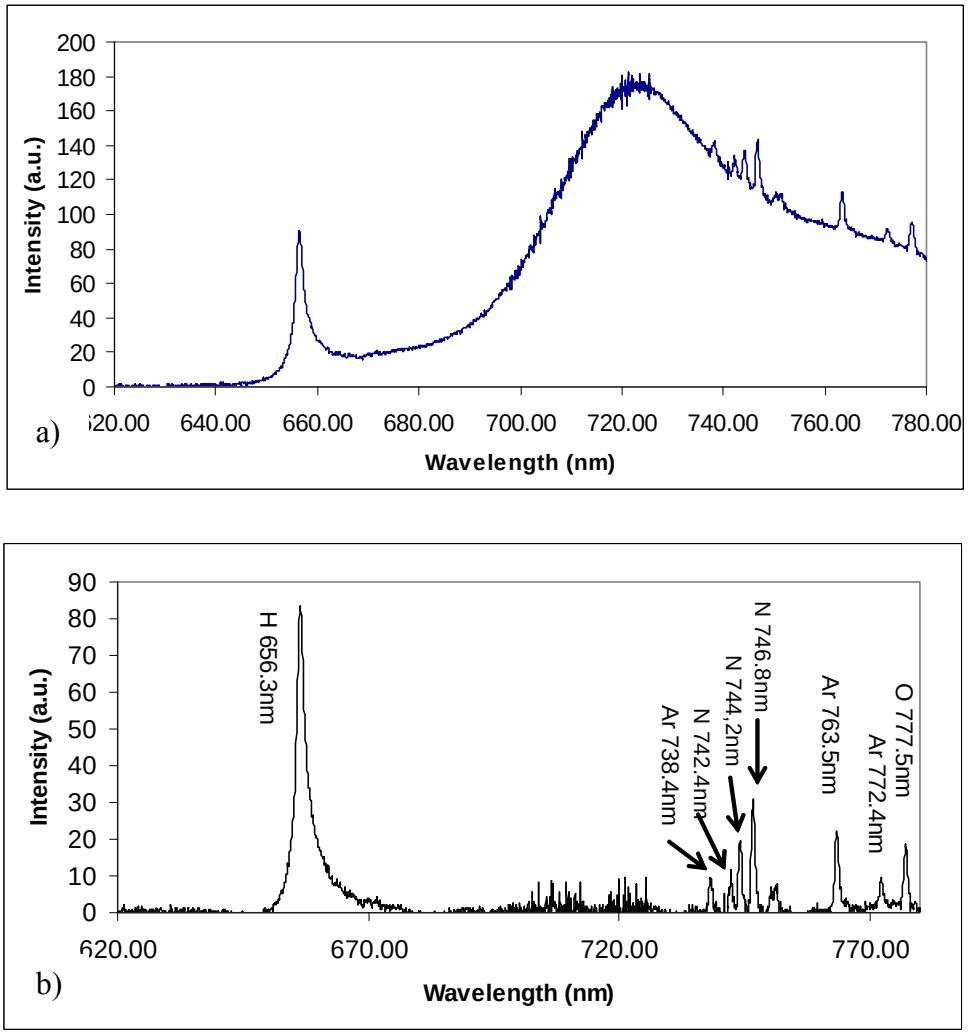

Figure 4.3.

LIBS spectrum of H_2 mixture (O_2: 0.08 %, Ar: 1.00 %, N_2: 2.00 %) at 850 torr. a) Raw data. b) Background-subtracted data.

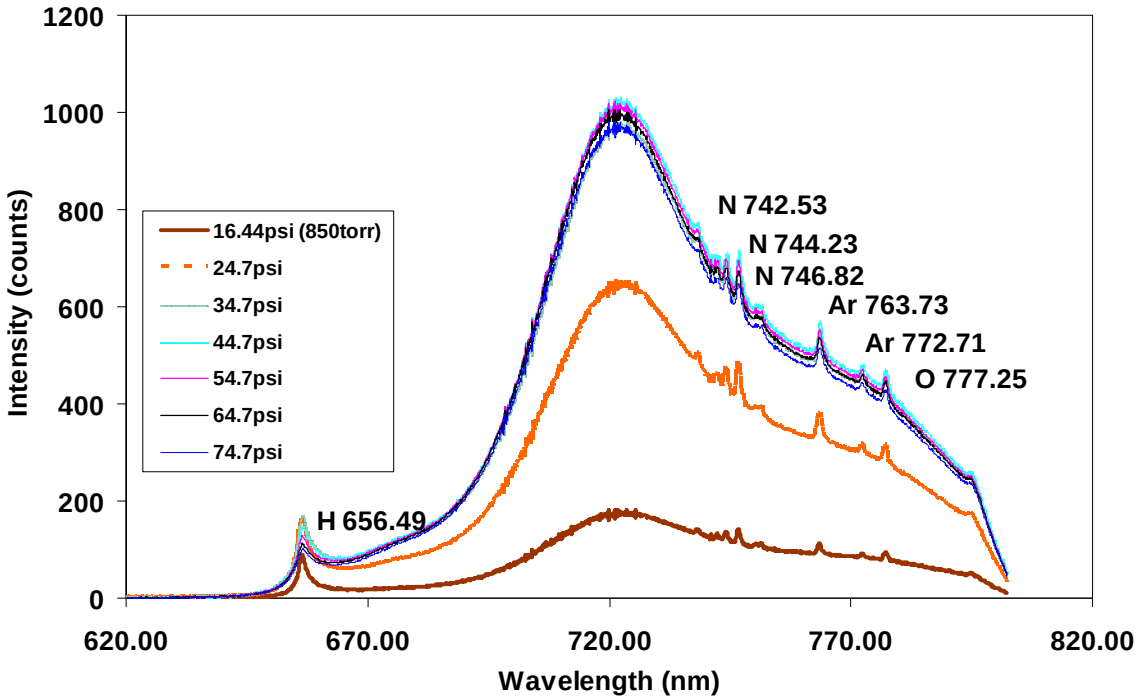

Figure 4.4.

LIBS spectra of H_2 mixture (O_2: 0.08 %, Ar: 1.00 %, N_2: 2.00 %) at different pressures. Each spectrum is an average of 200 laser pulses.

Table 4.1.

Spectroscopic constants and Einstein coefficient (A_{kj}) of the observed atomic lines.[54]

Atomic lines (nm)	A_{kj} ($\times 10^8$ s^{-1})	Upper Energy (cm^{-1})	g
H I 656.285	0.6465	97492.	6
N I 742.364	0.0595	96751	4
N I 744.229	0.124	96751	4
N I 746.831	0.193	96751	4
Ar I 738.398	0.0847	107290	5
Ar I 763.511	0.245	106238	5
Ar I 772.376	0.0518	106087	3
Ar I 772.421	0.117	107496	3
O I 777.194	0.369	86631	7
O I 777.417	0.369	86627	5
O I 777.539	0.369	86626	3

The plasma electron density (N_e) can be calculated from the Stark-broadened H_α emission lines which are based on comparison of measured line widths.[69]

$$N_e = C(N_e, T)\Delta\lambda_{FWHM}^{3/2} \tag{4.1}$$

where $C(N_e,T)$ is the coefficient that is only a weak function of the electron density and temperature, $\Delta\lambda$ is the Stark-broadened full-width-at-half-maximum (FWHM). The observed H_α line at different pressures can be well fit with a Lorentzian line profile. The Stark broadening line width $\Delta\lambda_{Stark}$ was obtained by subtracting $\Delta\lambda_{instrument}$, which is calculated from the spectral lines of a low-pressure Ar lamp, [70] from the experimentally measured line width $\Delta\lambda_{measured}$

$$\Delta\lambda_{Stark} = \Delta\lambda_{measured} - \Delta\lambda_{instrument} \tag{4.2}$$

The $C(N_e,T)$ coefficients at 10000K with corresponding electron densities were taken to calculate N_e. Figure 4.5 shows the calculated electron density at different pressures. Since the data was recorded with an ungated detector, the results shown in Figure 4.5 are a time-averaged electron density. This figure shows that the electron density first increases sharply with gas pressure. At gas pressures above 30 psi, the electron density increases slowly with pressure. This result is consistent with the observation of Tsuda and Yamada.[71] They measured the electron density of a high-pressure argon plasma produced using a XeCl excimer laser and found that the electron density increases with increasing pressure. However the electron density saturates and decreases when it is above a critical pressure. The critical pressure is laser frequency and laser energy dependent.

The signal-to-noise ratios for the atomic lines of N, O, and Ar at different pressures have been calculated (see Figure 4.6). It shows that the best signal-to-noise ratios (S/N) are obtained from measurements at pressures between 20 and 30 psi. Gas pressures higher than 30 psi did not give better sensitivity for impurity detection.

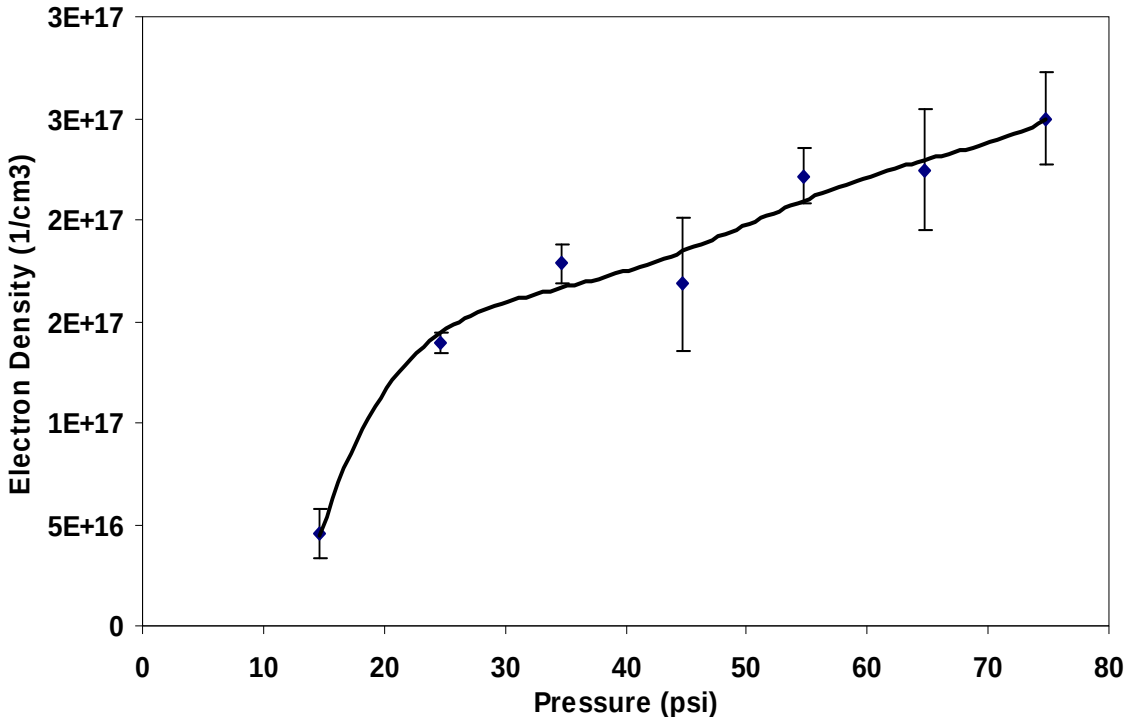

Figure 4.5.

Estimated time-averaged electron density vs. gas pressure.

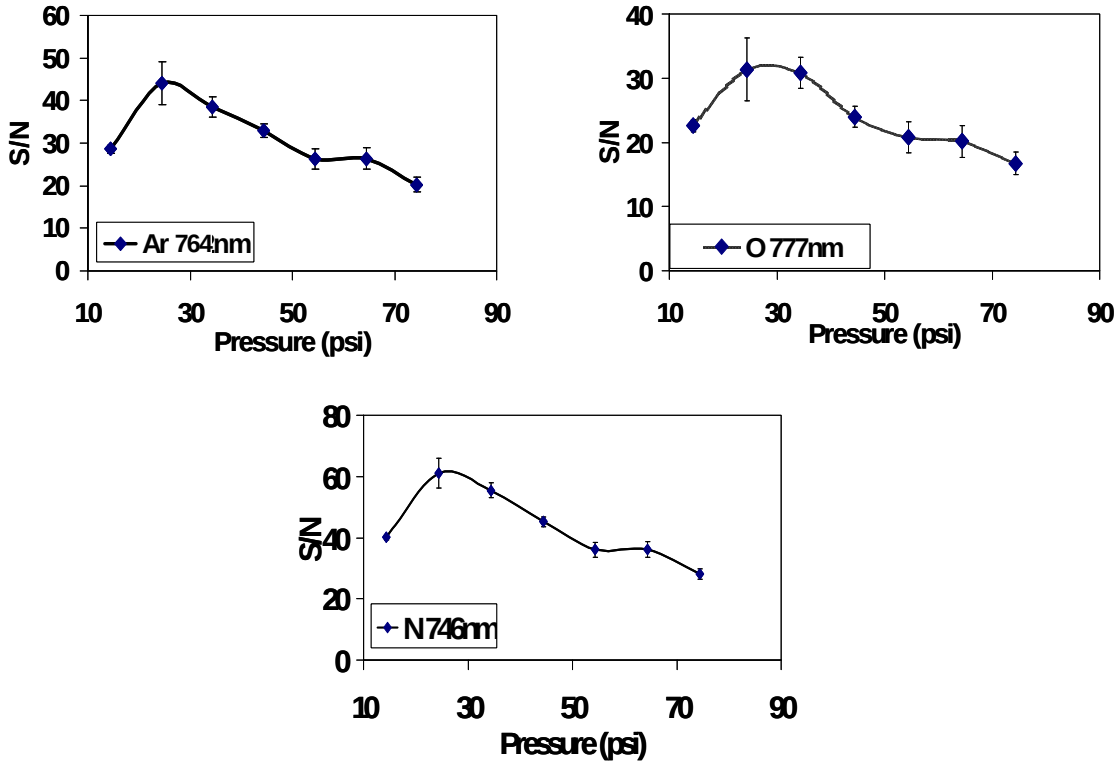

Figure 4.6.

Signal-to-noise ratios (S/N) obtained from LIBS spectra of H_2 mixture (O_2: 0.08 %, Ar: 1.00 %, N_2: 2.00 %) at different gas pressures.

4.2.1.3 Calibration

To quantitatively measure impurities in hydrogen, calibration data of the impurities need to be collected. To obtain calibration data for nitrogen, oxygen and argon, gas mixtures of different concentrations have been prepared by mixing pure hydrogen gas with a commercial H_2 mixture that contains 1.9% N_2 , 0.1% oxygen and 1% Ar in the sample cell. The gas pressure in the sample cell was fixed at 850 Torr for collecting calibration data. Calibration curves of N (746.83 nm), O (777.25 nm), and Ar (763.5 nm) lines at different concentrations were obtained using peak heights and using relative intensity ratios (using H_α line as reference line). Both the peak height calibration and

peak height ratio calibration are shown in Figure 4.7. Both calibration methods give reasonably good linear correlations ($R^2 \sim 0.98$ or better). Experimental fluctuations can significantly affect LIBS signals, but their influence can be eliminated by using calibration curves with the ratio of the reference sample intensity to the emission line intensity. Therefore, an intensity ratio method is preferable in practical applications, such as implementing LIBS technique at the NASA/SSC test site. The analytical performance of LIBS (accuracy and detection sensitivity) using a miniature spectrometer were further evaluated by analyzing LIBS data from different hydrogen mixtures. The predicted O_2, N_2, and Ar concentrations using LIBS calibration peak heights and peak height ratios are both shown in Figure 4.8. Both calibration methods give reasonable good results with an average relative accuracy of 4.5% for peak height analysis and 3.9% for peak ratio analysis.

The calibration data allows us to calculate the minimum impurity species in hydrogen that can be detected with the current LIBS system.

LOD (limit of detection) values were calculated from the following equation:

$$\mathrm{LOD} = 3\sigma / s \tag{4.3}$$

Where, σ is the standard deviation of the background and s is the calibration slope.[72] LOD values determined using the data shown in Figure 4.7 are 797 ppm, 94 ppm, and 1284 ppm for Ar, O_2, and N_2, respectively.

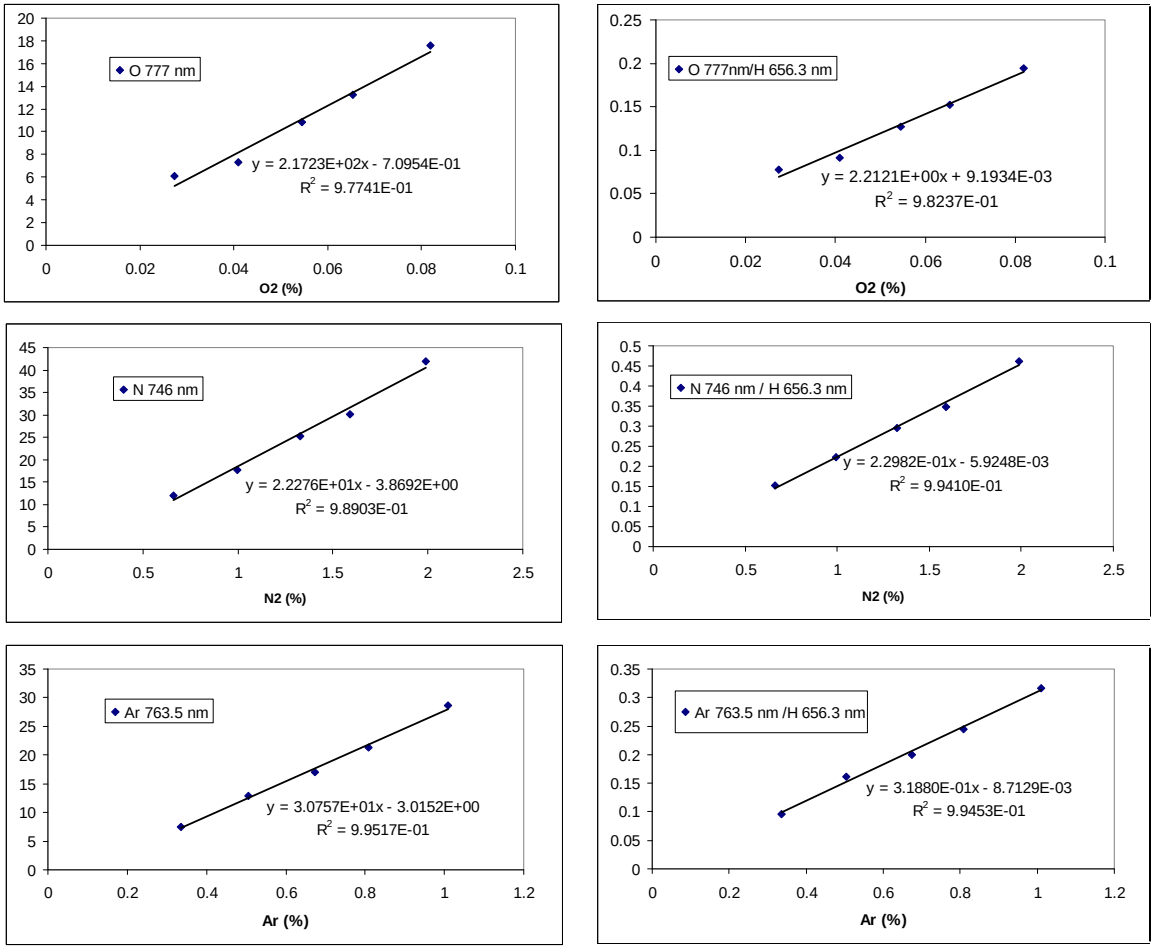

a) b)

Figure 4.7.

Calibration curves for O_2, N_2, Ar in hydrogen. a) Calibration based on peak heights. b) Calibration based on peak height ratios using the H_α line as reference line

.

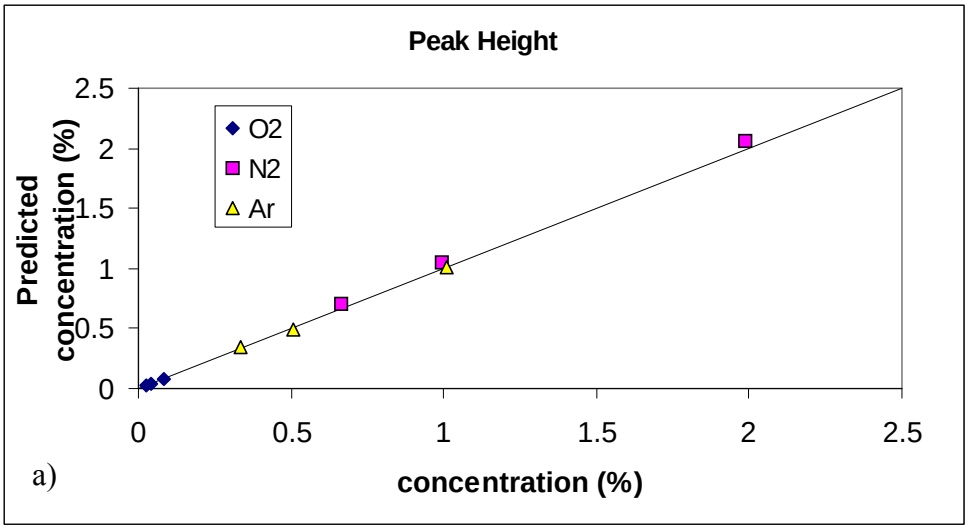

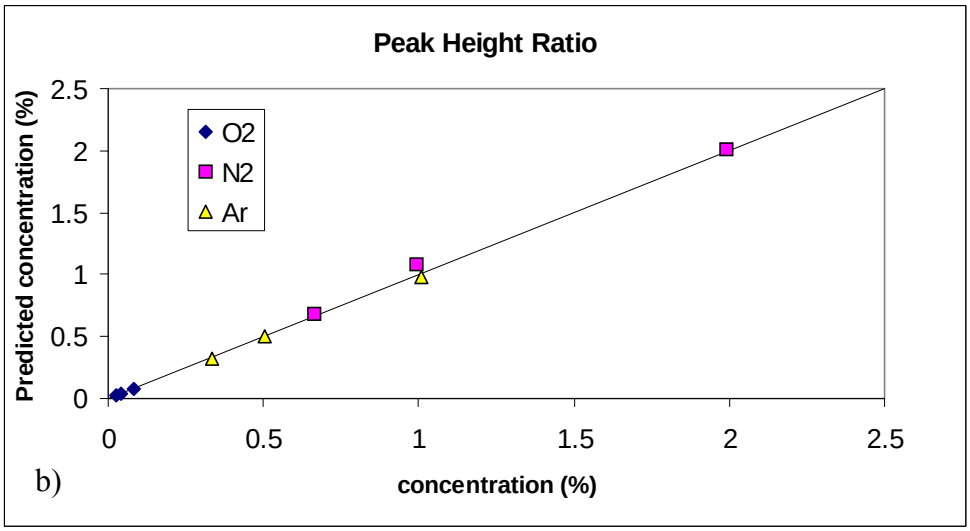

Figure 4.8.

The LIBS measured concentration versus actual concentration. a) using peak height calibration b) using peak height ratio calibration.

4.3 Elemental Analysis of Slurry Samples with Laser Induced Breakdown Spectroscopy

4.3.1. Introduction

Quantitative analysis of liquid samples is relatively challenging. The incident laser beam used to create breakdown generates waves on the surface of the liquid sample.

These waves not only increase shot-to-shot signal variation, but also disrupt the incident laser beam and the emitted LIBS signal by creating aerosols above the liquid surface. Since the laser pulse creates bubbles inside the liquid, these bubbles may reach the surface of the liquid, thereby changing the characteristics of the plasma, which affects the reproducibility of the LIBS measurement.[73] Splashing inside the liquid sample also affects the emitted LIBS signal. Recent research works on the analysis of liquid samples with laser induced breakdown spectroscopy include, but are not limited to, the following reported results. [74-77]

Disposing or destruction of radioactive waste is essential to protect people and the environment. LIBS applications for waste management have been mostly applied to solid samples.[78] Analyzing sludge (liquid radioactive waste) is necessary before storing radioactive wastes for long periods of time.[73] Preliminary results of liquid slurry analysis on flowing system were reported earlier.[79] However, droplets and aerosols above the slurry surface cause fluctuations in the LIBS signal and affect signal intensity and the homogeneity of the slurry flow.[73] For measurement of liquid slurry samples, high laser energy is required to create a plasma in an ablation process and gated detection delays within μm range are needed to analyze the low intensity characteristic emission lines.

In recent years, several researchers have studied samples coated on substrates for elemental analysis using LIBS. Balzer *et al.* used LIBS for thickness measurement and depth profiling of zinc-coated steel sheets.[80] Kim *et al.* used this technique specifically for spectral fingerprinting of paints and coating [81]. We have evaluated thin coating procedure slurry samples on PVC coated glass substrates. LIBS spectra were collected from the prepared dried slurry samples. Quantification of the result was done by applying

univariate and multivariate calibration on the LIBS spectra. Univariate calibration was done on background corrected line intensity. Partial least square methods (PLS) regression was used to for multivariate data analysis. [82-83]

4.3.2. Experimental

4.3.2.1 Slurry Sample Preparation

The slurry that used to evaluate the effect of water on LIBS signal has been prepared by Porrier et. al. [84] This composition was chosen to correspond to waste slurry from the Defense Waste Processing Facility (DWPF). An ICP analysis of this slurry is shown in Table 4.2. To prepare slurry samples of differing compositions, additional amounts of chemicals such as Fe_2O_3, MgO, and SiO_2 were added to the base DWPF slurry. The detail of the DWPF slurry can be found in Reference 73. To prepare dry slurry samples for LIBS analysis, glass slides were first coated with thin layer of PVC, then slurry was applied to the slides (Table 4.3). To dry the slurry, the slurry coated on PVC was put on a 50 °C hot plate for 5 minutes. Coatings are typically about 1 mm thick. Two replications were prepared of each slurry sample.

Table 4.2

Concentration of sludge feed simulants (wt%, liquid)

Elements	w% Concentration
Al	7.37
Ca	2.09
Cu	0.14
Fe	24.2
K	0.042
Mg	0.145
Mn	2.4
Ni	2.67
Si	0.813
Sr	0.085
Zn	0.266

Table 4.3.

Weight % concentration of Fe, Mg and Si in dried base.

	Weight %
Mg_1	1.41
Mg_2	3.02
Mg_3	4.29
Mg_4	4.39
Mg_5	4.75
Fe_1	18.73
Fe_2	19.30
Fe_3	27.53
Fe_4	33.05
Fe_5	38.11
Si_1	0.74
Si_2	3.62
Si_3	6.48
Si_4	8.82
Si_5	11.97

4.3.2.2 Experimental Setup

A schematic diagram of the LIBS setup is shown in Figure 4.9. A frequency-doubled, Q -switched Nd:YAG laser (Continuum Surelite III), is used as an excitation source. The 30mJ laser pulse at 532 nm was focused onto the sample with a 30-cm focal length fused silica convex lens to produce laser induced plasma. The LIBS signal was collected in the backward direction by focusing it into a 100-micron optical fiber. An Andor Technology (Mechelle ME 5000) broadband spectrometer (200-975 nm spectral range) integrated with an ICCD detector was used as the detection system. Solis software from Andor Technology was used to control the detection integration time, gate delay, and gate width (t_w). All spectra were collected at 1 μsec gate delay and a 5 μsec gate width. Each recorded spectrum is the accumulated result of 10 laser pulses. A total of 10 spectra are recorded for each sample. While recording the spectra, the sample was continuously rotated at 1 rotation per 50 seconds to avoid repeatedly hitting same spot on the sample surface.

4.3.2.3. LIBS Data Analysis

LIBS data was analyzed using both univariate and multivariate analysis. This study was focused on three important constituents of the slurry (i.e., Si, Fe, and Mg). Univariate calibration was performed on interference-free emission lines selected after close observation of the LIBS spectra. If the select analyte line has spectral interference due to self absorption or overlapping, the correlation between line intensity and analyte concentration will be complicated. The performance of this calibration was evaluated on

the basis of the coefficient of regression (R^2) and the root mean square error in calibration (RMSEC). RMSEC values were calculated with following equation:

$$RMSEC = \sqrt{\frac{\sum_{i=1}^{n}(x_i - y_i)^2}{n}} \tag{4.4}$$

Where, x_i is measured concentration and y_i is the predicted concentration.

Multivariate analysis, which correlates several independent variables with the data, was also applied to these data sets. The multivariate analysis was performed with The Unscrambler® version 9.7 (CAMO, Corvallis, OR, USA) software package. The calibration model was constructed with Partial Least Square (PLS) analysis, which decomposes x and y variables at one time. A detailed description of the calibration method can be found else where.[85] The performance of the model was evaluated on the basis of the number of principal components that the model uses to perform the calibration, the coefficient of regression (R^2) and RMSEC. Test set validation (TSV) was used to validate the constructed calibration model.

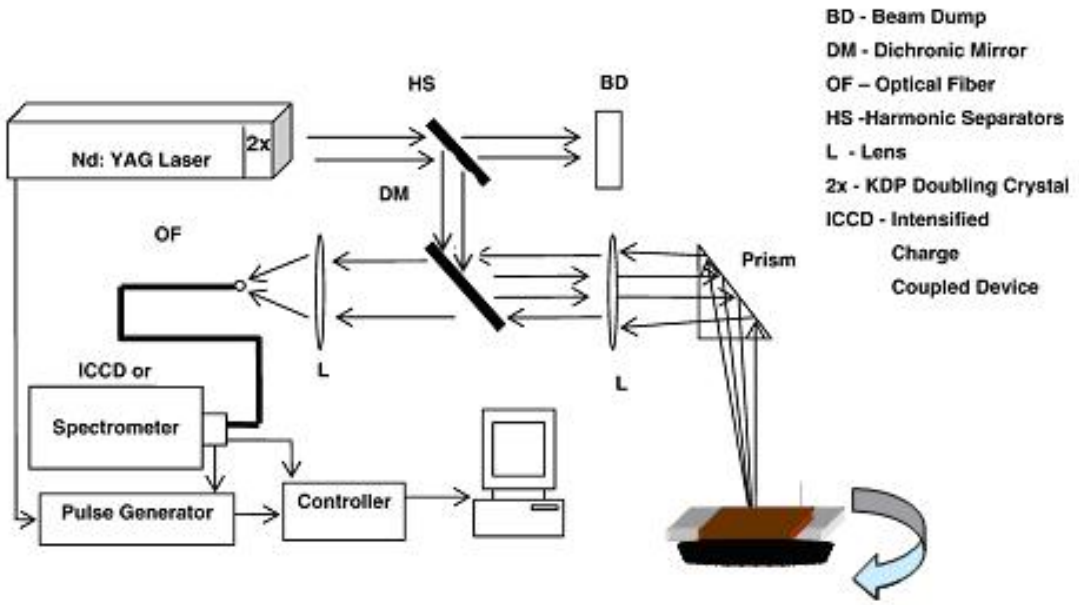

Figure 4.9

Schematic LIBS set-up

4.3.3 Results and Discussion

4.3.3.1 Effect of Water content

The direct analysis of slurry samples using LIBS presents challenges such as sedimentation, splashing, and surface turbulence, which result in large standard deviations. Because water can quench the laser plasma and suppresses the LIBS signal, poor sensitivity may result. We investigated how water content affects the LIBS signal. To study the effect of water on the LIBS signal, we place ~1 ml of slurry in a 3-cm beaker, and then place the beaker in an 80 °C furnace to evaporate some water from the slurry sample. A small amount of the resulting sample was analyzed by thermogravitic analyzer (TGA) to determine the water content left after heating. The rest of the sample

was used for LIBS measurements. The beaker was on a rotating stage during the LIBS measurements to make sure each measurement is from a fresh location.

Figure 4.10 shows LIBS signal obtained from four samples with different drying times. It is evident from the figure that LIBS signal from samples with water content of 71 percent by weight and above are very weak, and the LIBS signal shows significant improvement as the water content decreases. For the Al spectral line at 394.42 nm, the peak line intensity increases almost 10 times when the water content is reduced to a level of approximately 50%. Similar improvements can also be seen in other atomic lines. Improved reproducibility was also observed as the water content in the slurry was reduced. These results motivated us to evaluate dried slurry samples for LIBS measurement.

4.3.3.2 Analysis of Dried Slurry Samples

LIBS spectra of dried slurry samples in the 250 to 550 nm spectral region were studied. This region covers most of the important spectral lines from Mg, Si and Fe; which are the elements of interest. Calibration of the spectral data was performed both with univariate and multivariate analysis.

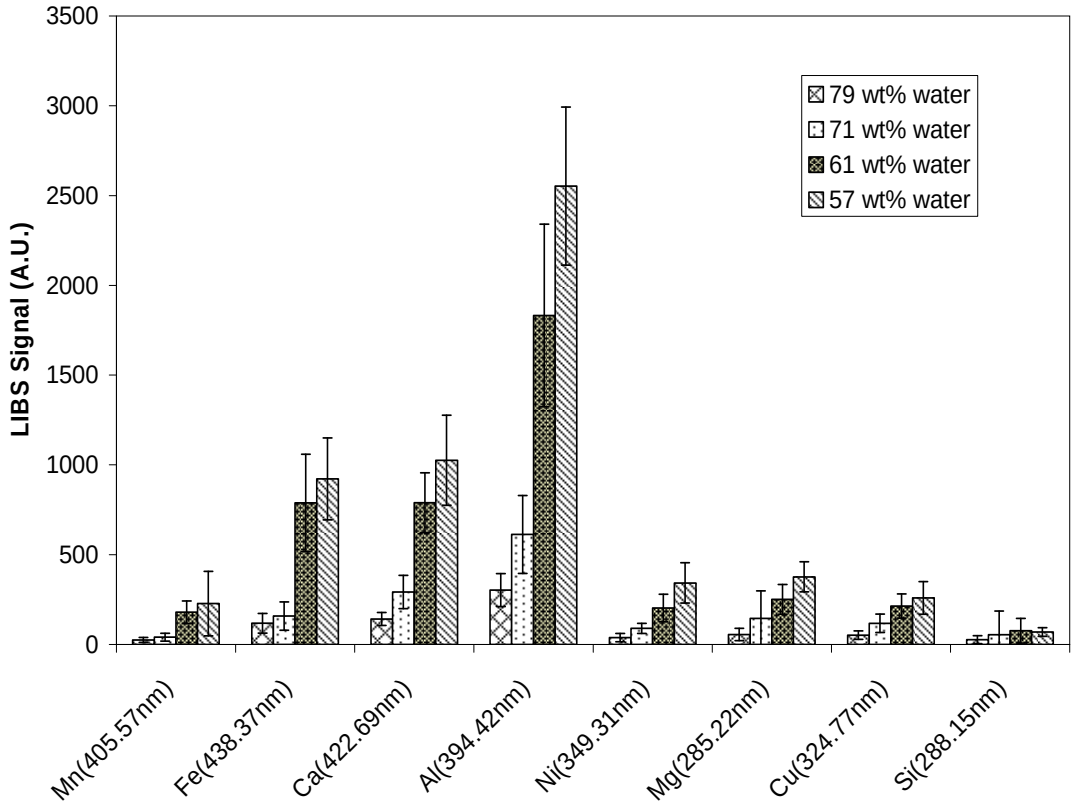

Figure 4.10

Effect of slurry water content on LIBS signal

4.3.3.3 Univariate Calibration

Self absorption is the main concern when selecting spectral lines for univariate calibration. It happens in high plasma density conditions as the plasma itself absorbs its own emission. Mainly ground state resonance lines are affected by self absorption phenomena. The temperature of the plasma drops at the outer surface of the plume. When light passes through that region it is absorbed by the plume. In univariate calibration, only one line per analyte is used.[82] Hence, it is very important to carefully choose the analyte line prior to performing calibration. Relative intensities of the selected lines were compared with data from the NIST atomic data base [68] to determine if self absorption or

other spectral interferences exist. An average spectrum of 10 replications was obtained for each measurement. The final spectra for the univariate calibration were obtained by taking average of the spectra obtained from the prepared two samples with the similar concentration. The line intensity was corrected for the background coming from continuous plasma emission. The background-corrected peak heights were used to establish the correlations with the species concentrations. The spectral peaks of Mg at 280.27 nm, Si at 288.15 nm and Fe at 561.6 nm were used. The results of univariate calibration for Mg, Si, and Fe are shown in Figure 4.11. Although R^2 for this calibration is good ($R^2 > 0.85$), still the RMSEC values are very high. For instance, the calibration result for Mg at 280.27 nm has a RMSEC of 0.67%, which is pretty large, given that the samples all had Mg concentrations of less than 5%. To improve the calibration results, we tried multivariate data analysis.

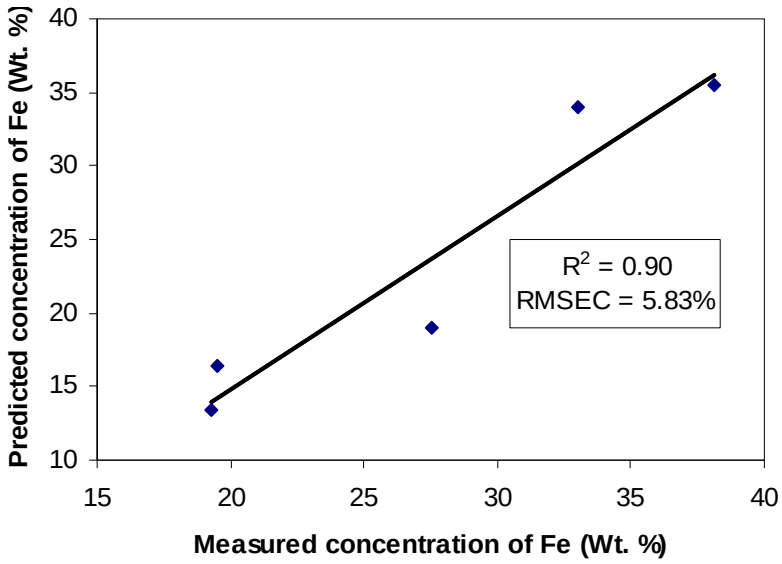

a)

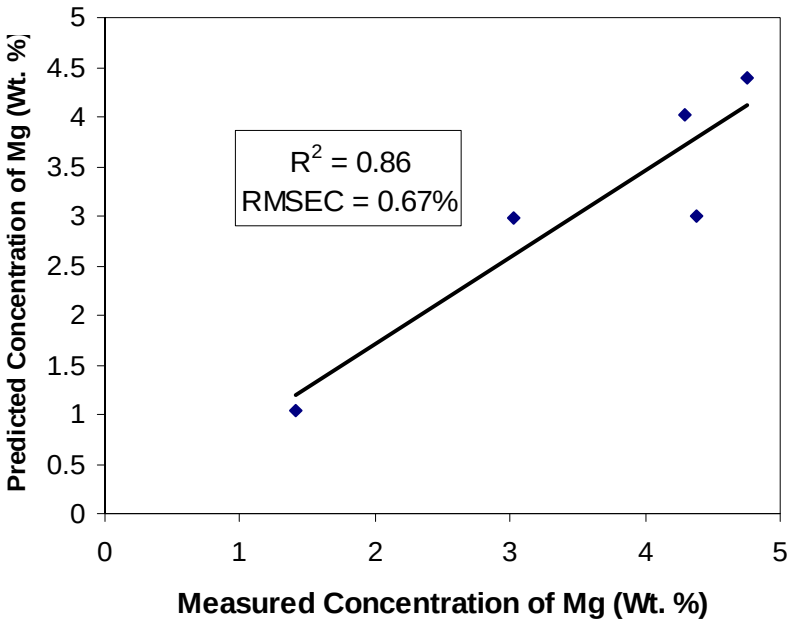

b)

Figure 4.11

a) Univariate calibration of Fe atomic emission lines at 561.6 nm b) Univariate calibration of Mg atomic emission lines at 280.27 nm c) Univariate calibration of Si atomic emission lines at 288.15 nm

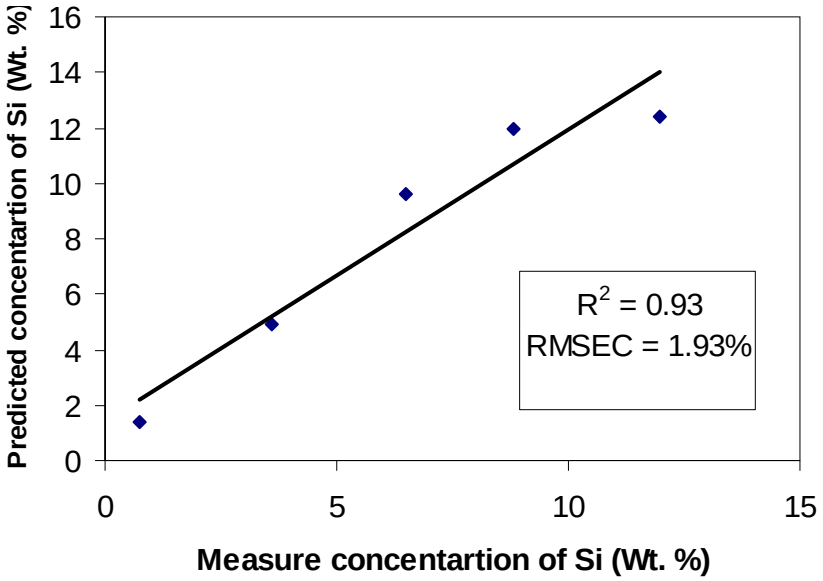

c)

Figure 4.11 (continued)

4.3.3.4 Multivariate Calibration

A multivariate calibration was developed using raw spectra and the whole spectrum approach as reported in the literature.[86] In this work, two set of samples were at each concentration. One set was used to make calibration model and second set was used for validating the model with test set validation (TSV). Calibration was done with partial least square (PLS) regression. PLS analysis simultaneously uses variation in data from the explanatory X-variable (spectral intensity) and response Y-variable (measured concentration) to find new principal components for the regression, which are more related to the variation in the response *Y*-variable. The explanatory variable (spectral intensity) is then linearly regressed on these new principal components (PC's) to determine the maximum variation response variable (measured concentration). Figure 4.12a shows the PLS calibration result for Mg. This calibration model was constructed

with 2 principal components. The coefficient of regression for this model was 0.99, a significant improvement compared to the univariate calibration where coefficient of regression was 0.86. RMSEC for this model was 0.01. The PLS regression model for Si is shown in Figure 4.12b. This model was constructed with 2 PC's and the coefficient of regression was 0.99. RMSEC for the calibration improved from 1.93% to 0.27%, compared to univariate calibration. The calibration result for Fe is shown in Figure 4.12c. 2 PC's were used to construct this model. The coefficient of regression was 0.99 and RMSEC 0.24. A comparison of the multivariate and univariate calibration results is shown in Table 4.4.

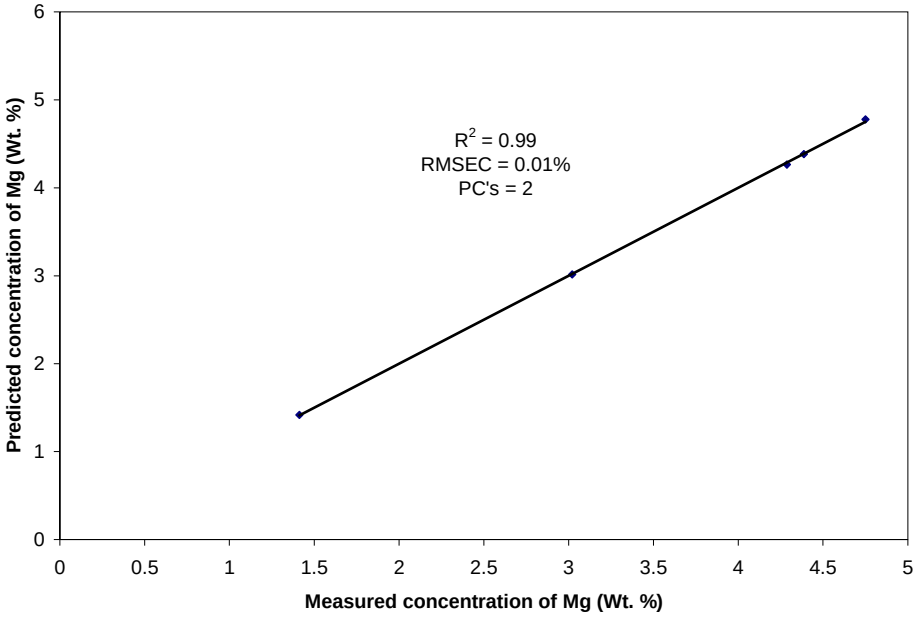

a)

Figure 4.12

a) Multivariate calibration plot for Mg concentration b) Multivariate calibration plot for Si concentration c) Multivariate calibration plot for Fe concentration

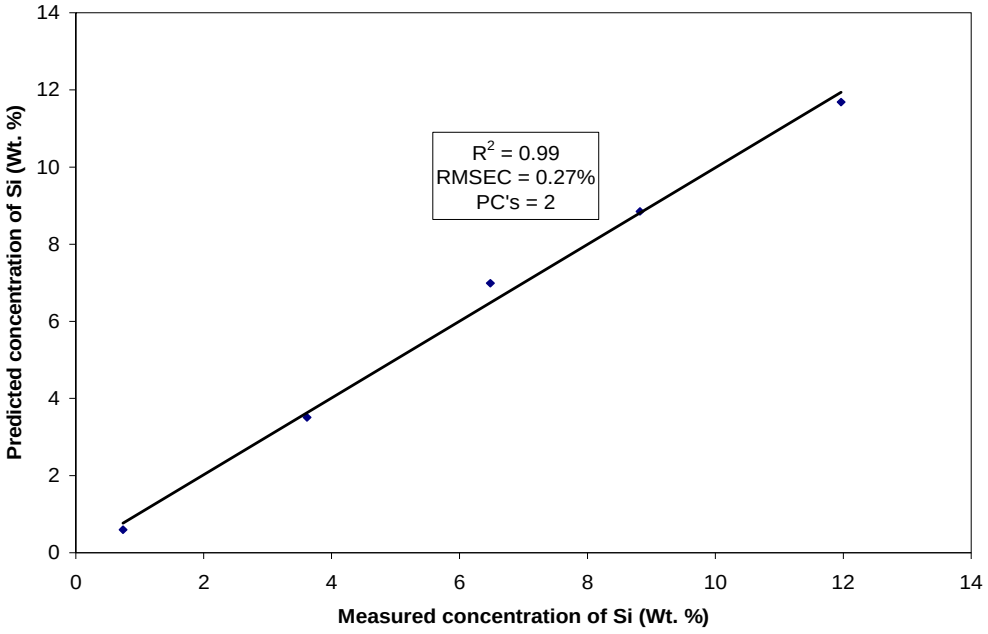

b)

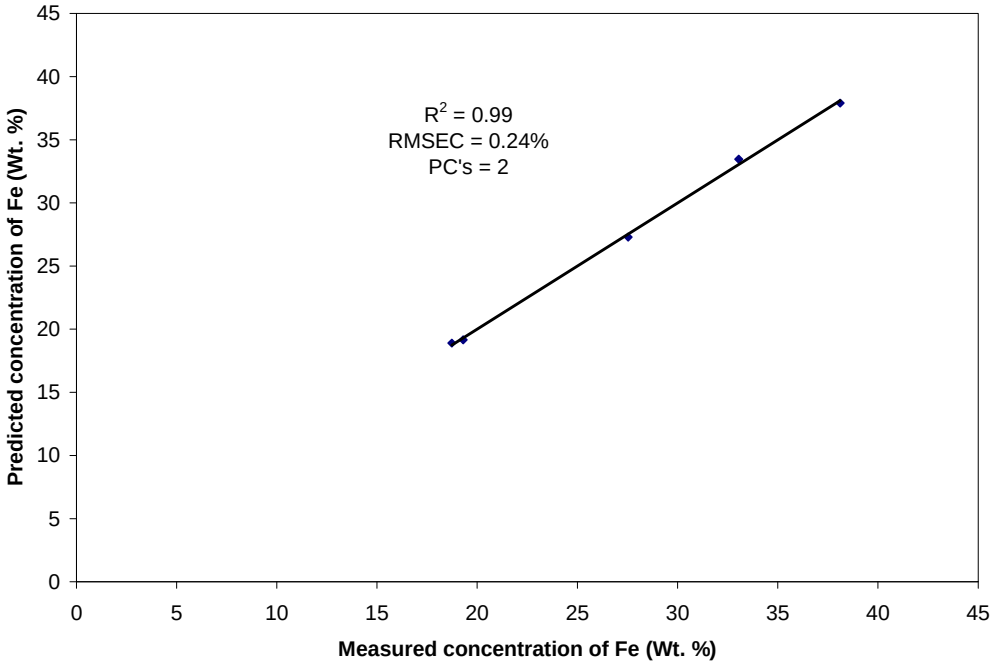

c)

Figure 4.12 (continued)

Table 4.4

Comparison between univariate and multivariate calibration.

	Mg		Si		Fe	
	Univariate	Multivariate	Univariate	Multivariate	Univariate	Multivariate
RMSEC (Wt. %)	0.67	0.01	1.93	0.27	5.83	0.24
R^2	0.86	0.99	0.93	0.99	0.90	0.99
PC	-	2	-	2	-	2

CHAPTER V

LASER SENSOR FOR COMBUSTION DIAGNOSTICS

5.1 Introduction

Combustion diagnostics increase the understanding of fundamental combustion and help the development of a combustion system that can take energy conservation and environmental protection into account. Laser-based diagnostics technique can provide non-intrusive measurements and are suitable for combustion diagnostics. The commonly used laser spectroscopic techniques for gas temperature and species concentration measurement are Laser-Induced Fluorescence (LIF), Laser Raman Scattering (LRS), Coherent anti-Stokes Raman Spectroscopy (CARS), and Cavity Ringdown Spectroscopy (CRDS). Recently some work on Laser Induced Breakdown Spectroscopy (LIBS) applications to combustion diagnostics that have been reported. These show that combustion characteristics and the amounts of pollutant species can be directly determined by LIBS. [87-93] LIF is a commonly used method for measurements of species in combustion applications, such as in flames. There are major difficulties in predicting the concentrations of OH, CH, H, N and O radicals. NO radicals in flames cause changes in flame chemistry, which induces CH and NO concentration changes.[94] CH can be easily measured by CRDS.[95] CRDS is an optical absorption technique that enables detection of species concentrations in a flame. CH radical concentrations in flame studies were monitored using the CH $A^2 - X^2\prod$ transition.[96] Electronically excited CH and OH radicals

are detected by chemiluminescence, yielding measurements of absolute concentrations.[97-98] Coherent Anti-Stokes Raman Spectroscopy (CARS) is a useful technique for determining species that can be identified above the noise level. Hahn and Eckbert measured CO concentrations in flames using broadband CARS, which is applicable even in unstable conditions.[99] However CARS requires practical understanding and rather expensive equipment to measure concentrations.

Combustion particulate emissions are one of the major environmental concerns of diesel engines. The emitted particulate matter is mainly composed of soot which is recognized as the main substance responsible for smoke opacity. The soot volume fraction has been measured using gravimetric and light extinction techniques. Recently, Laser Induced Incandescence (LII) has also been used to measure soot volume fractions in premixed and diffusion flames. [23, 100-103]

In this work, both LII and LIBS have been studied for combustion diagnostics. The equivalence ratios of a CH_4/air flame and a biodiesel flame were measured with LIBS and the details of this work are presented in Section 5.2. Studies of LII for soot volume fraction measurements from a soot generator and from a CH_4/air flame with LII were performed and the details are given in Section 5.3.

5.2 Diagnosis of Biodiesel Flame with LIBS

Several spectroscopic techniques have been used to measure equivalence ratios of engines. Those include LIF, Raman spectroscopy, Fourier transform infrared (FTIR) emission spectroscopy.[104] Raman spectroscopy has been used to measure N_2, and O_2 concentrations in unburned fuel. CO, CO_2 concentration measurements and chemical

balance equations have been used to calculate the air/fuel ratio.[105] Ferioli *et al*. have investigated LIBS as a means to measure the equivalence ratio of combustion flames using C, N, and O emission lines.[106-107] A ratio of H_α to O triplet lines was first investigated by Phuoc and White.[108] The equivalence ratio of premixed flames can be obtained by determination of the atomic number densities of hydrogen and oxygen in flames.[67,109,110] The LIBS determination of the equivalence ratio of laminar premixed flames was first reported by Stavropoulos *et al*.[109] Detectors used in LIBS experiments are generally operated in the gated mode, in which a pulse generator is used to control the gate delay and gate width of experiments in order to maximize the signal-to-background (S/B) and signal-to-noise (S/N) ratios.[13] All equivalence ratio measurements in all previous LIBS studies were determined using a gated detector. In this work, an ungated detection system was demonstrated for LIBS measurement of the equivalence ratio of biodiesel and methane/air flames.

Biodiesel provides a possible alternative to fossil fuel. It is considered to be environmentally friendly, non-toxic, and has no sulfur content. Biodiesel reduces emissions of carbon dioxide (CO_2), organic compounds, unburned hydrocarbons (UHC), sulfur oxides (SO_x), carbon monoxide (CO), polycyclic aromatic hydrocarbons (PAHs), and nitrated polycyclic aromatic hydrocarbons. Therefore, the use of biodiesel might significantly reduce emissions that contribute to global warming, increases engine life with its superior lubricating properties, and be non-toxic.[111] Biodiesels are mostly produced by a transesterification process that employs three types of chemical reaction conditions, such as a strong alkalis, acids, or enzymes.[112- 113]

5.2.1 Experimental Details

5.2.1.1 LIBS Apparatus

The laser beam is focused inside a flame by a 10-cm focal length fused silica planoconvex lens to produce laser-induced sparks. A frequency-doubled, pulsed Nd:YAG laser (Big Sky, model CFR 400) (532 nm, 189 mJ, 9-mm diameter, 10 Hz) is used as the excitation source; it can deliver laser energies up to 189 mJ per pulse. For initial study of biodiesel flames, measurements were performed using a gated detector. LIBS signals were collected in the backward direction with the same focusing lens and were focused into an optical fiber with the fiber's distal end attached to a 0.5-m spectrograph (SPEX 500M, 2400 lines/mm diffraction grating) (see Figure 5.1a). A 1024-element intensified diode array detector (IDAD) (PARC, model 1456) was mounted on the spectrograph. Both gate delay and gate width were controlled by a pulse generator (Princeton Instruments, model PG-10) which was synchronized with the laser. EG&G OMAVISION PC software was used for data acquisition. The spectral coverage with this gated detection system is 20 nm. The LIBS flame sensor used was an ungated, miniature fiber optic spectrometer (Ocean Optics, model USB2000, 2048-pixel linear silicon CCD array, 1200 l/mm grating) to record LIBS flame data. The LIBS emission signals were collected in both 90^{o} and in the backwards direction by an optical fiber pickup lens and UV-compatible optical fiber and sent to the miniature spectrometer (see Figure 5.1b).

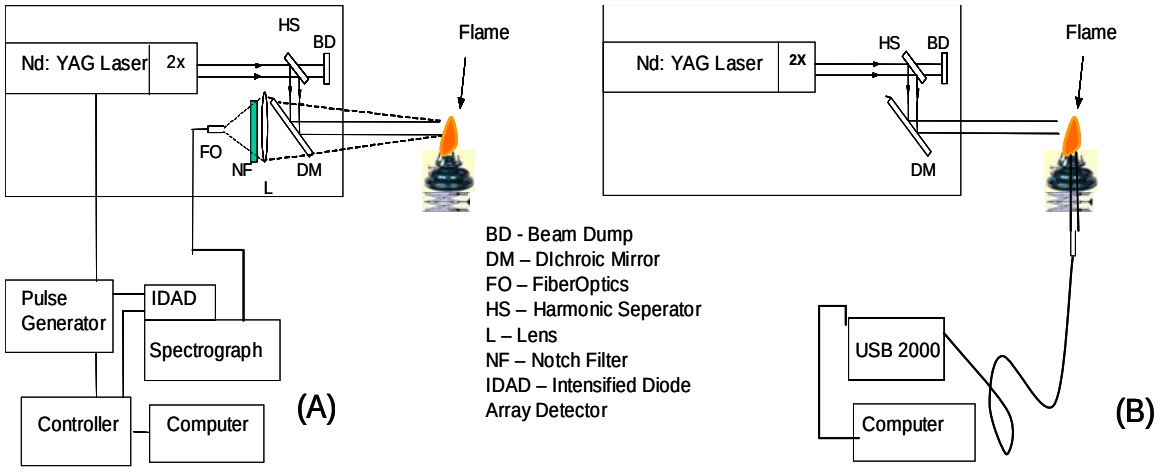

Figure 5.1.

LIBS Experimental set up (a) with gated, (b) without gated detector

Since, there was higher background in the backward collection set up, the data from the 90^{o}-collection set up was analyzed. Data analysis was performed using Ocean Optics SpectraSuite software. The spectrum from 540 - 850 nm can be simultaneously acquired with this LIBS sensor.

5.2.1.2 Methane/Air Flame

A stainless steel Bunsen burner was used to maintain a premixed methane/air flame which had 8-inch (20-cm) height and 2-inch (5-cm) diameter. Methane (99.9%) and air (21% oxygen) were mixed in a burner with the help of calibrated flow meters. LIBS measurements of the methane/air flame were recorded with an air flow rate of 5 liter per minute (LPM) and methane flow rates between 1.0 and 2.3 LPM. The laser was focused on the radial center and axially ~1 cm above the burner.

5.2.1.3 Biodiesel Flame

The biodiesel flame was produced using a commercial oil lamp, which consists of a cylindrical vessel 4-inches (10-cm) in diameter and 2-inches (5-cm) high with a cotton wick. LIBS measurements of biodiesel flames were performed at different radial and axial locations (radial width from 0 to 7 mm and axially upward from 0 to 5 mm) to study the structure of biodiesel flames. The flame on a wick is a typical diffusion flame which consists of four different zones, such as dark zone, C_2 and CH zone, luminous zone, and main reaction zone.[114] The efficiencies of the biodiesel flame with 50% to 100% ethanol concentrations in the biodiesel were also recorded and compared.

5.2.2 Results and Discussion

5.2.2.1 Methane/Air Flame

The stochiometric relationship of methane/air flames was obtained from [67]

$$CH_4 + 2\left(O_2 + \frac{0.79}{0.21}N_2\right) \rightarrow CO_2 + 2H_2O + \frac{1.58}{0.21}N_2 \tag{5.1}$$

The equivalence ratio can be calculated from the relative fuel and oxidizer concentration ratios in terms of mass or of moles. Thus, the fuel-to-oxidizer ratio divided by the stochiometric fuel-to-oxidizer ratio gives the following relationship.[67]

$$\Phi = \frac{m_{fuel} / m_{air}}{(m_{fuel} / m_{air})_{stochiometric}} \tag{5.2}$$

LIBS spectra of CH_4/air flames can be used to determine the elemental concentrations of N, H and O in flames. Since H is mainly from fuel and O is from air, we can estimate the equivalence ratio for premixed flames using the concentration ratio of H to O atoms divided by the stochiometric relationship of methane/air flames.[115]

LIBS spectra of CH_4/air flames with different flow rates of methane to air were recorded to obtain a calibration curve for flame equivalence. LIBS spectra were obtained using 120-mJ laser pulse energy. The intensity ratios of H to O from different mixtures of methane/air flames are presented in Figure 5.2. It shows a linear relation between the intensity ratio of H to O lines and the calculated equivalence ratio for premixed methane/air flames. The results obtained from the ungated LIBS sensor are similar to that obtained with a gated detector in previous studies.[67, 109] This study shows that this miniature LIBS sensor has the capability of monitoring the equivalence ratio of flames using the measured intensity ratio of H to O lines.

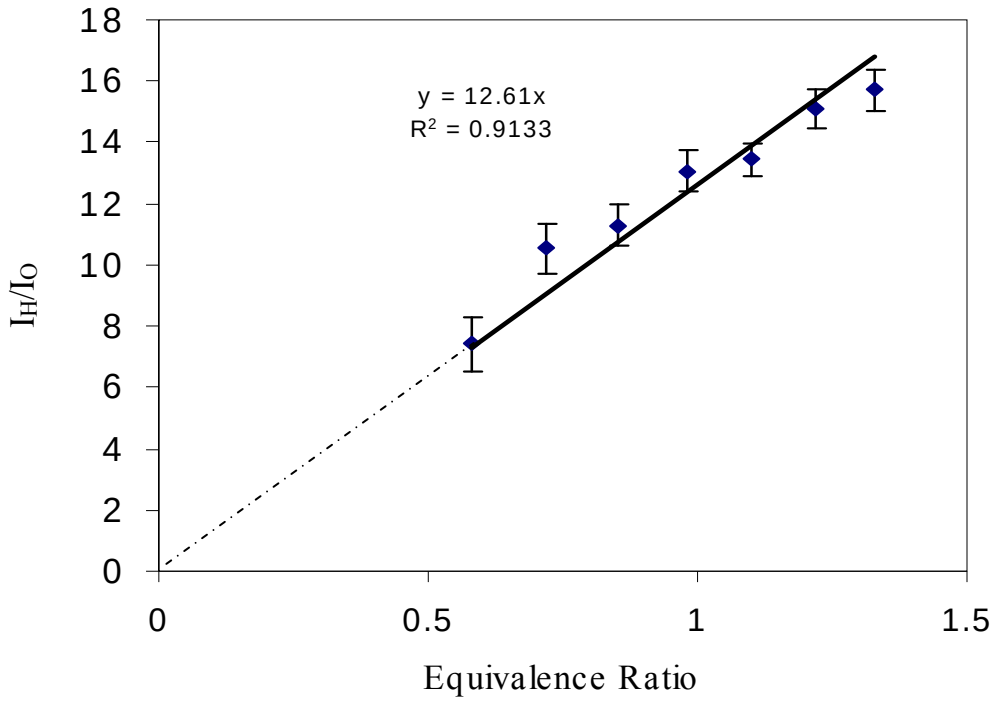

Figure 5.2.

Correlation of the Equivalence ratio of methane/air flame with the intensity ratio I_H/I_O.

5.2.2.2 Biodiesel Flame

The biodiesel flame is much more complicated flame than the methane/air flame. The stochiometric relationship for biodiesel flame is very difficult to formulate. This work is the first attempt to use LIBS to characterize the biodiesel flames using gated and ungated detection. LIBS spectra of biodiesel flames were obtained using 120-mJ laser pulse energy. The continuum background that is emitted while the laser spark is formed depends on the signal strength of the plasma. Since the plasma cools in very short time, it emits a characteristic signal that has information about the elemental concentrations of

species present. Since the continuum radiation decays much faster than the characteristic radiation, we can select a data acquisition time (i.e., the delay between the laser and detector gate width) that gives the best signal-to-background ratio (S/B) data. Gated detection not only allows one to select an optimum data acquisition time, but also discriminates against any unwanted continuum background from the test environment, such as the flame. The optimum gate delay for LIBS is generally below 10 μs. The optimum experimental parameters for flame detection with gated IDAD detection were found to be 5-μs gate delay time and 10-μs gate width for biodiesel flame. To study the distribution at horizontal positions, LIBS spectra have been recorded of the H spectral line at different horizontal positions 1 mm above the wick of the biodiesel flame (see Figure 5.3). The spectral shape and intensity of the H_α line are similar at these measurement locations. It indicates no significant variation in H concentration in horizontal position. At this height, H line intensity shows no change inside the flame. Stavropoulos *et al*. measured the radial distribution of a premixed laminar flame which shows different equivalence ratios in different radial distributions.[67, 109] Since it has complicated chemical structure, it is different from actual fossil fuels.

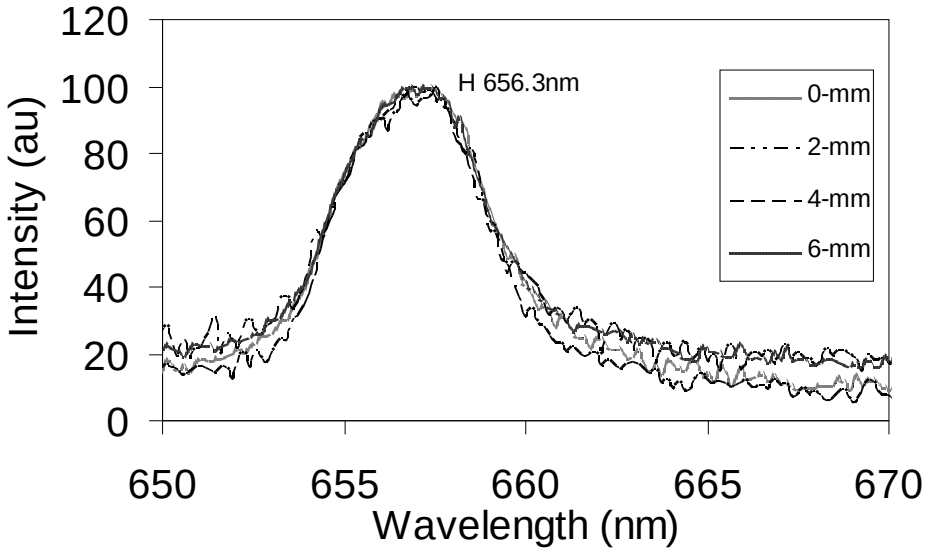

Figure 5.3.

LIBS spectra of H spectral line in biodiesel flame which were detected by IDAD gated detector.

LIBS data of biodiesel flames obtained with an ungated, miniature detector show strong flame emission background as shown in Figure 5.4(a). The flame emission spectrum recorded with the same experimental parameters with the laser off is also shown in Figure 5.4(a). It is clear that the recorded LIBS spectra of biodiesel flames have poor signal-to-background ratio (S/B) due to the interference of flame emission. To improve the S/B of LIBS for biodiesel flames, a data processing technique was developed to improve the S/B ratio. Experimentally obtained flame emission was used as a background spectrum. Since the flame emission spectrum varies with time, a linear background fit method was adapted in order to effectively subtract the flame emission from LIBS flame spectra. Only part of the flame spectrum was fitted with the LIBS spectrum to determine the scaling factor for background subtraction. The raw LIBS spectra were then subtracted from the scaled emission background. The background

subtracted LIBS spectrum of a biodiesel flame is shown in Figure 5.4(b**).** With this simple approach, we can use an ungated miniature spectrometer to develop a LIBS sensor for biodiesel flames.

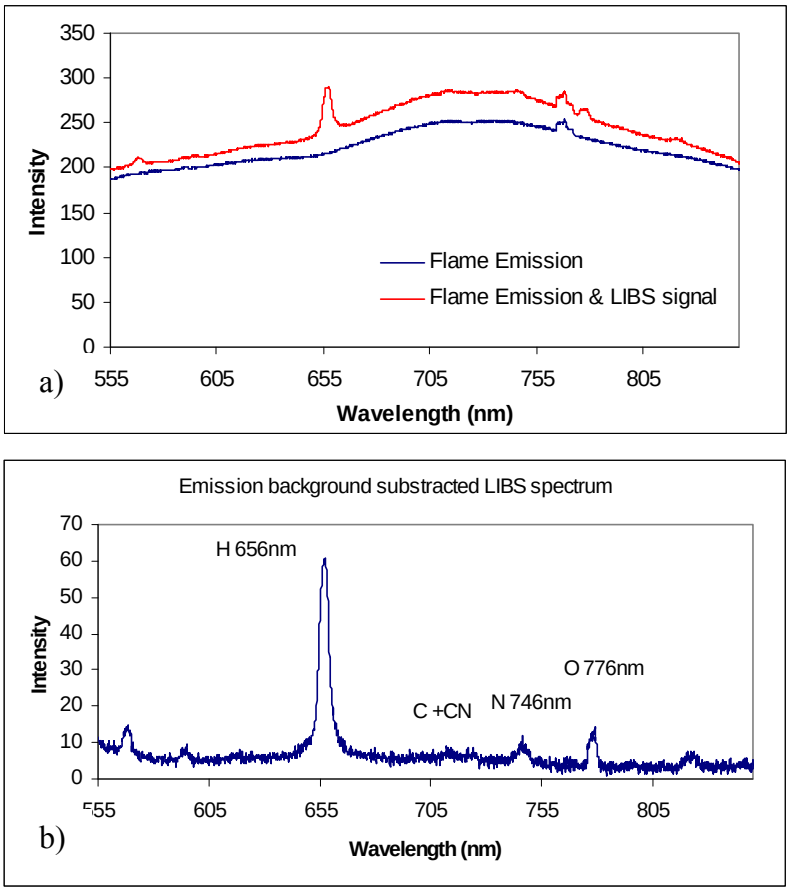

Figure 5.4.

LIBS spectra of biodiesel flame with ungated detection. (a) Raw data and (b) background subtracted spectrum.

To characterize the biodiesel flame with the LIBS sensor, LIBS data of biodiesel flames at the center of the flame and at different heights above the oil lamp were recorded. Figure 5.5 shows that the intensity ratio of H to O lines changes with height

above the oil lamp. Each data point shown in Figure 5.5 is an average of 20 spectra. Standard deviations of those measurements are represented by error bars. As height above the wick increases, the amount of carbon increases in the luminous zone. Soot and other species would affect the H/O ratio. For comparison purposes, diffusion flames of biodiesel with ethanol have also been investigated. LIBS spectra from the flames of different mixtures of biodiesel and ethanol were recorded. It was found that different ethanol concentrations in biodiesel have considerable effect on the intensity ratios of H to O lines in flames. It shows that the intensity area under the H/O lines decreases as ethanol concentration increases (see Table 5.1). Decrease in NO_x emission and amount of H_2O formation from ethanol may have an effect on decrease in H/O ratio.[114, 116]

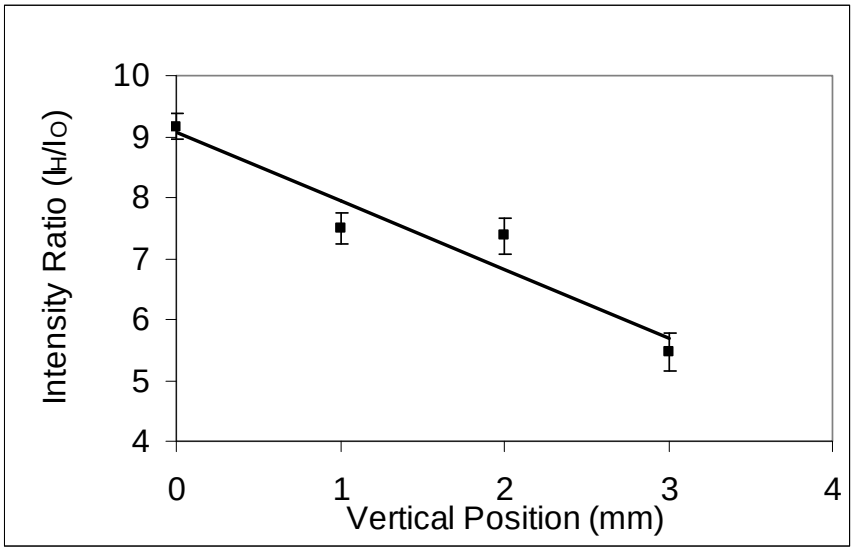

Figure 5.5

Intensity ratio of a biodiesel flame at different heights above burner.

Table 5.1.

Area intensity ratio (H/O) change with ethanol concentration in biodiesel flame

Ethanol concentration in biodiesel (%)	Area Intensity ratio (H/O)
0	0.896
25	0.763
50	0.258

5.3 Soot Volume Fraction Measurements with LII

Laser Induced Incandescence (LII) has been used to measure soot volume fractions (SVFs) in premixed and diffusion flames.[23, 100-103] Since the lifetime of laser induced incandescence depends on the particle size, LII can be used to estimate the soot particle size in flames. Soot particles are formed as spherical primary particles of graphitic carbon and are on the order of a few tens of nm in diameter.[117] Soot formation occurs by hydrocarbon fuels undergoing pyrolysis or partial oxidation during combustion to form small hydrocarbon radicals from which acetylene compounds are formed. Soot primary particles have diameters within the Rayleigh-scattering regime and soot is an excellent absorber and emitter of LII radiation. A pulsed laser is used to rapidly heat the soot particles within the laser beam to the soot vaporization temperature (4000-4500 K) and incandescence emission results.[118] Laser Induced Incandescence combines elastic scattering and line-of-sight techniques. It can be detected by the elastic scattering feature of LII. As the size of the primary soot particles is in the Rayleigh limit for light absorption, the LII signal is proportional to soot volume concentration. Detection of the particles with LII signals depends upon the excitation intensity, the excitation and detection wavelengths, detection timing duration, and the soot volume fraction.[119]

Sensitive LII detection can be obtained only by using a long gate width (microsecond range) and a short gate delay (100ns range). [120-123]

Previous measurements on soot particles, such as by Mie scattering, were resulted in large errors. The LII method is a promising technique for measuring soot volume fractions in flames. In LII, soot particles absorb laser energy and are quickly heated to a high temperature and incandescence occurs. Since the LII spectra can be obtained from a single laser pulse, it offers high temporal resolution. It is a non-intrusive technique, which can hence provide temporally and spatially resolved SVFs in combustion flames. Using an appropriate calibration method for the LII signal, information on the soot volume fraction and primary soot particle size can be obtained.

5.3.1 Theory

LII signal is basically blackbody radiation emitted by hot soot particles. The current LII theoretical model is based on energy and mass conservation of a single primary soot particle of known size. [124- 125] Several assumptions are made to simplify the model. The main assumptions are: (1) soot aggregates consist of single-size spherical primary particles of uniform composition; (2) the physical properties of soot primary particle (i.e. density, heat capacity, and optical properties) are as assumed to be those of a graphite particle; (3) the value of the particle refractive index-dependent function E(m) of soot is independent of temperature; and (4) morphological alteration by laser heating at high laser fluences is ignored.

The spectral radiant emittance of a blackbody is given by Planck's law

$$W(\lambda, T) = \frac{8\pi hc}{\lambda^5} \frac{1}{(e^{hc/\lambda KT} - 1)} \quad \text{W cm}^{-2}\ \mu\text{m}^{-1} \tag{5.3}$$

where T is the temperature (in Kelvin) of the blackbody; h is Planck's constant; c is the speed of light; k is Boltzmann's constant, and λ is the wavelength (in μm).

The particle surface temperature can be obtained from two-wavelength pyrometry using the following equation

$$\frac{I_{\lambda_1}}{I_{\lambda_2}} = \frac{\lambda_2^6 (e^{hc/k\lambda_2 T} - 1) E(m)_{\lambda_1}}{\lambda_1^6 (e^{hc/k\lambda_1 T} - 1) E(m)_{\lambda_2}} \tag{5.4}$$

where E(m) is a particle refractive index-dependent function.

The incandescence from a single primary particle of diameter d_p can be expressed as

$$P_p(\lambda) = \frac{8\pi^3 c^2 h}{\lambda^6 (e^{hc/k\lambda T} - 1)} d_p^3 E(m) \tag{5.5}$$

Since the measured incandescence I_λ equals the number of primary particle (N_p) times the incandescence from a single primary particle $P_p(\lambda)$, the particulate volume fraction (PVF) can be written as

$$PVF = \frac{\pi d_p^3 N_p}{6V} = \frac{\pi d_p^3}{6V} \frac{I_\lambda}{P_p(\lambda)} = \frac{\lambda^6 (e^{hc/k\lambda T} - 1) I_\lambda}{48 V \pi^2 c^2 h E_\lambda(m)} \tag{5.6}$$

where V is the volume measurement defined by the light collection optics and laser cross section. Note that PVF is independent of the primary particle size d_p.

5.3.2 Experimental Details

5.3.2.1 LII Setup

A frequency-doubled, pulsed Nd:YAG laser (Big Sky, model CFR 400) (532 nm, 189 mJ, 9-mm diameter, 10 Hz) is used as the excitation source (Figure 5.6). The laser is either focused (with a 30-cm focal length fused silica planoconvex lens) on the soot or directly shines on the soot particles. To evaluate the detection configuration for the optimum detection limit, both backward (i.e., 180°) and 90° detection have been evaluated. The detection system consists of a 0.5-m spectrograph (SPEX 500M, 2400 l/mm grating, 20nm spectral range) with the LII signal input through a UV-grade optical fiber. A 532-nm holographic notch filter is placed before the optical fiber to reject scattered laser light.

The spectrograph is fitted with a gated, 1024-element intensified diode array detector (IDAD) (PARC, model 1456). Both gate delay and gate width are controlled by a pulse generator (Princeton Instruments, model PG-10) which is synchronized with the laser. EG&G OMAVISION PC software is used for data acquisition. Data covering a 20-nm spectral region is acquired in a single run with a data sampling time of 3 s per spectrum and each sample is an average of 30 single pulse spectra**.** In the 90 degree configuration, a simple fiber pickup and some lens combinations were tested to efficiently couple the LII signal into the fiber. Optimum LII signal was obtained with the lens combinations of one 10-cm focal length cylindrical lens and two 10-cm focal length plano-convex lenses.

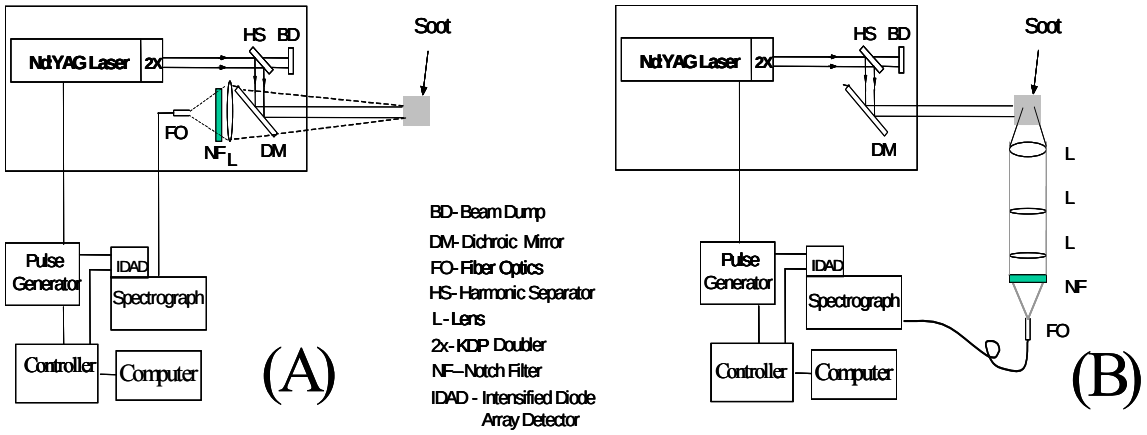

Figure 5.6.

Schematic diagram of LII experiments. a) backward detection; b) 90° detection.

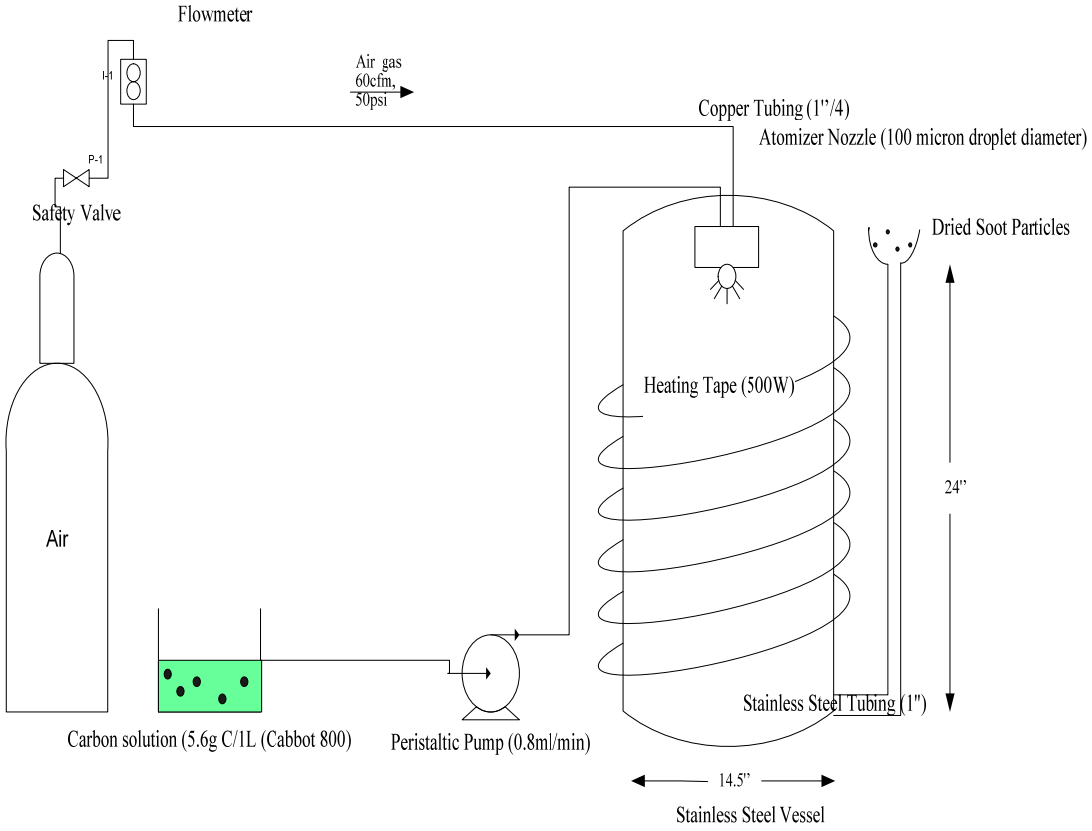

Figure 5.7

Schematic of the soot generator.

In addition to the SPEX 500 spectrometer, two other detection systems for LII measurements have also been used. One is the low-resolution, miniature spectrometer (Ocean Optics, model USB2000) with a CCD detector. The USB2000 doesn't have gating capability. It provides LII spectra from 180-850nm for soot generator measurements. It is helpful for quick evaluations of various experimental configurations and experimental parameters. The Hamamatsu photomultiplier tube (PMT) with an appropriate bandpass filters can be used to monitor LII signals at two wavelengths sequentially (e.g,.Thorlabs 430 nm and 650 nm band pass filters with FWHM=10) at 900V operating voltage. This system can provide a millisecond response time. Hence LII signal has the best enhancement at 430nm and 650nm.

5.3.2.2 Soot Generator

To obtain optimum experimental parameters for soot particle measurements with LII, a home-made soot generator has been built to generate aerosols of carbon black particles. The soot generator consists of a spray nozzle, copper tubing, peristaltic pump, and a stainless steel vessel (Fig. 5.7). The peristaltic pump is connected between the carbon solution container and the nozzle. The nozzle is attached to a 3908-inch^3 stainless steel vessel. Air gas is supplied by an air tank which has 60 cubic feet/hour (cfh) flow rate at 50 psi air pressure. The carbon solution was prepared by mixing 5.6 grams of carbon black (Cabot 800, 220 nm diameter) particles in 1 liter of distilled water. One gram of Arabic gum was added to the carbon solution to keep the carbon black particles suspended in the solution. After the solution was mixed by a magnetic stirrer for one hour, it was sprayed into the stainless steel vessel using a peristaltic pump at a 1 L/min

flow rate. The stainless steel vessel was heated to 100 °C by heating tapes (500 W) to evaporate the water from the droplets and produce soot particles. Dried soot particles then exited from 1"-diameter stainless steel tubing. The spray nozzle (Spraying Systems Corp., model SUJ1A) produces droplets with a mean diameter of approximately 100 microns in this soot generator. A 100-micron droplet containing a suspension of this carbon black in water at a dilution of 5.6 grams per liter is calculated to contain, on average, 2.63×10^5 primary particles per drop. As the water in each drop evaporates, leaving behind carbon black solids, the carbon black particles are expected to agglomerate. Hence, this laboratory soot generator is expected to produce relatively large agglomerates, averaging over 10^5 primary particles each. Each primary particle should be approximately 220 nm in diameter.

The morphology and structure of the soot captured from the soot generator and flame experiments were investigated by Transmission Electron Microscopy (TEM) (JEOL model JEM-100CX II) analysis. The thermophoretic deposition technique was used for the TEM observations. Thermophoretic deposition occurs due to the presence of a temperature gradient in the vicinity of a cold wall inside a flow field of a particle-laden gas. The holder exposure time should be long enough to capture a significant sample, but short enough to expose a cold surface to the flame-born particles. The morphological features provide not only qualitative information on particle agglomeration, surface growth, and oxidation, but also quantitative data on primary particle size.[125] The holder was passed rapidly through the flame and above the soot generator outlet tube in less than 1 s. Average soot particle size was determined by measuring major and minor axis lengths.[126]

5.3.3 Results and Discussion

LII measurements with the soot generator were performed to optimize the system's experimental parameters. Effects of laser fluence, gate delay, gate width, and laser beam focus on the LII signal were studied (Fig. 5.8). The data shows that 100-ns gate delay and 1000-ns gate width are optimum detection windows for LII experiments under our current setup. It was also found that LII spectra obtained with an unfocused laser beam have a higher intensity compared with those with a focused beam (see Fig. 5.9). The experiment with the focused laser beam has higher fluence due to the smaller focused spot size. Therefore, only limited laser energy can be used in this setup to eliminate the problem of particle induced breakdown (PIB). Also, the setup using the focused laser beam has a smaller interaction volume (i.e., fewer soot particles) and therefore less LII signal results. On the other hand, the unfocused laser beam can cover a larger active volume (i.e., more soot particles) and higher laser pulse energy can be applied without the problem of PIB.

Since the data show that the optimum LII signal is obtained with an unfocused laser beam setup, this experimental setup has been used to record LII spectra with various laser energies. A soot density of about 3.58×10^{-8} g/cm^3 produced by the soot generator was excited by the unfocused laser beam. LII signal increased with increasing laser fluence from 0.1 –0.2 J/cm^2. The LII signal intensity reaches a plateau region for fluences above 0.2 J/cm^2 (see Fig. 5.10). This indicates that the energy absorbed by the soot particles in the plateau region is not sensitive to variation of the laser fluence.

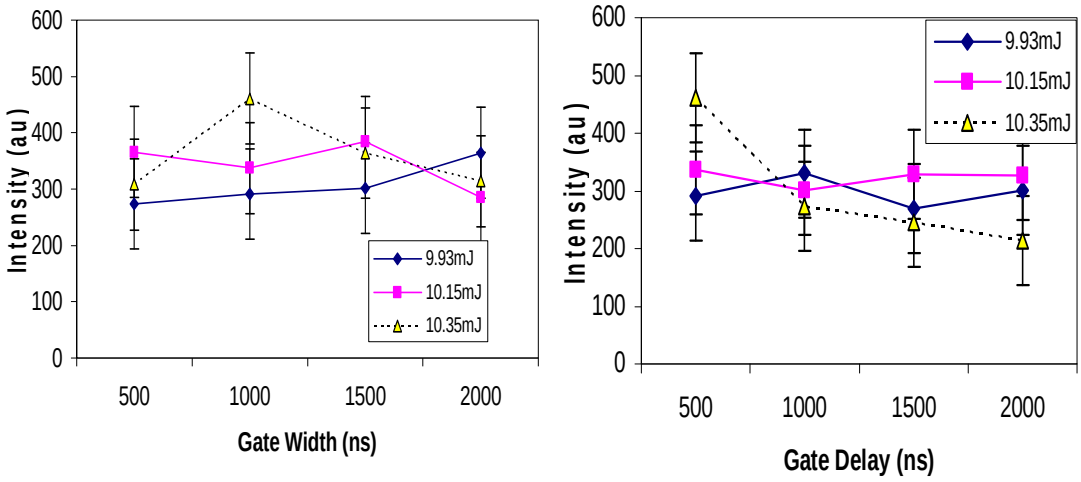

a) b)

Figure 5.8.

Effect of the detection window on the LII Signal. a) 100-ns gate delay. b) 100-ns gate width.

The easy aligned backward detection configuration (Figure 5.6a) was used to optimize the detection time window and laser fluence for LII measurements. To determine the optimum LII detection configuration, the 90 degree detection configuration has been evaluated (Figure 5.6b). Comparing the LII signal obtained from backward detection and 90° detection, it was found that 90° detection provides better signal-to-noise LII signal (~2 times higher). The 90° configuration has also been evaluated to be the most efficient way to couple the LII signal into the optical fiber. A simple fiber pickup lens and some lens combinations were tested to couple the LII signal into the fiber. It was found that the optimum LII setup was obtained with the lens combinations of one 10-cm focal length cylindrical lens and two 10-cm focal length plano-convex lenses.

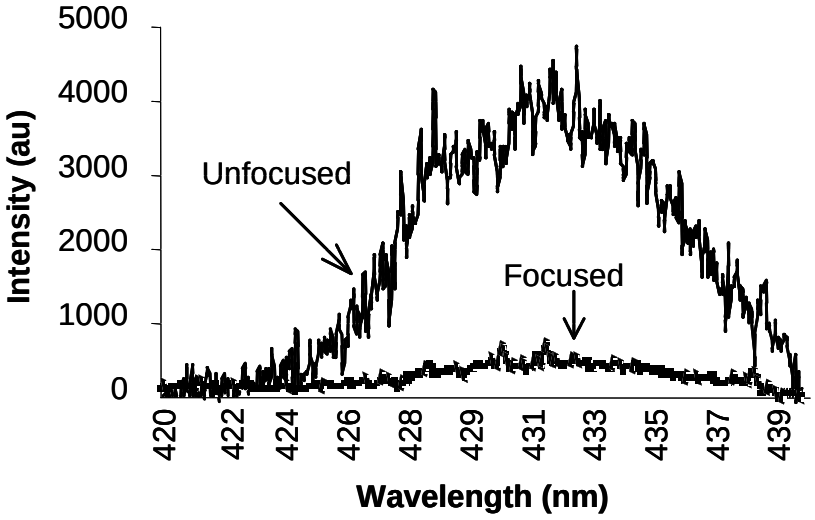

Figure 5.9

Effect of laser focusing on LII signal

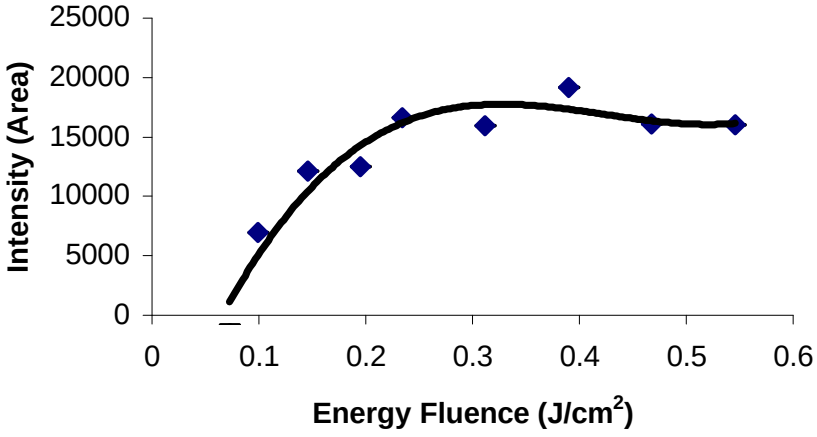

Figure 5.10

Variation of LII signal with laser fluence.

With the 90° configuration, the LII signals at different soot concentrations have been recorded. To vary the soot density in the measurement volume, the solution flow

rate has been varied from 1.06 to 5.69 ml/min (Figure 5.11). Note that the negative peak near 532 nm is due to attenuation by the 532-nm notch filter. A carbon solution of 11.2 g/L was used in this experiment. Variation of the LII signal due to variation of the solution flow rate was recorded with two different spectrometers and is shown in Figure 5.12. Data clearly indicates a linear relation between the LII signal and the solution flow rate. Measurements with a fixed solution flow rate and different solution concentrations have also been performed. The LII signal is linearly proportional to the carbon solution concentration as shown in Figure 5.13. This type of data can serve as calibration data for unknown soot volume density measurements if the soot volume density is calculated from the soot generation parameters or is calibrated with other techniques.

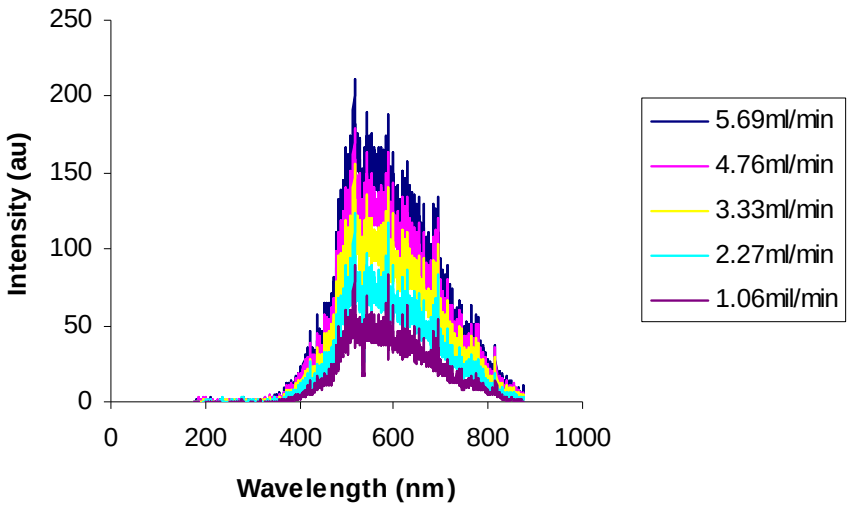

Figure 5.11.

LII spectra at different carbon solution (11.2 g/L) flow rates.

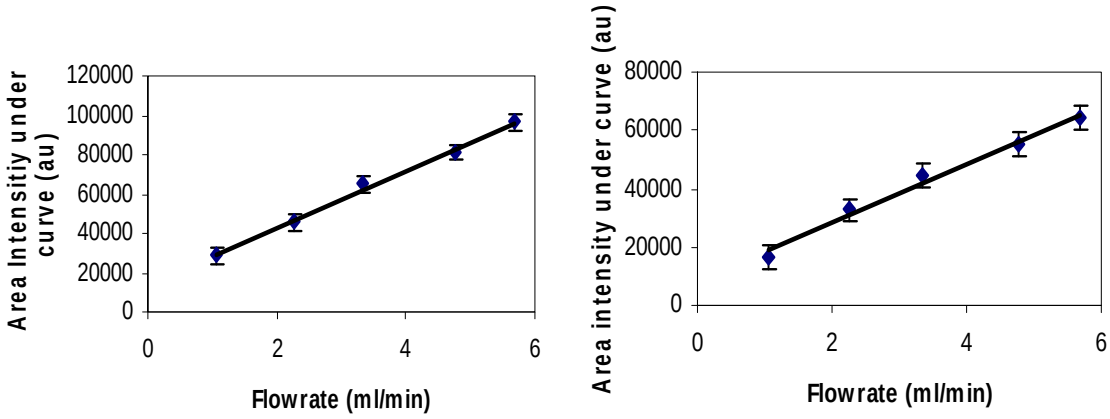

a) b)

Figure 5.12.

Variation of area intensity under curve with flow rate using a) SPEX 500, and b) USB 2000 spectrometers.

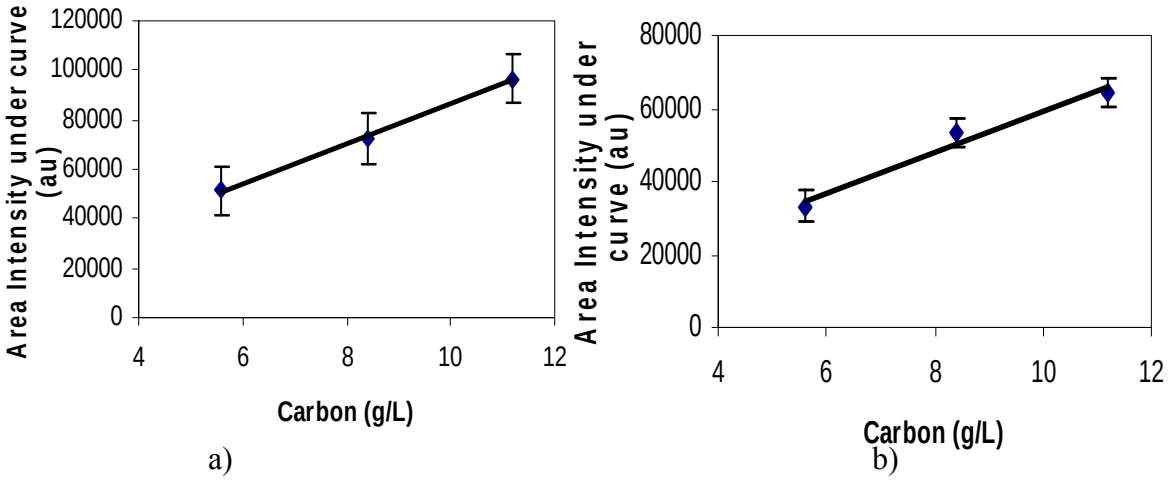

a) b)

Figure 5. 13

Variation of area intensity with different carbon solution concentrations with a) SPEX 500 and b) USB 2000 spectrometers.

The performance of a photomultiplier tube (PMT) for LII detection has been evaluated. An appropriate bandpass filter was placed in front of the PMT to record LII signals at 430 nm and at 650 nm with a PMT. The 532-nm scattered light is eliminated by a holographic notch filter placed before the collection optical fiber. LII signals obtained from different carbon solution concentrations and flow rates were investigated at 430 nm and at 650 nm with PMT detection. Figure 5.14 shows the LII data of a 5.6 g/L carbon solution at different solution flow rates and at different two detection wavelengths. The PMT data all show a linear relationship between the LII signal and the carbon concentration.

5.3.3.1 Flame Measurements

The parametric study performed with the soot generator helped to obtain the optimum experimental setup for LII experiments in a hydrocarbon flame. An acetylene-air diffusion flame was setup for flame measurement (Figure 5.15). The acetylene-air diffusion flame is stabilized at the exit of a 16-mm diameter burner tube. The fuel and air flow rates are held at 392 cm^3/min and 1500 cm^3/min respectively. Flame data were collected with the SPEX 500 spectrometer system. LII signals were collected using 100-ns gate delay and 1000-ns gate width, determined from soot generator measurements. LII signal dependence with different heights above the burner (HAB) values of acetylene-air flames were investigated, and those are shown in Figure 5.16. LII signal intensity and HAB values are linearly dependent on each other (Figure 5.17). Consequently, soot concentration increases with height in the flame. The LII signal as a function of radial position at 2-cm above the burner is shown in Figure 5.18.

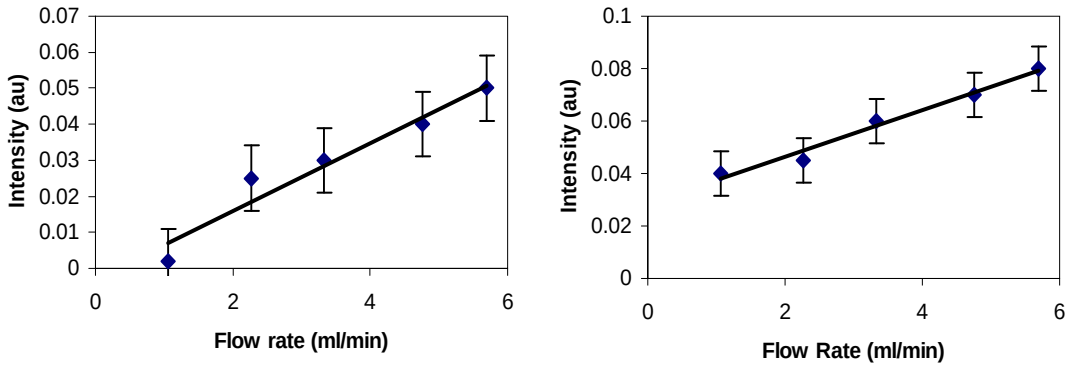

a) b)

Figure 5.14.

LII signals recorded with a PMT for different carbon concentrations a) with 430nm band pass filter. and b) with a 650nm band pass filter.

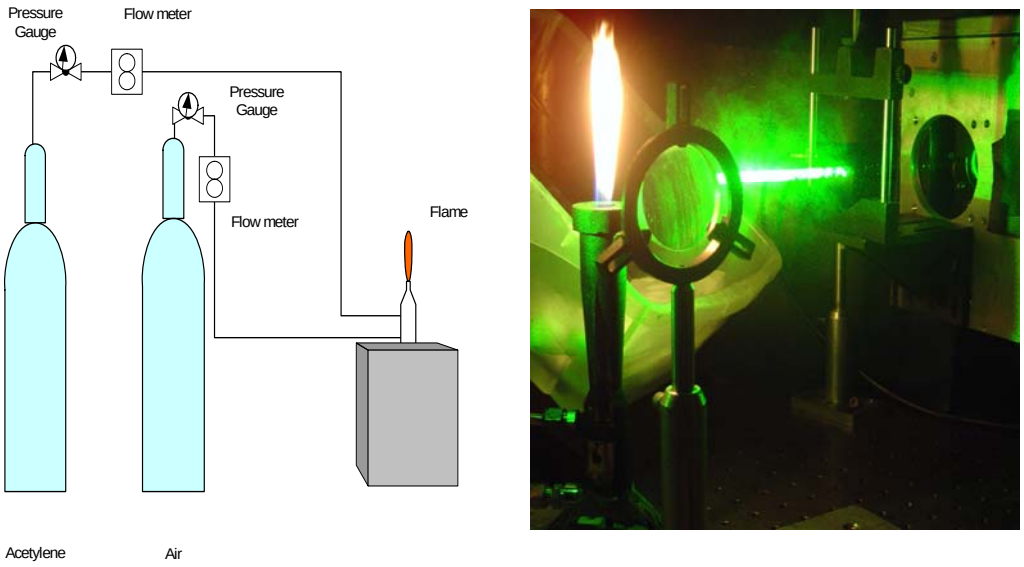

a) **b)**

Figure 5.15

a) Schematic diagram of LII experimental setup with an acetylene/air flame.
b) Flame setup

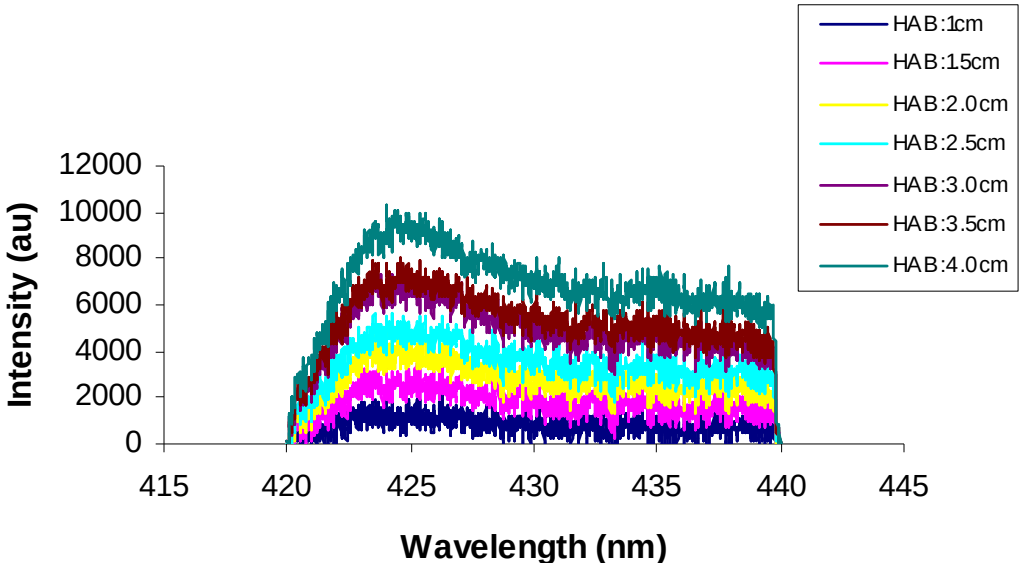

Figure 5.16

LII spectra recorded with a 0.5-m spectrometer at various HAB values.

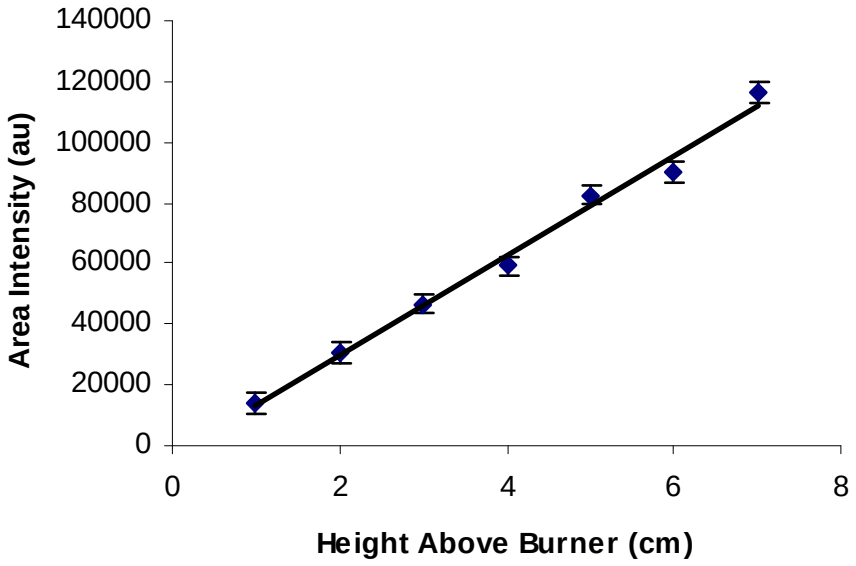

Figure 5.17

Variation of intensity (area) with height above burner (HAB).

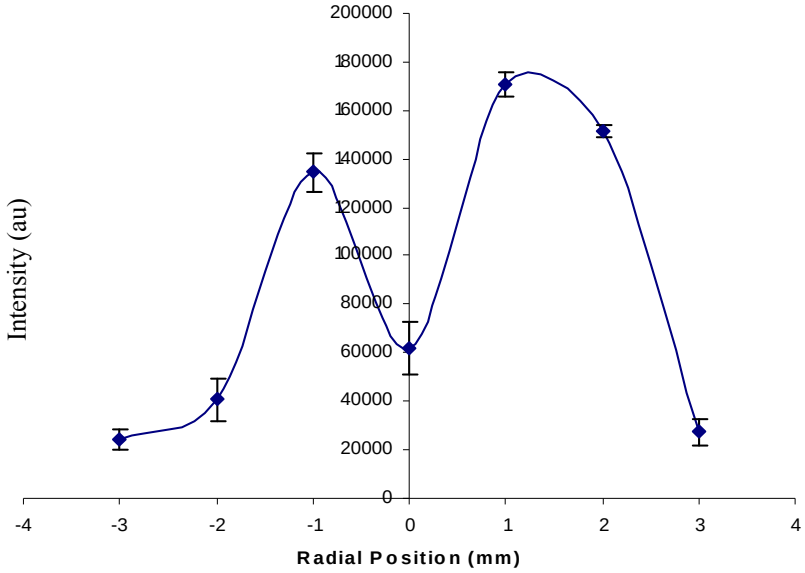

Figure 5.18

Variation of area intensity with radial position in flame at height of 2 cm above burner.

5.3.3.2 Soot Volume Fraction

The particle surface temperature is the key parameter to calculate the soot volume fraction (SVF). The soot temperature from the soot generator was first calculated using Eq. (5.4). The particulate volume fraction (PVF) can then be obtained from Eq. (5.6) with calculated soot temperature.

The soot volume fractions (SVF) of six different HAB values have been calculated from the LII spectra of flames and are presented in Table 5.2. SVF values are higher at the top of the flame. This shows that unburned particles are at higher concentration in that region. SVF values linearly increase with increasing carbon solution concentration in the soot generator experiments (Table 5.3). Average temperature of soot

from the soot generator is 3603 K. SVF values of flames were also calculated from soot generator PVF values.

Table 5.2

Soot volume fractions of flames with different HAB values.

Carbon Solution Concentration (g/ml)	SVF (soot generator)
1.06	2.93×10^{-9}
2.27	3.98×10^{-9}
3.33	6.87×10^{-9}
4.76	8.27×10^{-9}
5.69	1.01×10^{-8}

Table 5.3

Soot volume fraction of soot generator for different carbon solution concentrations.

HAB (cm)	R ($I_{flame}/I_{soot\ generator}$)	SVF (flame)
4.0	1.77	1.78×10^{-8}
3.5	1.40	1.41×10^{-8}
3.0	1.18	1.19×10^{-8}
2.5	0.79	7.97×10^{-9}
2.0	0.65	6.56×10^{-9}
1.5	0.44	4.44×10^{-9}
1.0	0.12	1.21×10^{-9}

5.3.3.3 Soot Particle Structure

Soot is made up of primary particles that clump together to form aggregates. The primary particles are, to a pretty good approximation, spherical. Primary particles range in size from roughly 10 to 100 nm in diameter. It is the aggregation of these primary particles into large clusters that give soot particles their complicated structure. Some soot aggregates are seen to consist of primary particles joined together to form irregular

branched chains. Larger aggregates seem to consist of large clumps of primary particles. It is clear that these structures are not deterministic and must be described statistically. Soot aggregates can contain hundreds or even thousands of primary particles randomly clumped together.

In our soot generator experiments, commercial carbon black from Cabot Corporation in place of soot has been used. The carbon black is dispersed in water. The water is sprayed into a stream of air, and the water droplets evaporate, leaving behind particles of carbon black. An analysis of this experiment shows the following: Assuming a 100-micron diameter droplet of water contains suspended carbon black. The droplet volume can be calculated to be 5.24×10^{-13} m^3. Approximately 5.6 grams of carbon black are mixed with 1 liter of water; hence the concentration of carbon black is 5.6 kg/m^3. Knowing the volume of an average water droplet and the concentration of carbon black in water, the expected mass of carbon black contained in each droplet is calculated to be 2.93×10^{-12} kg.

The specific gravity of amorphous carbon is found to be 1.8 to 2.1 and the specific gravity of graphite is found to be 1.9 to 2.3. We will assume that carbon black has a density of 2 g/cm^3. Cabot Monarch 120 V-6750 carbon black has a primary particle diameter of roughly 220 nm. Therefore, the volume of a primary particle is approximately 9.05×10^{-22} m^3 and the mass of a primary particle is approximately, 1.81×10^{-18} kg.

The average number of primary particles that will be contained in a typical droplet of water is calculated to be 1.62×10^6 by dividing the mass of carbon black contained in each droplet by the mass of a primary particle. Soot agglomerates are

described as fractal. Thus we conclude that the agglomerates produced in this bench top apparatus will, on average, contain over a million primary particles each. Each primary particle is about 220 nm in diameter.

Soot particle measurements from the soot generator with 8.4 g/L carbon solution were carried on with a TEM (JEOL, model JEM-100CX II). The flame setup employing 2.5 L/min air flow rate at 50 psi pressure and 400 cc/min acetylene flow rate at 1 psi pressure was used for soot particle size measurements. Soot samples were collected on coated copper TEM grids to obtain agglomerate soot particle size. TEM grids, mounted at 4-cm height above burner and 1-cm height above soot generator outlet tube, were mounted to a stable holder. TEM micrographs of soot particles from flames and the soot generator can be seen in Figure 5.19. PAH formation and growth of soot depends on the basic steps of fuel pyrolysis. Carbon black reveals that soot particles consist of numerous crystallites on the order of 10^4 primary particles. For comparison, TEM micrographs of Cabot 800 carbon powder were also taken and are shown in Figure 5.20. Carbon atom layer planes form a series of crystallites. Layer plane defects and reactive radical sites are thermally annealed as temperature increases. Graphitic layers are formed which are the most energetic stable form of carbon.[121] Graphitic structure can be seen with measurements with flames, which have higher elevated temperatures (see Fig. 5.19).[127] The analysis of soot particle structure will provide the necessary information for LII modeling.

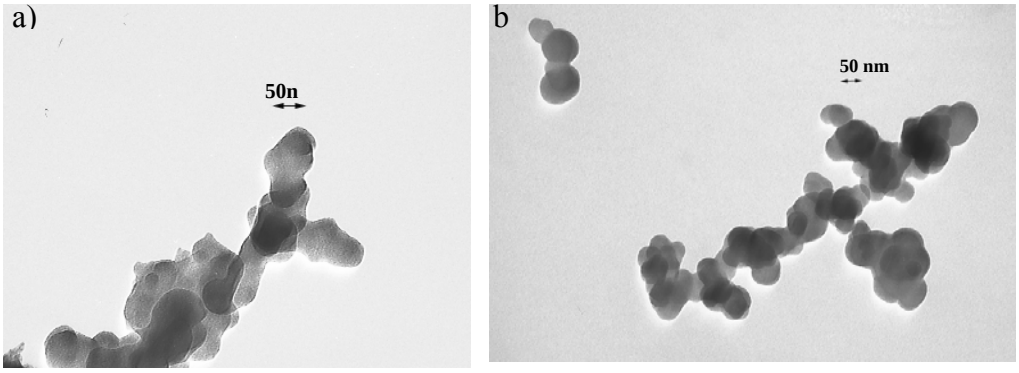

Figure 5.19.

TEM micrographs of soot particles from a) Flame and b) Soot generator.

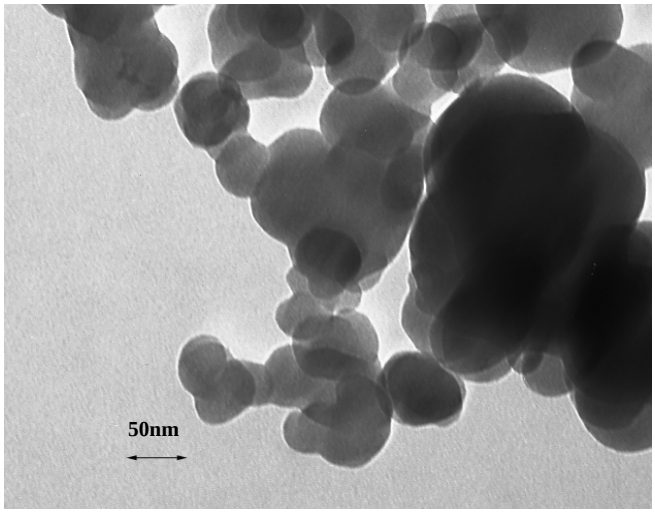

Figure 5.20

TEM micrographs of Cabot 800 carbon powder.

CHAPTER VI

CONCLUSIONS

Laser Induced Breakdown Spectroscopy (LIBS) and Laser Induced Incandescence (LII) based applications were investigated in this dissertation. LII was performed to analyze soot structure and particle volume fractions. LIBS was used to analyze analyte concentrations in liquids, and dried slurry samples. Impurity detection in a gaseous environment was carried out by using LIBS. Conclusions from these investigations are as follows.

6.1 LIBS for Hydrogen Impurity Detection

Application of Laser Induced Breakdown Spectroscopy for detecting impurities was investigated in a hydrogen mixture in Chapter 4.2. For the H2 mixtures N2, O2, and Ar are impurities at different concentrations to calibrate the system. An ungated detection system used in this work has been shown to give reliable and reproductive results. The study of the effect of pressure on the signal to noise (S/N) ratio shows that the S/N ratio increases with increasing pressure until a critical pressure (~24.7 psi in this work) and then decreases with increasing pressure. Peak height and peak ratio calibration for impurity determination both give reliable results. Peak ratio calibration should be more suitable for practical applications. The LODs for impurities was determined to be ~1000

ppm (parts-per-million) for Ar and N2 and ~100 ppm for O2 with the ungated detection system.

6.2 Elemental Analysis of Slurry Samples with LIBS

In Chapter 4.3, elemental analysis of radioactive wastes was carried out by analytical tools at various stages during the vitrification process. Since wet slurry samples create various complications for LIBS, we have developed a LIBS technology based on dried slurry samples. PVC was coated on glass slides to hold the dried samples on the glass substrates. The LIBS signal was enhanced and the standard deviation was reduced as the water content decreased. Calibration curves from multivariate analysis were compared to those from univariate analysis for dried slurry samples. Partial least squares showed significantly better results compared to univariate calibration, with higher regression coefficients and lower RMSEC values. These work demostrated novel techniques for quantitative analysis of dried slurry samples.

6.3 Diagnosis of Biodiesel Flame with LIBS

In Chapter 5.2, a miniature LIBS sensor was developed for characterization of different flames using an ungated miniature spectrometer as the detection system. The intensity ratio of the H to O lines was used to determine the equivalence ratio of CH4/air flames. A linear relationship between the intensity ratio of the H to O lines and the calculated equivalence ratio was obtained for methane/air flames. This research shows that for flames, a LIBS sensor can be developed without an expensive gated detection system. LIBS data of biodiesel flames recorded with an ungated miniature spectrometer

has a high emission background. A data processing method was developed to improve the signal-to-background ratio (S/B) of the LIBS biodiesel flame spectra recorded with the ungated LIBS sensor. Although it is difficult to directly calculate the equivalence ratio for biodiesel flames due to their unknown stochiometric formula, this research has demonstrated the feasibility of using an ungated LIBS sensor as a tool to study the chemical-kinetic mechanisms of biodiesel combustion.

6.4 Soot Volume Fraction Measurements with LII

In Chapter 5.3, the soot structure of hydrocarbons was investigated with the help of a LII system. The performance of two detection systems have been tested and evaluated with a soot generator as well as a flame system. A low-resolution Ocean Optics spectrometer with a CCD detector was also used to cover a wider spectral region in the soot generator measurements. It was used to examine the spectral interferences and evaluate various filters for PMT detection. The study shows that we can use PMTs with two proper bandpass filters to monitor the signal ratio of selected spectral regions to extract soot volume fraction (SVF). Flame measurements show that LII can be employed for on-line, real-time measurements to characterize the performance of hydrocarbon rocket engines and also evaluate the effects of the engine testing on the environment.

REFERENCES

1. W. Demtroder, “Laser Spectroscopy Basic Concepts and Instrumentation”, Springer, 1996.

2. L.Radziemski, Solarz R.W., Paisner J. A., “Laser Spectroscopy and Its Applications”, Marcel Dekker Inc., 1987.

3. D. A. Cremers, L. J. Radziemski, and T. R. Loree, "Spectrochemical Analysis of Liquids Using the Laser Spark," Applied Spectroscopy. 38, 721, 1984.

4. A. J. Miziolek, V. Palleschi, I. Schechter, “Laser- Induced Breakdown Spectroscopy”, Cambridge, 2006.

5. C. J. Casch, “New Soot Diagnostics in Flames Based on Laser Vaporization of Small Soot Particles in a Flame”, Applied Optics, 23, 2209, 1984.

6. R.L. Vander Wal, T.M. Ticich, A. B. Sephens, “Optical and Microscopy Investigations of Soot Structure Alterations by Laser Induced Incandescence”, Applied Physics B, 67, 115, 1998.

7. D. R. Snelling, G. J. Smallwood, R. A. Sawchuk., W. S. Neil, D. Gareau, W. L. Chippior, F. Liu, O. L Gulder, and W. D. Bachalo, “Particulate Matter Measurements in a Diesel Engine Exhaust by Laser-Induced Incandescence and the Standart Gravimetric Procedure”, SAE Paper, Society of Automotive Engineers, Warrendale, PA, 1999.

8. S. L. Shapiro, A. J. Campillo, V. H. Kollman, W. B. Goad “ Exciton transfer in DNA”, Optics Communications, 15, 308, 1975.

9. J. L. Abraham, M. E. Andersen, R. Z. Muggli, “Raman Microprobe Identification Of Pathologically And Forensically Important Particles In Tissue”, Proceedings of Eigth International Conference of Raman Spectroscopy, Bordeaux, 809, 1980.

10. M. Couzi., F. Cruege, P. Martineau, C. Mullet, R. Pailler, “Characterization of composite materials by means of the Raman microprobe”, Microbeam Analysis, 18, 274, 1983

11. H. Zhang, F. Y. Yueh and J. P. Singh, “Performance Evaluation of Laser Induced Breakdown Spectroscopy as a Multi-metal Continuous Emission Monitor”, J. Air & Waste Management Assoc. 51,174, 2001.

12. B. J. Marquardt, D. N. Stratis, D. A. Cremers, S. M. Angel, “Novel Probe for Laser-Induced Breakdown Spectroscopy and Raman Measurements Using an Imaging Optical Fiber”, 52, 1148, 1998

13. J. P. Singh and S. N. Thakur, Laser-Induced Breakdown Spectroscopy, Elsevier Science B. V., 2007.

14. S. Schraml, C. Heimgartner, S. Will, A. Leipertz, A. Hemm, “Application of a New Soot Sensor for Exhaust Emission Control Based on Time Resolved Laser-Induced Incandescence (TIRE-LII) SAE Technical Paper Series, Society Of Automotive Engineers, Warrendale, PA, 2000

15. J.M. Hollas, “Modern Spectroscopy”, Wiley & Sons, New York, 2004

16. W. R. Hindmarsh, “Collision broadening of spectral lines by neutral atoms”, Progress in Quantum Electronics”, 2, 143, 1973

17. D. D. Burgess, “Spectroscopy of Laboratory Plasmas”, Space Science Reviews, 13, 493, 1972.

18. W. L. Kruer, “ The Physics of Laser Plasma Interaction”, Wesley, New York, 1988

19. G. Bekefi, “Principle of Laser Plasmas”, Wiley and Sons, New York, 1976

20. O. Samek, D. C. S. Beddows, J. Kaiser, S. V. Kukhlevsky, M. Lisˇka, H. H. Telle, J. Young, “Application of Laser-Induced Breakdown Spectroscopy to In Situ Analysis Of Liquid Samples”, Optical Engineering, 39, 8, 2248, 2000

21. H. R. Griem, “Plasma Spectroscopy”, Mc Graw Hill, New York, 1964

22. D. L. Hofeldt, “Real-Time Soot Concentration Measurement Techniques for Engine Exhaust Streams”, Journal of fuels Lubricant, 4, 45, 1993

23. F. Cignoli, S. Benecchi, G. Zizak, “Time-Delayed Detection of Laser-Induced Incandescence for the Two Dimensional Visualization of Soot in Flames”, Applied Optics, 33, 5778, 1994

24. M. J. Colles., C. R. Pidgeon., “Tunable Lasers” Reports on Progress in Physics, 38, 329, 1975

25. K.L Hohla , “Excimer Pumped Dye Lasers-The New Generation”, Laser Focus, 18, 67, 1982.

26. C. Yamanaka., “Short Wavelength Lasers”, Springer Proceeding Physics, 30, 1988.

27. H. E. Bauer, F. Leis, K. Niemax., “Laser Induced Breakdown Spectrometry With An Échelle Spectrometer and Intensified Charge Coupled Device Detection”, Spectrochimica Acta B, 53, 1815, 1998.

28. C. Haisch, U. Panne., R. Niessner., “Combination of An Intensified Charge Coupled Device With An Echelle Spectrograph For Analysis of Colloidal Material By Laser–Induced Plasma Spectroscopy”, Spectrochimica Acta B, 53, 1657, 1998.

29. D. F.Barbe, W. D. Baker , K. L. Davis “Signal Processing With Chargecoupled Devices”, Topics in Applied Physics, 41, 91, 1979.

30. R. B. Bilhorn, J. V. Sweedler, P. M. Epperson, “Charge Transfer Device Detectors for Analytical Optical Spectroscopy, Operation and Characteristics”, Applied Spectroscopy, 41, 1114, 1987.

31. J. P. Singh, F. Y. Yueh, H. Zhang, and K. P. Karney, “A Preliminary Study Of The Determination Of Uranium, Plutonium And Neptunium By Laser Induced Breakdown Spectroscopy”, RecentRes. Dev. Appl. Spectrosc. 2, 59, 1999.

32. V. N. Rai, A. K. Rai, F. Y. Yueh, and J. P. Singh, “Optical Emission From Laser Induced Breakdown Plasma Of Solid And Liquid Samples In The Presence Of Magnetic Field”, Applied Optics 42, 2085, 2003.

33. O. Samek, D. C. S. Beddows, J. Kaiser, S. V. Kukhlevsky, M. Liska, H. H. Telle, and J. Young, “Application Of Laser Induced Breakdown Spectroscopy To In Situ Analysis Of Liquid Samples,” Optics Engineering, 39, 2248, 2000.

34. T. A. Reichardt, W. Einfeld, and T. J. Kulp, Review of Remote Detection for Natural Gas Transmission Pipeline Leak, Report for U.S. Department of Energy’s National Energy Technology Laboratory (NETL), Sandia National Laboratory, Albuquerque, NM.

35. W. A. de Groot, “Fiber-optic Based Compact Gas Leak Detection System”,” AIAA-1995-2646 ASME, SAE, and ASEE, Joint Propulsion Conference and Exhibit, 31st, San Diego, CA, July 10, 1995.

36. H. W. Schrotter and H. W. Klockner, Raman Spectroscopy of Gases and Liquids, Ed. by A. Weber, pp. 123-166, Springer- Verlag, Berlin, 1979.

37. W. R. Fenner, H. A. Hyatt, J. M. Kellam, and S. P. S. Porto, “Raman Cross Section of Some Simple Gases” Journal of Optical Society of America, 63, 73, 1973.

38. J. J. Valentini , Spectrometric Techniques, Volume 4, Academic Press, New York, 1985.

39. J. D. Burakov, P.Y. Misyakov, P. A. Naumenko, S. V. Nechaev, G. T. Rozdobarin, V. V. Semenov, L. V. Sokolova, and I. P. Folomkin, "Use of the Method of Resonance Fluorescence with a Dye Laser for Plasma Diagnostics in the FT-1 Tokamak Installation," JETP Lett. 26, 403, 1977.

40. B. Schweer, D. Rusbuldt, E. Hintz, J.B. Roberto, and W.R. Husinsky, "Measurement of the Density and Velocity Distribution of Neutral Fe in ISX-B by Laser Fluorescence Spectroscopy", Journal of Nuclear Materials, 93-94, Part 1, 357, 1980.

41. P. Gohil, G. Kolbe, M.J. Forrest, D.D. Burgess, and B.Z. Hu, "A Measurement of the Neutral Hydrogen Density Determined from Balmer Alpha Fluorescence Scattering in the HBTX1A Reverse Field Pinch," Journal of Physics D, 16,333, 1983.

42. D. R. Crosley and G. P. Smith, "Laser Induced Fluorescence Spectroscopy for Combustion Diagnostics," Optical Engineering, 2,545-553, 1983.

43. A. C. Eckbreth, Laser Diagnostics for Combustion Temperature and Species, 2nd Edition, Gordon & Beach Publishers, Amsterdam, pp. 381, 1996.

44. K. Kohse, and J. B. Jeffries, Applied Combustion Diagnostics, Taylor Francis, New York, 2002.

45. G. Berden, R. Peeters, and G. Meijer, "Cavity Ring-down Spectroscopy: Experimental Schemes and Applications", Int. Rev. Phys. Chem., 19, 565, 2000.

46. P. E. Best, P.L. Chien, R. M. Carangelo, P. R. Solomon, M. Danchak and I. Ilovivi, "Tomographic Reconstruction of FT-IR Emission and Transmission Spectra in a Sooting Laminar Diffusion Flame: Species Concentrations and Temperatures", Combustion and Flame, 85, 309, 1991.

47. H. Zhang, F. Y. Yueh, and J. P. Singh, "Laser-induced Breakdown Spectroscopy as a Multi-metal Continuous Emission Monitor," Applied Optics, 38, 1459, 1999.

48. J. Ball, V. Hoheiter and D. W. Hahn, "Hydrogen Leak Detection Using Laser Induced Breakdown Spectroscopy", Applied Spectroscopy, 59, 348, 2005.

49. J. P. Singh, F. Y. Yueh, H. Zhang and R. L. Cook, "Study of Laser Induced Breakdown Spectroscopy as a Process Monitor and Control Tool for Hazardous Waste Remediation", Process Control and Quality, 10,247, 1997.

50. F. Y. Yueh, J. P. Singh, and H. Zhang, "Elemental Analysis with Laser-Induced Breakdown Spectroscopy", Encyclopedia of Analytical Chemistry: Instrumentation and Application, Ed. R. A. Myer, Wiley, Chichester, UK, 2066, 2000

51. H. Zhang, F. Y. Yueh and J. P. Singh, "Performance Evaluation of Laser Induced Breakdown Spectrometry as a Multi-Metal Continuous Emission Monitor," J. Air & Waste Management Association, 51, 174, 2001.

52. V. N. Rai, J. P. Singh, C. B. Winstead, F. Y., Yueh, and R. L. Cook, , "Laser-Induced Breakdown and Emission Spectroscopy of Hydrocarbon Fueled Flame and Rocket Engine Simulator Plume," AIAA Journal, 41, 2192, 2002.

53. F. Y., Yueh, R. C., Sharma, J. P. Singh, and H., Zhang, "Evaluation of the Potential of Laser- Induced Breakdown Spectroscopy for Detection of Trace Element in Liquid", J. Air & Waste Management Assoc., 52, 1307, 2002.

54. G. Arca, A. Ciucci, V. Palleschi, S. Rastelli, and E. Tognoni, "Trace Element Analysis In Water By The Laser-Induced Breakdown Spectroscopy Technique", Journal of Applied Spectroscopy, 51, 8, 1102, 1997.

55. A. K. Rai, H. Zhang, F. Y. Yueh, J. P. Singh and A. Weisberg, , Parametric Study of a Fiber Optic Laser Induce Breakdown Spectroscopy Probe for Analysis of Aluminum Alloy. Spectrochim Acta Part B 56, 2371, 2001.

56. A. K. Rai, F. Y., Yueh, and J. P. Singh, "Laser- Induced Breakdown Spectroscopy of Molten Aluminum Alloy", Applied Optics, 42, 2078, 2003.

57. R. E. Neuhauser, U. PanneaV, R. Niessnera, G. A. Petruccib, P. Cavallib, and N. Omenetto, "On-line and in-situ Detection of Lead Aerosols by Plasma-Spectroscopy and Laser-excited Atomic Fluorescence Spectroscopy", Analytica Chimica Acta, 346, 3748, 1997.

58 K. Y. Yamamoto, D. A. Cremers, M. J. Ferris, and L. E. Foster, "Detection of Metals in the Environment Using a Portable Laser-Induced Breakdown Spectroscopy Instrument," Applied Spectroscopy, 50, 222, 1996.

59 D. A. Cremers, J.E. Baefield II, and A.C. Koskelo, "Remote Elemental Analysis by Laser- Induced Breakdown Spectroscopy Using a Fiber Optic Cable", Applied Spectroscopy, 49, 6, 857, 1995

60. A.V. Pakhomov, W. Nichols, and J. Borysow, "Laser-Induced Breakdown Spectroscopy for Detection of Lead in Concrete", Applied Spectroscopy, 50, 880, 1996.

61. J. R. Wachter and D. A. Cremers, "Determination of Uranium in Solution Using Laser- Induced Breakdown Spectroscopy", Applied Spectroscopy, 41, 1042, 1987.

62. H. Zhang, F. Y. Yueh, and J. P. Singh, "Laser-induced Breakdown Spectroscopy as a multi-metal Continuous Emission Monitor", Applied Optics, 38, 1459, 1999.

63. J. Ball, V. Hoheiter and D. W. Hahn, "Hydrogen Leak Detection Using Laser Induced Breakdown Spectroscopy", Applied. Spectroscopy, 59, 348, 2005.

64. V. N. Rai, J. P. Singh, C. Winstead, F. Y. Yueh, and R. L. Cook, "Laser-Induced Breakdown Spectroscopy of Hydrocarbon Flame and Rocket Engine Simulator Plume", AIAA Journal,41, 11, 2003.

65. R. W. Schmeider, "Combustion Applications of Laser-Induced Breakdown Spectroscopy", Proceedings of the Electro- Optics Laser Conference, 17, 1981.

66. T. X. Phuoc and F. P. White, "Laser Induced Spark for measurements of the fuel-to-air ratio of a combustible mixture", Fuel, 81, 1761, 2002

67. P. Stavropoulos, A. Michalakou, G. Skevi, and S. Couris "Laser-induced Breakdown Spectroscopy as an Analytical Tool for Equivalence Ratio Measurement in Methane–Air Premixed Flames", Spectrochimica Acta B, 60, 1092, 2005.

68. NIST Atomic Spectra Database: http://physics.nist.gov/PhysRefData/ASD/.

69. H. R Griem, Plasma Spectroscopy, McGraw-Hill, New York, 1964.

70. M. Adamson, A. Padmanabhan, G,J Godfrey, and S.J. Rehse, "Laser-induced Breakdown Spectroscopy at a Water/Gas Interface: A Study of Bath Gas-Dependent Molecular Species, Spectrochimica Acta B, 62, 1348, 2007.

71. N. Tsuda and J. Yamada, "Physical Properties of Dense Plasma Produced By XeCl Excimer Laser In High-Pressure Argon Gases," Japanese Journal of Applied. Physics, 38, 3712, 1999.

72. J. D. Ingle, S. R. Crouch, and K. M. Lafferty, Spectrochemical Analysis, Prentice Hall, Englewood Clifds, New Jersey, USA, 1988.

73. S. Y. Oh, T. Miller, F. Y. Yueh, J. P. Singh, "Comparative Study Of Laser Induced Breakdown Spectroscopy Measurement Using Two Slurry Circulation Systems", Applied Optics, 46, 4020, 2007.

74. S. L. Lui, Godwal, Y. Taschuk, Y. Y. Tsui, R. Fedosejevs," Detection Of Lead In Water Using Laser-Induced Breakdown Spectroscopy And Laser-Induced Fluorescence", Analytical Chemistry , 80, 6, 1995, 2008.

75. Z. J. Chen, H. K. Li, M. Liu, R. H. Li, " Fast And Sensitive Trace Metal Analysis In Aqueous Solutions By Laser-Induced Breakdown Spectroscopy Using Wood Slice Substrates", Spectrochimica Acta Part B, 63, 1, 64, 2008.

76. N. K. Rai, A. K. Rai, "LIBS - An Efficient Approach For The Determination Of Cr In Industrial Wastewater", Journal Of Hazardous Materials, 150, 3, 835, 2008.

77. V. Lazic, S. Jovicevic, R. Fantoni, F. Colao, "Efficient plasma and bubble generation under water by an optimized laser excitation and its application for liquid analyses by laser-induced breakdown spectroscopy", Spectrochimica Acta Part B-Atomic Spectroscopy, 62, 12, 1433, 2007.

78. H. Zheng, F. Y. Yueh, T. Miller, J. P. Singh, K. E. Zeigler, J. C. Marra, Analysis of plutonium oxide surrogate residue using laser-induced breakdown spectroscopy, Spectrochimica Acta Part B, 63, 968, 2008.

79. S. Y. Oh, F. Y. Yueh, J. P. Singh, C. C. Herman, Kristine Zeigler, "Preliminary Evaluation Of Laser Induced Breakdown Spectroscopy For Slurry Samples", Spectrochimica Acta Part B, 64, 113, 2009

80. H. Balzer, M. Hoehne, V. Sturm, R. Noll , "Online Coating Thickness Measurement And Depth Profiling Of Zinc Coated Sheet Steel By Laser-Induced Breakdown Spectroscopy", Spectrochimica Acta Part B, 60, 1172, 2005.

81. T. Kim, B. T. Nguyen, V. Minassian, C. T. Lin, "Paints and coatings monitored by laser-induced breakdown spectroscopy", Journal of Coating Technology Research, 4, 241, 2007.

82. Z. M. Martin, N. Labbe, T. G. Rials, S. D. Wullschleger, "Analysis of preservative-treated wood by multivariate analysis of laser-induced breakdown spectroscopy spectra", Spectrochimica Acta Part B, 60, 1179, 2005.

83. P. Felizardo, P. Baptista, J. C. Menezes, M. J. N. Correia, "Multivariate near infrared spectroscopy models for predicting methanol and water content in biodiesel", Analytica Chimica Acta, 595, 107, 2007.

84. M. R. Poirier, Recipe for Simulated Tank 8F Sludge Containing No RCRA Metals or Halides, WSRC-TR-2005-00045 Rev.0, Westinghouse Savannah River Company, Aiken SC.

85. K. H. Esbensen, Multivariate Data Analysis in Practice, 5th edition, Camo Inc., 2004.

86. H. Fink, U. Panne, R. Niessener, "Process Analysis of Recycled Thermoplasts from Consumer Electronics by Laser-Induced Plasma Spectroscopy", Analytical Chemistry, 74, 4324, 2002.

87. H. Zhang, F. Y. Yueh and J. P. Singh, “Laser-Induced Breakdown Spectroscopy as a Multi-metal Continuous- Emission Monitor”, Applied Optics, 38, 1459, 1999.

88. D. W. Hahn, W. L. Flower, and K. R. Henken, “Discrete Particle Detection and Metal Emission Monitoring using Laser Induced Breakdown Spectroscopy”, Applied. Spectroscopy, 51, 1836, 1997.

89. H. Zhang, J. P. Singh, F. Y. Yueh and R. L. Cook, “Laser- Induced Breakdown Spectra in a Coal-Fired MHD Facility”, Applied Spectroscopy. 49, 1617, 1995.

90. A. Michalakou, P. Stavropoulos, and S. Couris, “Laser-Induced Breakdown Spectroscopy in Reactive Flows of Hydrocarbon-air Mixtures”, Applied Physics Letters, 92, 1501, 2008.

91. D. A. Cremers and L. J. Radziemski, “Detection of chlorine and fluorine in air by laser-induced breakdown spectrometry,” Analytical Chemistry, 55, 1252, 1983.

92. L. J. Radziemski, T. R. Loree, D. A. Cremers, and N. M. Hoffman, “Time-Resolved Laser- Induced Breakdown Spectrometry of Aerosols,” Analytical Chemistry, 55, 1246, 1983.

93. J. P. Singh, H. Zhang, F. Y. Yueh, and K. P. Carney, “Investigation of the Effects of Atmospheric Conditions on the Quantification of Metal Hydrides Using Laser Induced Breakdown Spectroscopy,” Applied Spectroscopy, 50, 764, 1996.

94. P.A. Berg, G.P. Smith, J.B. Jeffries, and D.R. Crosley, “Nitric Oxide Formation and Reburn in Low-Pressure Methane Flames,” Proceedings Combustion Instruments 27, 1377, 1998.

95. J. Luque, J. B. Jeffries, G. P. Smith, D.R. Crosley, and J. J. Scherer, “Combined Cavity Ringdown Absorbtion and Laser-Induced Florescence Imaging Measurements of CN(BX) and CH(B-X) in Low Pressure CH4-O2-N2 and CH4-NO-O2-N2 Flames,” Combustion and Flame, 126, 1725, 2001.

96. J. W. Thoman, and A. McIlroy, “Absolute CH Radical Concentrations in Rich Low-Pressure Methane-Oxygen-Argon Flames via Cavity Ringdown Spectroscopy of the A2Δ- X2Π Transition”, Journal of Physical Chemistry A, 104, 4953, 2000.

97. K. T. Walsh, M. B. Long, M. A. Tanoff, and M. D. Smooke, “Experimental and Computational Study of CH, CH, and OH in an Axisymmetric Laminar Diffusion Flame”, Proceedings Combustion Institute, 27, 615, 1998.

98. J. Luque, J. B. Jeffries, G. P. Smith, D. R. Crosley, K. T. Walsh, M. B. Long, and M. D. Smooke, “ CH(A-X) and OH(A-X) Optical Emission in an Axisymmetric Laminar Diffusion Flame”, Combustion and Flame, 122, 172, 2000.

99. A. C. Eckbreth and R. J. Hall, "CARS Concentration Sensitivity With and Without Nonresonant Background Suppression", Combustion Science and Technology, 25, 175, 1981.

100. R. L. Vander Wal, K. A. Jensen, and M. Y. Choi, "Simultaneous Laser-Induced Emission of Soot and Polycyclic Aeromatic Hydrocarbons within a Gas-Jet Diffusion Flame," Combustion and Flame, 109, 399, 1997.

101. R. L. Vander Wal, Z. Zhou, and M. Y. Choi, "Laser- Induced Incandescence Calibration via Gravimetric Sampling", Combustion and Flame 105, 462, 1996.

102. R. L. Vander Wal, "Onset of Carbonization: Special Location via Simultaneous LIFLII and Characterization via TEM", Combustion Science and Technology, 118, 343, 1996.

103. C. R. Shaddix and K. C. Smyth, "Laser- Induced Incandescence Measurement of Soot Production in Steady and Flickering Methane, Propane, and Ethylene Diffusion Flame", Combustion and Flame, 107, 418, 1996.

104. S. Einecke, C. Schulz, and V. Sick, "Measurement of Temperature, Fuel Concentration and Equivalence Ratio Fields using Tracer LIF in IC Engine Combustion", Applied Physics B, 71, 717, 2000.

105. L. Ma, S. T. Sanders, J. B. Jeffries, and R. K. Hanson, "Monitoring and Control of a Pulse Detonation Engine using a Diode-Laser Fuel Concentration and Temperature Sensor," Proceedings of Combustion Institute, 29, 161, 2003.

106. F. Ferioli, P. V. Puzinauskas, and S. G. Buckley, "Laser-Induced Breakdown Spectroscopy for On-Line Engine Equivalence Ratio Measurements", Applied Spectroscopy, 57, 1183, 2003.

107. F. Ferioli and S. G. Buckley, "Measurements of Hydrocarbons Using Laser-induced Breakdown Spectroscopy", Combustion and Flame, 144, 435, 2006.

108. T. X. Phuoc and F. P. White, "Laser Induced Spark for Measurements of the Fuel-to- Air Ratio of a Combustible Mixture", Fuel, 81, 1761, 2002.

109. P. Stavropoulos, A. Michalakou, G. Skevis, and S. Couris, "Quantitative Local Equivalence Ratio Determination in Laminar Premixed Methane–Air Flames by Laser Induced breakdown Spectroscopy (LIBS)", Chemical Physics Letters, 404, 309, 2005.

110. L. Zimmer and S. Tachibana, "Laser Induced Plasma Spectroscopy for Local Equivalence Ratio Measurements in an Oscillating Combustion Environment", Proceedings of the Combustion Institute, 31, 737, 2007.

111. X. Lu, J. Ma, L. Ji, and Z. Huang, "Experimental Study on the Combustion Characteristics and Emissions of Biodiesel Fueled Compression Ignition Engines with Premixed Dimethoxymethane", Energy & Fuels, 21, 3144, 2007.

112. M. P. P. Castro, A. A. Andrade, R. W. A. Franco, P. C. M. L. Miranda, M. Sthel, H. Vargas, R. Constantino, and M. L. Baesso, "Thermal Properties Measurements in Biodiesel Oils using Photothermal Techniques", Chemical Physics Letters, 411, 18, 2005.

113. C. Y. Lin and H. A. Lin, "Diesel Engine Performance and Emission Characteristics of Biodiesel Produced by the Peroxidation Process", Fuel, 85, 298, 2006.

114. P. Saxena and F. A. Williams, "Numerical and Experimental Studies of Ethanol Flame", Proceedings of the Combustion Institute, 31, 1149, 2007.

115. T. W. Lee and N. Hegde, "Laser-induced Breakdown Spectroscopy for *in situ* Diagnostics of Combustion Parameters Including Temperature", Combustion and Flame, 142, 314, 2005.

116. N. M. Ribeiro, A. C. Pinto, C. M. Quintella, G. O. da Rocha, O. S. G. Teixeira, L. L. N. Guarieiro, M. C. Rangel, M. C. C. Veloso, M. J. C. Rezende, R. S. Cruz, A. M. de Oliveira, E. A. Torres, and J. B. de Andrade, "The Role of Additives for Diesel and Diesel Blended (Ethanol or Biodiesel) Fuels: A Review", Energy & Fuels, 21, 2433, 2007.

117. R. T. Wainner and J. M. Seitzman, "Soot Diagnostics using Laser-Induced Incandescence in Flames and Exhaust Flows," Proceedings of 37th AIAA Aerospace Sciences Meeting and Exhibit, AIAA, 99, 1999.

118. L. A. Melton, "Soot Diagnostics Based on Laser Heating," Applied Optics, 23, 2201, 1984.

119 D. R. Snelling, G. J. Smallwood, I. G. Campbell, J. E. Medlock, and O. L. Gulder, "Development and Application of Laser-Induced Incandescence (LII) as a Diagnostic for Soot Particulate Measurements", AGARD 90th Symposium of the Propulsion and Energetics Panel on Advanced Non-Intrusive Instrumentation for Propulsion Engines, October, Brussels, Belgium, 1997.

120. R. L. Vander Wal, "Laser-Induced Incandescence: Detection Issues", Applied Optics, 35, 6548, 1996.

121. R. L. Vander Wal1, T. M. Ticich, A. B. Stephens, "Optical and microscopy investigations of soot structure alterations by laser-induced incandescence", Applied Physics B Lasers and Optics, 67, 115, 1998.

122. Randy L. Vander Wal and Thomas M. Ticich, “Cavity ringdown and laser-induced incandescence measurements of soot”, Applied Optics, 38, 1144, 1999.

123. D. R. Snelling, K. A. Thomson, G. J. Smallwood, and Ö. L. Gülder, “Two-Dimensional Imaging of Soot Volume Fraction in Laminar Diffusion Flames,” Applied Optics, 38, 2478, 1999.

124. D. R. Snelling, F. Liu, G. J. Smallwood, and Ö. L. Gülder, “Evaluation of the Nanoscale Heat and Mass Transfer Model of LII: Prediction of the Excitation Intensity,” Proceedings of NHTC’00 34 National Heat Transfer Conference, Pittsburgh, Pennsylvania, August 20-22, 2000.

125. R. A. Dobbins and C. M. Megaridis, “Morphology of Flame-Generated Soot As Determined by Thermophoretic Sampling”, Langmuir, 3, 254, 1987.

126. G. D. Yoder, P. K. Diwakar, and D. W. Hahn, “Assessment of Soot Particle Vaporization Effects during Laser-Induced Incandescence with Time-Resolved Light Scattering”, Applied Optics, 44, 4211, 2005.

127. R. L. Vander Wal and K. A. Jensen, “Laser-induced Incandescence: Excitation Intensity,” Applied Optics, 37, 1607, 1998.